Adaptive Control of Hypersonic Vehicles

by

Travis Eli Gibson

Submitted to the Department of Mechanical Engineering
in partial fulfillment of the requirements for the degree of

Master of Science

at the

MASSACHUSETTS INSTITUTE OF TECHNOLOGY

September 2008

Author .....
Department of Mechanical Engineering
August 15, 2008

Certified by .....
Anuradha M. Annaswamy
Senior Research Scientist
Thesis Supervisor

Accepted by .....
Lallit Anand
Chairman, Department Committee on Graduate Students

Adaptive Control of Hypersonic Vehicles

by

Travis Eli Gibson

Submitted to the Department of Mechanical Engineering
on August 15, 2008, in partial fulfillment of the
requirements for the degree of
Master of Science

Abstract

The guidance, navigation and control of hypersonic vehicles are highly challenging tasks due to the fact that the dynamics of the airframe, propulsion system and structure are integrated and highly interactive. Such a coupling makes it difficult to model various components with a requisite degree of accuracy. This in turn makes various control tasks including altitude and velocity command tracking in the cruise phase of the flight extremely difficult. This work proposes an adaptive controller for a hypersonic cruise vehicle subject to: aerodynamic uncertainties, center-of-gravity movements, actuator saturation, failures, and time-delays. The adaptive control architecture is based on a linearized model of the underlying rigid body dynamics and explicitly accommodates for all uncertainties. Within the control structure is a baseline Proportional Integral Filter commonly used in optimal control designs. The control design is validated using a highfidelity HSV model that incorporates various effects including coupling between structural modes and aerodynamics, and thrust pitch coupling. Analysis of the Adaptive Robust Controller for Hypersonic Vehicles (ARCH) is carried out using a control verification methodology. This methodology illustrates the resilience of the controller to the uncertainties mentioned above for a set of closed-loop requirements that prevent excessive structural loading, poor tracking performance, and engine stalls. This analysis enables the quantification of the improvements that result from using and adaptive controller for a typical maneuver in the V–h space under cruise conditions.

Thesis Supervisor: Anuradha M. Annaswamy
Title: Senior Research Scientist

Acknowledgments

I would like to thank Dr. Anuradha Annaswamy for her continued support in my research endeavors. I believe we will continue to generate great work together. Thank you as well to Dr. Luis Crespo of the NIA for his research support. His work has helped to illustrate the benefits of my research. I would also like to thank Dr. Sean Kenny at NASA Langley for his direction during my summer work. I would like to thank my lab mates: Yildiray Yildiz, Dr. Jinho Jang, Zac Dydek, Megumi Matsutani and Manohar Srikanth. And of course my mom dad and brother for relaxing times back in Florida. Finally I would like to thank God for helping me through my long nights in lab, and these intense semesters at MIT.

Contents

List of Figures

List of Tables

Chapter 1

Introduction

> "Not since the Right Brothers solved the basic problems of sustained, controlled flight has there been such an assault upon our atmosphere as during the first years of the space age. Man extended and speeded up his travels within the vast ocean of air surrounding the Earth until he achieved flight outside its confines. This remarkable accomplishment was the culmination of a long history of effort to harness the force of that air so that he could explore the three-dimensional ocean of atmosphere in which he lives. That history had shown him that before he could explore his ethereal ocean, he must first explore the more restrictive world of aerodynamic forces."[46]
>
> *Wendell H. Stillwell*

In attempts to slice through the air at higher and higher speeds, ever more elegant and abstract aircraft designs have been conjured by NASA engineers and scientist. The X–43 is one such aircraft, Figure 1-3. This aircraft is a flying butter knife. One can imagine controlling it is not an easy task. Rear control surfaces, strong engine–airframe coupling and flexibility effects each compound the control problem, and the problem is exacerbated at hypersonic speeds. In this work an adaptive control algorithm is presented that has superior performance and robustness characteristics

when compared to a nominal classic controller.

1.1 History of X–Planes

The *National Advisory Committee for Aeronautics* (NACA) started the United States X–Plane Program in 1945 with the XS–1, later designated X–1, Figure 1-1. A contract was given to Bell Aircraft Inc., and oversight on the program was managed by the United States Air Force. The goal of the project was to break the sound barrier with a manned aircraft. On October 14th 1947 that was accomplished.[48, 37] Projects like this have continued ever since. Out of the X–Plane program the first aircrafts to fly at altitudes exceeding 100,000, 200,000 and 300,000 ft, along with the first aircrafts to fly at Mach 3, 4, 5, and 6 have been built and tested.[1]

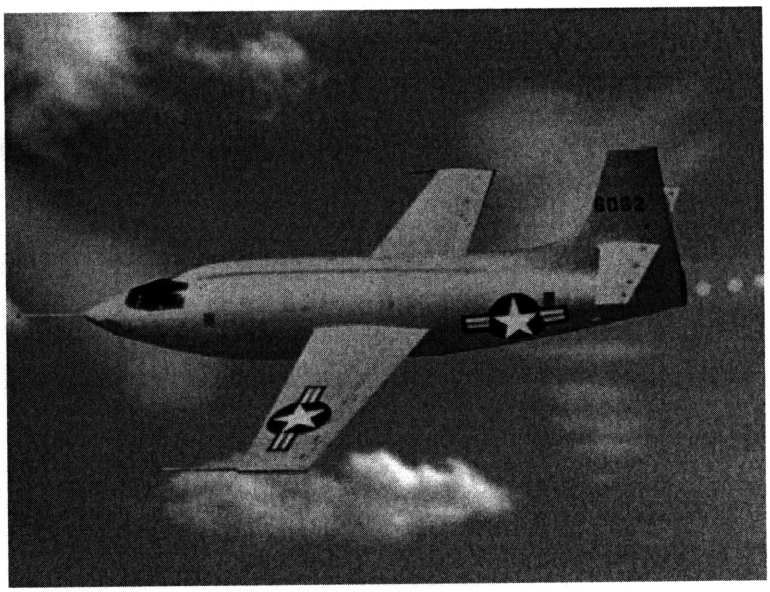

Figure 1-1: Bell X–1

One of the most notable projects to come out of the program is the X–15 aircraft, Figure 1-2. The program began in 1954 and 199 test flights were performed. The X–15 was designed with several research goals in mind. The major goal was to understand the effects of high speed atmosphere reentry. In the process the X–15 broke altitude and speed records with flights higher than 300,000 ft and at speeds in

[1] `http://history.nasa.gov/x1/appendixa1.html` Table A-1

excess of Mach 6.[30] The results of this project directly impacted the short 7 years before Alan Shepard was the first American in space.

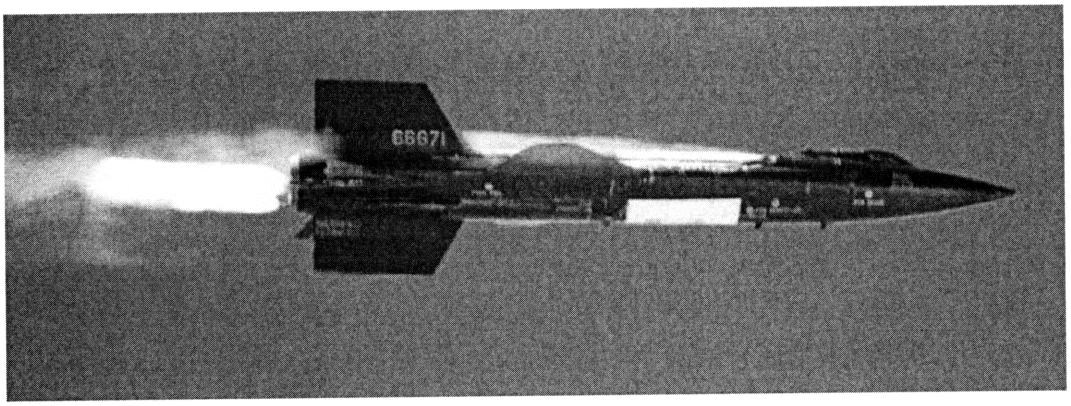

Figure 1-2: X-15

Two important characteristics of the X–15 program were the exploration of the hypersonic regime and the implementation of an adaptive algorithm in aircraft stabilization. "The Hypersonic Envelope, starts at a Mach number like 5 and extends to a Mach number or velocity as high as the imagination and technology will allow." [38] This quote by Richard Neumann illustrates the somewhat vague nature of the term "hypersonic". The hypersonic flight regime is particulary important for the X–43 as that is the defining characteristic that allows for the efficient combustion of the scramjet engine. This will be discussed in more detail in a subsequent section.

The adaptive control algorithm implemented in the X–15 project was designed by Minneapolis Honeywell Corp. It was referred to as a "Self–Adaptive" control system. The Self–Adaptive control system had a variable feedback gain on euler rates in order to maintain attitude stability in flight. The variable feedback gains were adjusted so as to minimize the error between the actual attitude of the aircraft and some ideal reference attitude. The adaptive controller decreased the tuning time necessary to gain schedule a classic controller over the entire flight envelope.[46, 18]

The adaptive algorithm from Honeywell was truly ahead of its time in implementation. However, it lacked the mathematical tools necessary to prove stability in a rigorous manner and relied on "rule of thumb" ideologies instead. This ended in tragedy however. On November 15, 1967 test flight 191 of 199 crashed above Delamar

Dry Lake.[30] Unbeknownst to the pilot there was an electrical malfunction and the aircraft began to deviate from the desired trajectory and a gross side–slip angle was building. Once off by 15° the pilot corrected for the mistake, then the aircraft drifted again, after several seconds of pilot corrections the aircraft interred a Mach 5 spin at an altitude of 230,000 ft.[30, 47] As the aircraft fell into more dense air it broke apart killing the pilot, Mike Adams. This crash put a holt on all adaptive control implementation for several decades, and not until recently has the idea been revisited. Now with more rigorous stability proofs.

In an attempt to pave the way for reusable and more affordable vehicles the X–43 program was initiated in order to conduct experiments in hypersonic vehicle system identification and inflight scramjet combustion. The first flight was in 2001, Figure 1-3.[36, 51] Airbreathing hypersonic engines are being considered because of the reduced weight of such systems when compared to rocket powered hypersonic vehicles. Rockets require that the oxidizer along with the fuel be carried up with the aircraft. Where as in a scramjet engine, the oxidizer is not needed. This can potentially increase the payload capabilities of scramjet powered vehicles.

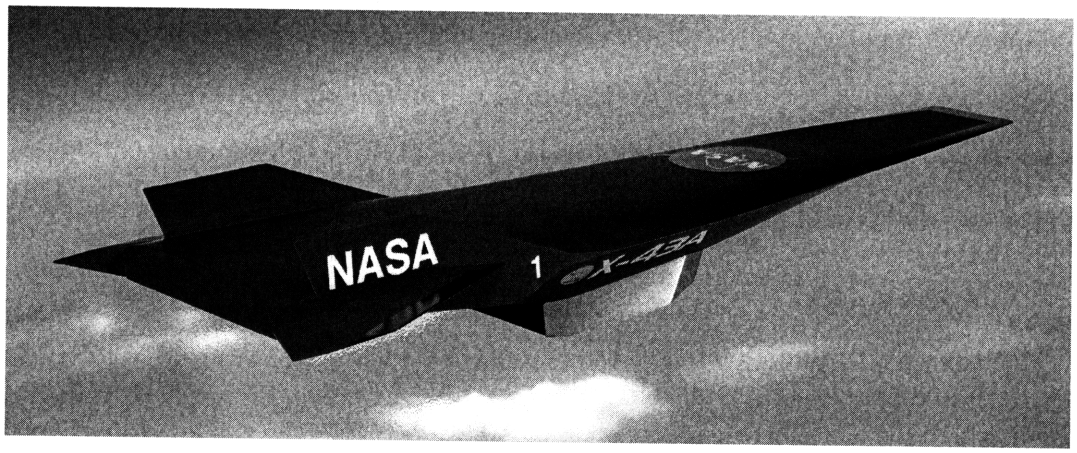

Figure 1-3: X–43 artistic rendering

1.2 Modelling of Hypersonic Vehicles

The X–43 could not launch from the ground and the scramjet engine was not operable unless at hypersonic speeds. The typical mission profile would be as follows. The X–

43 begins attached to the end of a Pegasus Rocket and both structures together would be carried under the wing of a B–52B, see Figure 1-4. The B–52B would carry the Pegasus booster system up to an altitude of 40,000 ft where the Pegasus booster would be dropped. The booster would then propel the X–43 to an altitude of 95,000 ft at some hypersonic speed where the X–43 would then be pushed off the end of the Pegasus Rocket. Then, depending on the mission objectives, the X–43 would carry out various tasks. This mission profile is illustrated in Figure 1-5. The dynamics of the X–43 after the Pegasus push–off are what this work pertains to. This flight condition will be referred to as the cruise condition for the X–43.

Figure 1-4: X–43 on Pegasus under B–52B [6]

Several attempts have been made to characterize the longitudinal dynamics of a hypersonic vehicle. One notable comprehensive analytical aeropropilsive–aeroelastic *Hypersonic Vehicle* (HSV) model is that proposed by Chavez and Schmidt in [10]. In that work a 2–D vehicle geometry was assumed; and with Newtonian theory, a 1–D isentropic scramjet model, and a lumped mass elastic model the HSV dynamics were formulated. Newtonian theory, however, is better suited for blunt bodies and becomes less accurate for slender bodies. Noting this fact, Bolender and Doman

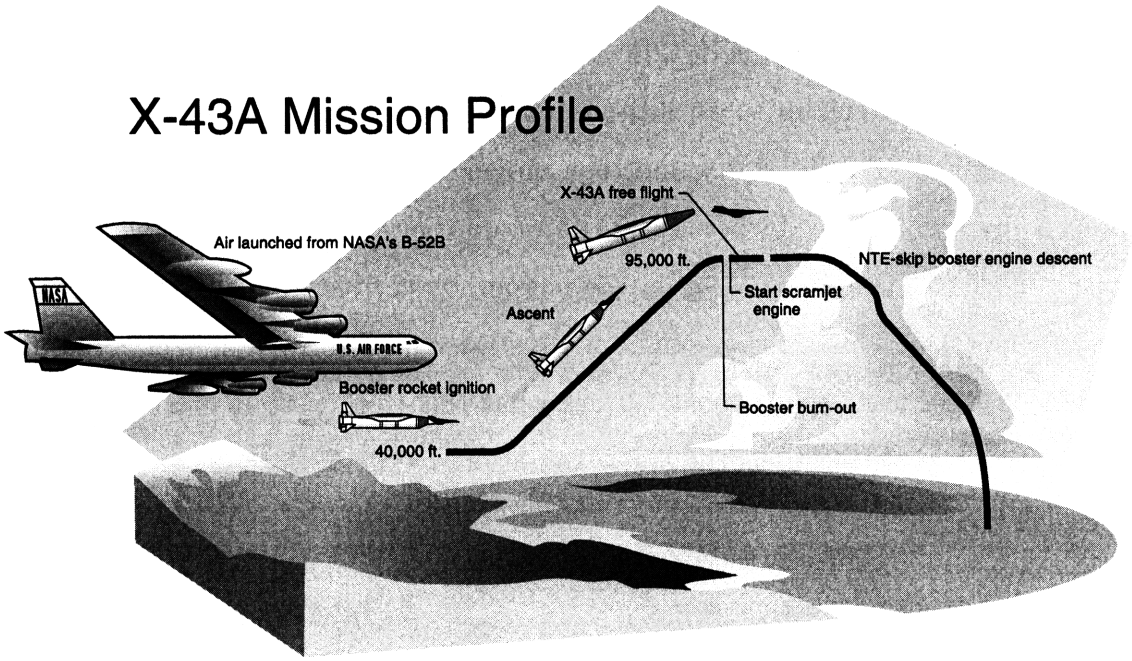

Figure 1-5: X–43 flight envelope [5]

in [7] propose an HSV model that builds upon the work by Chavez. Instead of Newtonian Impact theory, Oblique Shock theory is proposed for the compression of high speed air. Bolender and Doman's work incorporates the elastic effects with a double cantilever beem model, and the rigid–elastic dynamics are then obtained through a Lagrangian formulation. Doman and Bolender have recently built upon their work in [7] and included unsteady, thermal, and viscous effects as well as an updated elastic model.[9]. CFD–based characterizations have also been proposed such as that in [11].

1.3 Control Design

The Guidance, Navigation and Control of hypersonic vehicles are highly challenging tasks due to the fact that the dynamics of the airframe, propulsion and structure are highly integrated and highly interactive. Such a coupling makes it very difficult to model various components with a requisite degree of accuracy. This in turn makes

various control tasks including altitude and velocity command tracking in the cruise phase of the flight extremely difficult.

Notable works in the area of HSV control design are discussed here in. In [33], an adaptive linear-quadratic controller is deployed in the presence of structural modes and actuator dynamics, and is shown to track altitude and velocity commands in the presence of aerodynamic changes and actuator changes. The authors of [52] designed an adaptive sliding mode controller that tracks step commands in height and velocity while requiring limited state information. In [19] the authors employed both robust and adaptive techniques on a sequential loop closing methodology. The work in [31] focuses on elastic mode suppression through an adaptive notch filter technique. References [35], [49] and [50] not only focus on control design but also on robustness characteristics of the controller. Similar studies are carried out in this thesis in Chapter 5. Other notable works in the area of control of Hypersonic vehicles are References [34, 1, 26, 13, 12, 24, 41, 39, 23, 40, 42] and [32].

Uncertainty characterization is also important when determining the relative robustness characteristics of any given controller. Aircraft geometry and mass property uncertainties have been studied in [39]. Aerodynamics coefficient uncertainties were used in [40] and [33] to test the control algorithm; and inertial–elastic uncertainties were studied in [42] and [28].

1.4 Overview

In this work, a baseline controller is first developed that has *Proportional*, *Integral* and *Filter* components, commonly called a PIF controller.[44] An adaptive controller then augments to the baseline controller. It accommodates for aerodynamic uncertainties, center-of-gravity movements, actuator saturation and failures and is robust with respect to time–delays and elastic effects. The nonlinear rigid HSV model in [40] is used for control design and the nonlinear aeroelastic HSV model in [7] is used for controller evaluation. Time simulations are presented to illustrate the benefits of the adaptive algorithm. Analysis is also performed in order to study the resilience

of the controller to the uncertainties mentioned above for a set of closed-loop requirements that prevent excessive structural loading, poor tracking performance and engine stalls.[21, 22]

Chapter 2

Vehicle Modelling

The *Hypersonic Vehicle*, HSV, geometry used in this study is shown in Figure 2-1. This geometry is representative of the NASA X-43 aircraft. There are three control inputs for this vehicle, the elevator deflection δ_e, the canard deflection δ_c, and the equivalence ratio for the fuel in the scramjet ϕ. The canard was added in recent studies in order to increase the available bandwidth for the controller.[8, 40] It should be noted however that this control surface may not be physically realizable given the harsh environment in the forward of the aircraft. For that reason the HSV model is constructed so that the canard effects can easily be removed, so as to have a two input system. In order to obtain the physics based model proposed in this work the pressure

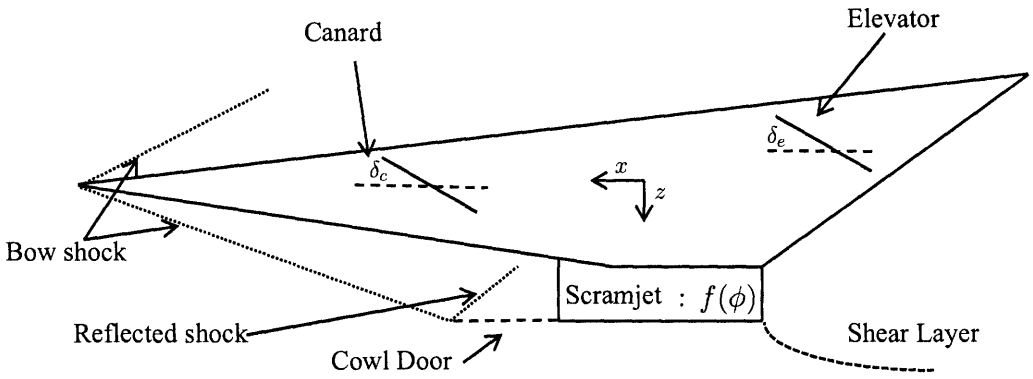

Figure 2-1: HSV side view with control inputs[7]

distribution around the aircraft must be defined. Then, the rigid(elastic) forces are obtained by integration of the pressure distribution over the surface(mode shapes)

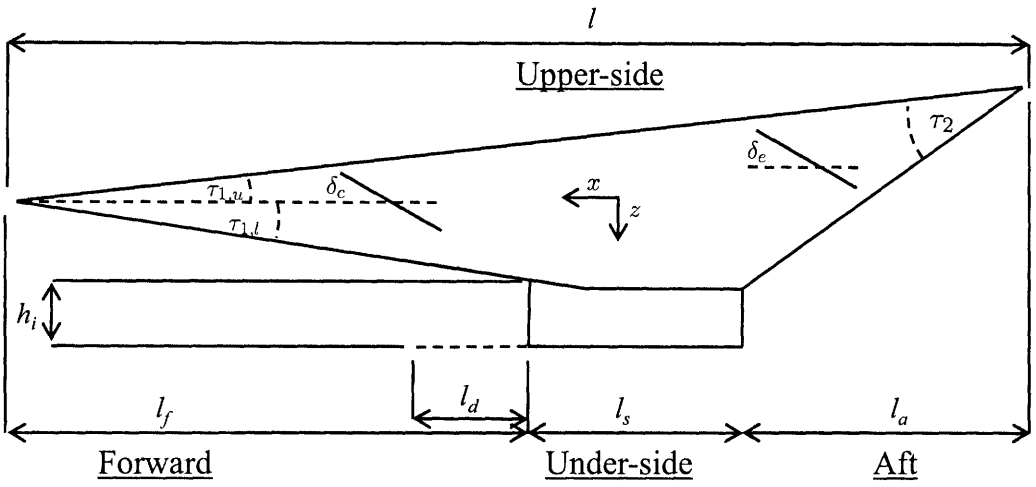

Figure 2-2: HSV side view with dimenion labels[7]

of the HSV. Given the simple geometry of the aircraft, a majority of the pressure distribution can be obtained by implementing Prandtl–Meyer expansion and oblique shock theory.

2.1 Oblique Shock and Expansion Wave Theory

Oblique shock theory is applicable when supersonic flow is turned over a concave surface, see Figure 2-3 for physical intuition. Given a prescribed turn angle δ_t the shock angle θ_s can be calculated with the following expression,

$$\sin^6\theta_s + b\sin^4\theta_s + c\sin^2\theta_s + d = 0, \tag{2.1}$$

where

$$\begin{aligned} b &= -\frac{M_1^2+2}{M_1^2} - \gamma\sin^2\delta_t \\ c &= \frac{2M_1^2+1}{M_1^4} + \left[\frac{(\gamma+1)^2}{4} + \frac{\gamma-1}{M_1^2}\right]\sin^2\delta_t \\ d &= -\frac{\cos^2\delta_t}{M_1^4}. \end{aligned} \tag{2.2}$$

In the previous expression M_1 denotes the mach number of the fluid before reaching the shock wave and γ represents the ratio of specific heats ($\gamma = C_p/C_v$). The shock angle is then determined by solving for the second root of Equation (2.1) with respect to $\sin^2\theta_s$. The pressure p, temperature T, and Mach number M, can then be obtained using the relations,

$$\frac{p_2}{p_1} = \frac{7M_1^2\sin^2\theta_s - 1}{6} \tag{2.3}$$

$$\frac{T_2}{T_1} = \frac{\left(7M_1^2\sin^2\theta_s - 1\right)\left(M_1^2\sin^2\theta_s + 5\right)}{36M_1^2\sin\theta_s} \tag{2.4}$$

$$M_2^2\sin^2(\theta_s - \delta_t) = \frac{M_1^2\sin^2\theta_s + 5}{7M_1^2\sin^2\theta_s - 1}. \tag{2.5}$$

where subscripts 1 and 2 denote pre and post shock values.[3]

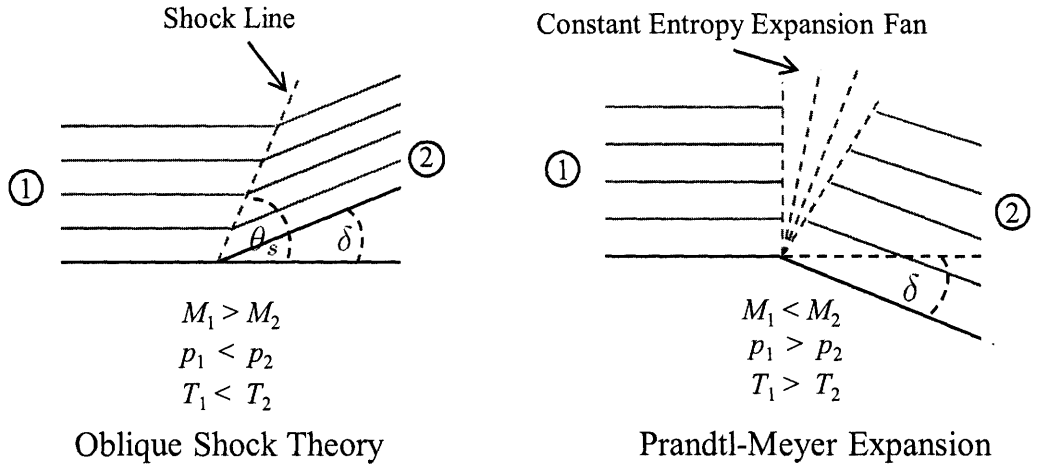

Figure 2-3: Visual aids for oblique shock and Prandtl–Meyer expansion.[2]

When the opposite scenario occurs and flow is turned over a convex corner, the flow expands. The properties of the gas are then characterized by Prandtl–Meyer expansion,

$$\delta_t = \nu(M_2) - \nu(M_1) \tag{2.6}$$

where

$$\nu(M) = \sqrt{\frac{\gamma+1}{\gamma-1}}\arctan\sqrt{\frac{\gamma+1}{\gamma-1}\left(M^2-1\right)}\arctan\sqrt{M^2-1}. \tag{2.7}$$

With the post expansion Mach number obtained, the remaining air properties can be

calculated as,[3]

$$\frac{p_2}{p_1} = \left[\frac{1+[(\gamma-1)/2]M_1^2}{1+[(\gamma-1)/2]M_2^2}\right]^{\gamma/(\gamma-1)} \tag{2.8}$$

$$\frac{T_2}{T_1} = \frac{1+[(\gamma-1)/2]M_1^2}{1+[(\gamma-1)/2]M_2^2}. \tag{2.9}$$

These theories can then be applied across the front, top and bottom of the aircraft in order to obtain the pressure distribution for the upper-surface, forward, underside, and inlet to the scramjet as well as the air properties around the canard and elevator.

2.2 Rigid Body Forces and Moments

Given the free stream Mach Number M_∞, temperature T_∞, and and air pressure p_∞, the location of the bow shock can be determined along with the upper body properties on the top of the air frame and the forward lower body properties, as shown in Figure 2-4. Note that the following subscript notation $(\cdot)_u$ and $(\cdot)_f$ will be used to denote upper–body properties and forward under–body properties respectively.

Once the pressures are determined as described above, the forces and moments on the upper–side of the HSV are found as,

$$F_{x,u} = -p_u l_u \tan\tau_{1,u} \tag{2.10}$$

$$F_{z,u} = p_u l_u \tag{2.11}$$

$$M_{y,u} = \tilde{z}_f F_{x,u} - \tilde{x}_f F_{y,u}, \tag{2.12}$$

where $\tilde{z}_u$ and $\tilde{x}_u$ are the differences between the geometric center of the upper panel (x_u,z_u) and the center of mass of the aircraft, $\tilde{x}_u = x_u - \bar{x}$ $\tilde{z}_u = z_u - \bar{z}$. The forces and

moments on the forward under–side are then found using the following expressions,

$$F_{x,f} = -p_f l_l \tan \tau_{1,l} \tag{2.13}$$

$$F_{z,f} = -p_f l_l \tag{2.14}$$

$$M_{y,f} = \tilde{z}_f F_{x,f} - \tilde{x}_f F_{y,f}, \tag{2.15}$$

with $\tilde{z}_f$ and $\tilde{x}_f$ having the same interpretation as above. The pressure is constant on the surface of the HSV behind the bow shock and it is for that reason that the forces are simply calculated using a single value for the pressure across the entire surface.

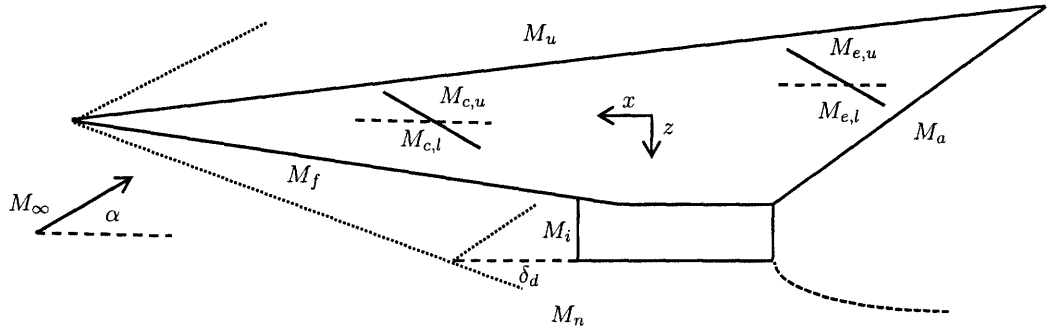

Figure 2-4: Mach Number Location Subscript Indexing

The air after passing through the bow shock on the under–side of the HSV will impinge on the cowl door, which protrudes in front of the scramjet engine. The cowl door is assumed to be adjustable and in this work it is assumed that the cowl door can be adjusted perfectly so as to maintain an on lip condition with the bow shock wave. Given this scenario, there will be a force exerted on the aircraft as the post bow shock air is turned parallel to the entrance of the scramjet,

$$F_{x,\text{inlet}} = \gamma M_f^2 p_f (1 - \cos(\tau_{1,l} + \alpha)) h_i \tag{2.16}$$

$$F_{z,\text{inlet}} = \gamma M_f^2 p_f \sin(\tau_{1,l} + \alpha) h_i \tag{2.17}$$

$$M_{y,\text{inlet}} = \tilde{z}_{\text{inlet}} F_{x,\text{inlet}} - \tilde{x}_{\text{inlet}} F_{z,\text{inlet}}. \tag{2.18}$$

Using geometry, one would find that the cowl door is adjusted using the following

expression,

$$l_d = l_f - (l_f \tan \tau_{1,l} + h_i) \cot(\delta_d - \alpha), \tag{2.19}$$

where δ_d is the relative angle between the bow shock and the cowl door, and α is the angle of attack of the aircraft.

The nacelle is the cowl door and the underside of the scramjet together, and properties of the aircraft under the nacelle are denoted as $(\cdot)_n$. The nacelle length is given as,

$$l_n = l_s + l_d.$$

The total force and moment imparted on the nacelle of the aircraft is determined by the following relations,

$$F_{z,n} = -p_n l_n \tag{2.20}$$

$$M_{y,n} = -F_{z,n} \tilde{x}_n, \tag{2.21}$$

where $\tilde{x}_n$ is distance between the center of the nacelle and the center of gravity of the aircraft, and p_n is calculated using either oblique shock theory or expansion theory depending on the angle of attack. Note that given the shock on lip condition, the properties for the nacelle are simply determined from the free stream air. If the shock on lip condition is not satisfied, the above relations do not hold.

Continuing to follow the path of the air, after passing through the bow shock and then the second shock from the reflection on the cowl door, the air will enter the scramjet engine. The scramjet is modelled as 1-D, and isentropic flow is assumed. The expressions necessary to incorporate the propulsion system were first introduced by Chavez and Schmidt.[10] The model for the scramjet is shown in Figure 2-5. After the free stream air impinges on the cowl it is turned upward parallel to the entrance of the scramjet. Oblique Shock theory can be used in order to determine the Mach Number at the Inlet from the Mach Number under the fore-body of the HSV.

The change in Mach number as the flow is compressed in the diffuser is calculated

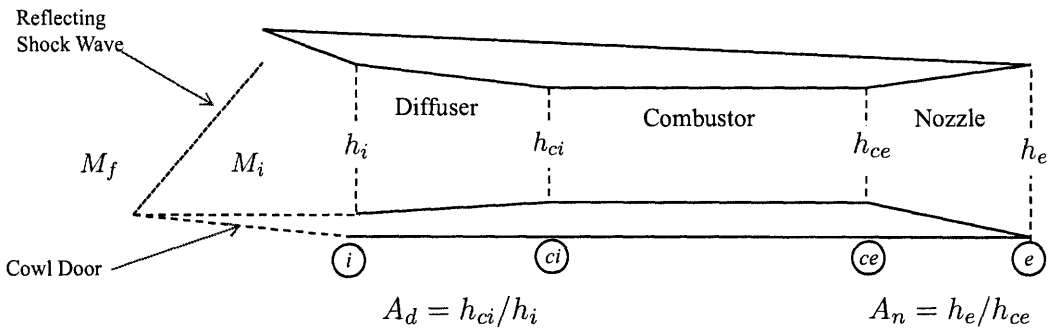

Figure 2-5: Scramjet Model[7]

as,

$$\frac{\left[1+[(\gamma-1)/2]M_{ci}^2\right]^{(\gamma+1)/(\gamma-1)}}{M_{ci}^2} = A_d^2\frac{\left[1+[(\gamma-1)/2]M_i^2\right]^{(\gamma+1)/(\gamma-1)}}{M_i^2} \tag{2.22}$$

where $(\cdot)_i$ denotes the inlet to the scramjet, $(\cdot)_{ci}$ denotes the combustor inlet, and A_d is the diffuser area ratio as shown in Figure 2-5. The air properties at the combustor inlet are calculated using Equations (2.8) and (2.9).

The combustor is modelled as a constant area duct with heat addition. This leads to the expression,

$$\frac{M_{ce}^2\left[1+[(\gamma-1)/2]M_{ce}^2\right]}{(\gamma M_{ce}^2+1)^2} = \frac{M_{ci}^2\left[1+[(\gamma-1)/2]M_{ci}^2\right]}{(\gamma M_{ci}^2+1)^2} + \frac{M_{ci}^2}{(\gamma M_{ci}^2+1)^2}\frac{\Delta T_{t_c}}{T_{ci}} \tag{2.23}$$

where the Mach number at the combustor exit M_{ce} is a function of the total temperature change across the combustor ΔT_{t_c}. The temperature and pressure at the combustor exit are then defined as

$$p_{ce} = p_{ci}\frac{1+\gamma M_{ci}^2}{1+\gamma M_{ce}^2} \tag{2.24}$$

$$T_{ce} = T_{ci}\left[\left(\frac{1+\gamma M_{ce}^2}{1+\gamma M_{ci}^2}\right)\frac{M_{ci}}{M_i}\right]^2 \tag{2.25}$$

An analytical expression relating the total temperature change across the com-

bustor to the equivalence ratio ϕ follows,

$$\frac{T_{t_{ce}}}{T_{t_{ci}}} = \frac{1 + H_f \eta_c f_{st} \phi / (c_p T_{t_{ci}})}{1 + f_{sT} \phi} \tag{2.26}$$

$$\Delta T_{t_c} = T_{t_{ce}} - T_{t_{ci}} \tag{2.27}$$

where η_c is the efficiency of the scramjet (0.9), f_{st} is the stoichiometric air-fuel ratio (0.0291), H_c is the heat of combustion for the fuel (LH2 at 51,500 BTU/lbm) and c_p is the specific heat of the fuel at constant pressure (0.24 BTU/(lbm°R).[25, 27, 4, 7] It is important to note that temperatures with subscript t are the total temperatures and all other temperatures referred to in this work are the static temperatures. The ratio of total temperature to static temperature can be obtained using the following,

$$\frac{T_t}{T} = 1 + \frac{\gamma - 1}{2} M^2. \tag{2.28}$$

The procedure for obtaining the Mach number for the air at the exit of the scramjet is similar to that of Equation (2.22),

$$\frac{\left[1 + [(\gamma - 1)/2] M_e^2\right]^{(\gamma+1)/(\gamma-1)}}{M_e^2} = A_n^2 \frac{\left[1 + [(\gamma - 1)/2] M_{ce}^2\right]^{(\gamma+1)/(\gamma-1)}}{M_{ce}^2}. \tag{2.29}$$

Using a control volume around the scramjet and applying the law of conservation of momentum, the total thrust from the scramjet can be obtained

$$\mathcal{T} = \dot{m}_a (V_e - V_\infty) + (p_e - p_\infty) h_e - (p_i - p_\infty) h_i. \tag{2.30}$$

The air upon leaving the scramjet will then expand along the aft of the aircraft and interact with the free stream air coming from the underside of the HSV. An analytical expression for the pressure on the aft of the scramjet as a function of the free stream air pressure was found by Chavez and Schmidt and is displayed below,

$$p_a = \frac{p_e}{1 + s_a / l_a (p_e / p_\infty - 1)} \tag{2.31}$$

where l_a is the length of the aft of the aircraft in the x–body direction and s_a is the length coordinate in the x–body direction. Integration of the aft body pressure along the back side of the aircraft results into the following expressions for the aft-body forces and moments,

$$F_{x,a} = p_\infty l_a \frac{p_e}{p_\infty} \frac{\log(p_e/p_\infty)}{(p_e/p_\infty) - 1} \tan(\tau_2 + \tau_{1,u}) \tag{2.32}$$

$$F_{z,a} = -p_\infty l_a \frac{p_e}{p_\infty} \frac{\log(p_e/p_\infty)}{(p_e/p_\infty) - 1} \tag{2.33}$$

$$M_{y,a} = \tilde{z}_a F_{x,a} - \tilde{x}_a F_{z,a} \tag{2.34}$$

where the pitching moment is calculated from the point of average pressure on the aft body panel. The point of average pressure can be calculated as $\bar{p}_a = \int_0^{l_a} p_a(s_a) \mathrm{d}s_a / l_a$. The center of pressure coordinates are then found by solving for x_a in the following expression $p_a(x_a) = \bar{p}_a$. Then the relative position of the center of pressure to the center of gravity of the HSV is trivial.

Two components of the total force acting on the HSV that have not been addressed yet are the forces from the canard and elevator. Depending on the angle of attack of the HSV and the relative positions of the canard and elevator the pressure surrounding the control surfaces can be determined from oblique shock or Prandtl–Meyer expansion. Once the pressures surrounding the canard are determined, the forces acting upon it are calculated as follows,

$$F_{x,c} = -(p_{c,l} - p_{c,u}) \sin \delta_c S_c \tag{2.35}$$

$$F_{z,c} = -(p_{c,l} - p_{c,u}) \cos \delta_c S_c \tag{2.36}$$

$$M_{y,c} = \tilde{z}_c F_{x,c} - \tilde{x}_c F_{z,c}. \tag{2.37}$$

The forces acting on the elevator have an identical set of equations and are shown

below for completeness,

$$F_{x,e} = -\left(p_{e,l} - p_{e,u}\right) \sin \delta_e S_e \tag{2.38}$$

$$F_{z,e} = -\left(p_{e,l} - p_{e,u}\right) \cos \delta_e S_e \tag{2.39}$$

$$M_{y,e} = \tilde{z}_e F_{x,e} - \tilde{x}_e F_{z,e}. \tag{2.40}$$

For the coordinates of the canard and elevator refer to Appendix A.1.

Thus far all of the forces and moments acting on the hypersonic vehicle that control the rigid–body dynamics have been expressed and therefore the total x–body force, z–body force and y–body moment are calculated as follows,

$$F_x = F_{x,u} + F_{x,f} + F_{x,\text{inlet}} + F_{x,a} + F_{x,e} + F_{x,c} \tag{2.41}$$

$$F_z = F_{z,u} + F_{z,f} + F_{z,\text{inlet}} + F_{z,n} + F_{z,a} + F_{z,e} + F_{z,c} \tag{2.42}$$

$$M_y = M_{y,u} + M_{y,f} + M_{y,\text{inlet}} + M_{y,n} + M_{y,a} + M_{y,e} + M_{y,c} + z_T \mathcal{T}. \tag{2.43}$$

As previously mentioned, this work also includes the elastic effects an the HSV dynamics. These effects are outlined in the following section.

2.3 Elastic Forces and Moments

The elastic effects are obtained by modelling the HSV as two fixed free beams. One beam free at the forward of the HSV and fixed at the center of gravity, and a second beam fixed at the center of gravity and free toward the aft. A visual representation of the above beam model is shown in Figure 2-6. It is important to note that the

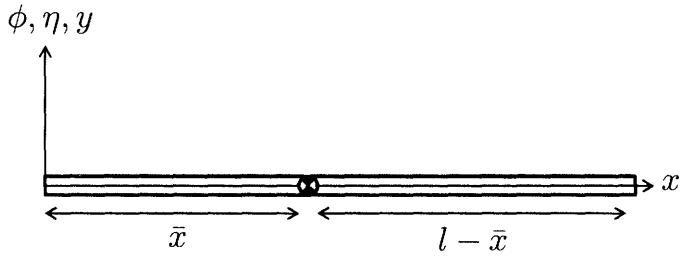

Figure 2-6: Elastic HSV beam model with coordinates.

coordinate system for the elastic model has up as positive, where in the rigid–body model down is positive.

2.3.1 Natural Modes of Vibration for a Fixed–Free Beam

Given the above flexible beam model for the HSV, and assuming that small deflections occur so that Hooke's Law can be used, the vertical deflection y is well defined as a function of space and time. It is governed by the following partial–differential equation,

$$EI\frac{\partial^4 y(x,t)}{\partial x^4} + \hat{m}\frac{\partial^2 y(x,t)}{\partial t^2} = 0, \tag{2.44}$$

where $\hat{m}$ is the constant mass density and EI is the constant Young's modulus area moment of inertia. For values of these parameters refer to Tables A.1 and A.2. It is assumed that the solution to (2.44) can be separated in space and time so that,

$$y(x,t) = \phi(x)f(t). \tag{2.45}$$

Given this, (2.44) can be separated as follows,

$$EI\frac{\mathrm{d}^4\phi(x)}{\mathrm{d}x^4} - \omega^2\hat{m}\phi(x) = 0 \tag{2.46}$$

$$\frac{\mathrm{d}f(t)}{\mathrm{d}t^4} + \omega^2 f(t) = 0. \tag{2.47}$$

For notational convenience the following substitution is made $\beta^4 = \omega^2\hat{m}/EI$. Equation (2.46) is now of the form,

$$EI\frac{\mathrm{d}^4\phi(x)}{\mathrm{d}x^4} - \beta^4\phi(x) = 0. \tag{2.48}$$

The solution to the ordinary–differential equation in (2.48) is referred to as the mode shape and has a solution of the following form,

$$\phi(x) = A\sin\beta x + B\cos\beta x + C\sinh\beta x + D\cosh\beta x. \tag{2.49}$$

The equations given thus far are for a generic free–fixed beam. The following discussion will pertain to the component of the elastic model forward of the HSV's center of gravity, and a later discussion will pertain to the aft section of the beam model.

The modal analysis for the forward components will be denoted with a subscript f. In order to solve for the unknown constants in (2.49) the following boundary conditions are given. Two geometric boundary conditions arise,

$$\phi_f(\bar{x}) = 0 \tag{2.50}$$

$$\phi_f'(\bar{x}) = 0. \tag{2.51}$$

The geometric boundary conditions arise from the fact that the beam model is fixed at the center of gravity of the HSV. Also, a pair of natural boundary conditions arise at the free end of the beam,

$$\phi''(0) = 0 \tag{2.52}$$

$$\phi'''(0) = 0. \tag{2.53}$$

The natural boundary conditions arise from the fact that the bending moment and shear force are both zero at the free end. Substitution of the four boundary conditions for the forward beam into the mode shape function described in (2.49), result into the following relation,

$$\cos\beta_f\bar{x}\cosh\beta_f\bar{x} = -1. \tag{2.54}$$

There are infinitely many solutions for β_f in (2.54). The infinitely many solutions relate to the fact that a non finite number of modes determine the flexible nature of a beam. For this study only the smallest value of β_f was used and thus, only one bending mode will be incorporated for the forward beam. Note, that the same is done for the aft beam as well. Substitution of the solution β_f into (2.49) results into the

following expression for the forward beam mode shape,

$$\begin{aligned}\phi_f =& A_f[(\sin\beta_f\bar{x} - \sinh\beta_f\bar{x})(\sin\beta_f x + \sinh\beta_f x) \\ &+ (\cos\beta_f\bar{x} + \cosh\beta_f\bar{x})(\cos\beta_f x + \cosh\beta_f x)],\end{aligned} \tag{2.55}$$

where A_f is a scaling factor that is chosen so as to mass normalize the mode shape and is determined by the following orthogonal solution,

$$\int_0^{\bar{x}} \hat{m}_f\phi_f(x)\phi_f(x)\mathrm{d}x = 1. \tag{2.56}$$

A similar approach was taken for the aft cantilever beam. With its unique set of four boundary conditions, the following relation results

$$\cos(\beta_a(l-\bar{x}))\cosh(\beta_a(l-\bar{x})) = -1, \tag{2.57}$$

so that the aft beam has a mode shape of the following form,

$$\begin{aligned}\phi_a =& A_a[(\sin\beta_a(l-\bar{x}) - \sinh\beta_a(l-\bar{x}))(\sin\beta_a(x-\bar{x}) - \sinh\beta_a(x-\bar{x})) \\ &+ (\cos\beta_a(l-\bar{x}) + \cosh\beta_a(l-\bar{x}))(\cos\beta_a(x-\bar{x}) - \cosh\beta_a(x-\bar{x}))].\end{aligned} \tag{2.58}$$

The aft beam is also mass normalized, and A_a is solved for in the following,

$$\int_{\bar{x}}^{l} \hat{m}_a\phi_a(x)\phi_a(x)\mathrm{d}x = 1. \tag{2.59}$$

Using the above approach, the following values were obtained for the forward and aft beams,

$$\begin{aligned}A_f &= 0.0283 \text{ ft} \\ A_a &= -0.0256 \text{ ft} \\ \beta_f &= 0.0341 \text{ ft}^{-1} \\ \beta_a &= 0.0417 \text{ ft}^{-1}.\end{aligned}$$

A visual representation of the combined forward and aft mode shapes as described in (2.55) and (2.58) is shown in Figure 2-7.

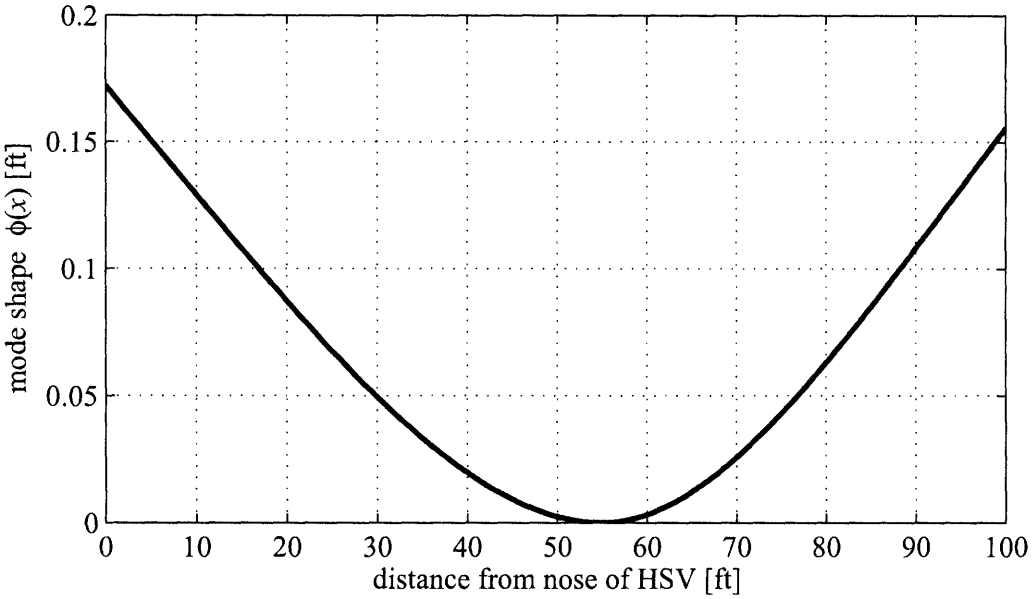

Figure 2-7: Forward and aft mode shape.

2.3.2 Forced Modal Response

The forced response associated with (2.44) is of the form,

$$EI\frac{\partial^4 y(x,t)}{\partial x^4} + \hat{m}\frac{\partial^2 y(x,t)}{\partial t^2} = p(x,t) + P_j(x,t)\delta(x - x_j), \tag{2.60}$$

where p denotes pressure and P is a point load. The above equation has solutions for y as,

$$y(x,t) = \sum_{k=1}^{\infty} \phi_k(x)\eta_k(t). \tag{2.61}$$

where the infinite summation over k illustrates the fact that there are infinitely many modes for a fixed–free beam. Do not confuse that with the subscripts f and a. The discussion thus far has not distinguished between forward and aft, and is of a generic flavor. The η terms will later be regarded as the flexible state variables, and are

governed by the following second order equation

$$\ddot{\eta}_k + \omega_k^2 \eta_k = N_k(t) \tag{2.62}$$

where N_k is the modal force defined as,

$$N_k(t) = \int \phi_k(x) p(x,t) \mathrm{d}x + \sum_{j=1}^{l} \phi_k(x_j) P_j(t). \tag{2.63}$$

Once again, the flexible model used in this work only pertains to the first bending modes for each beam. Application of (2.63) to the forward and aft beams results in the following force relations

$$N_f(t) = -\int_0^{\bar{x}} \phi_f(x) p(x,t) \mathrm{d}x + (-\phi_f(x_c) F_{z,c}(t)) \tag{2.64}$$

$$N_a(t) = -\int_{\bar{x}}^{l} \phi_a(x) p(x,t) \mathrm{d}x + (-\phi_a(x_e) F_{z,e}(t)). \tag{2.65}$$

Notice the minus signs in the above expression. The flexible beam model coordinate system denotes up as positive, where as the coordinate system for the rigid–body dynamics assumes down to be positive.

2.4 Equations of Motion

Two distinct aircraft models will be introduced in this study. One aircraft model will incorporate the flexible effects and will be used for controller evaluation, and as so will be referred to as the *Evaluation Model* (EM). The second model will only include the rigid–body effects and will be used for control design, and will be referred to as the *Design Model* (DM). The construction and implementation of these models is discussed below.

2.4.1 Evaluation Model

Using Lagrange's Equations, the equations of motion of the flexible hypersonic vehicle can be derived as follows,[7]

$$
\begin{aligned}
F_x &= m\dot{U} + mQW + mg\sin\theta + \dot{Q}(\lambda_a\eta_a + \lambda_f\eta_f) + 2Q(\lambda_a\dot{\eta}_a + \lambda_f\dot{\eta}_f) \\
F_z &= m\dot{W} - mQU - mg\cos\theta + \lambda_a\ddot{\eta}_a + \lambda_f\ddot{\eta}_f - Q^2(\lambda_a\eta_a + \lambda_f\eta_f) \\
M_y &= (I_{yy} + \eta_a^2 + \eta_f^2)\dot{Q} + (\dot{U} + QW)(\lambda_a\eta_a + \lambda_f\eta_f) + 2Q(\eta_a\dot{\eta}_a + \eta_f\dot{\eta}_f) - \psi_a\ddot{\eta}_a - \psi_f\ddot{\eta}_f \\
N_f &= \ddot{\eta}_f + (\dot{W} - QU)\lambda_f - \dot{Q}\psi_f + 2\zeta\omega_f\dot{\eta}_f + (\omega_f^2 - Q^2)\eta_f \\
N_a &= \ddot{\eta}_a + (\dot{W} - QU)\lambda_a - \dot{Q}\psi_a + 2\zeta\omega_a\dot{\eta}_a + (\omega_a^2 - Q^2)\eta_a.
\end{aligned}
\tag{2.66}
$$

where

$$
\begin{aligned}
\lambda_f &= \int_0^{\bar{x}} \hat{m}_f\phi_f(x)dx \\
\lambda_a &= \int_{\bar{x}}^{l} \hat{m}_a\phi_a(x)dx \\
\tilde{\psi}_f &= \int_0^{\bar{x}} (x - \bar{x})\hat{m}_f\phi_f(x)dx \\
\tilde{\psi}_a &= \int_{\bar{x}}^{l} (x - \bar{x})\hat{m}_a\phi_a(x)dx.
\end{aligned}
$$

The left hand side of the equation contains the rigid and elastic forces and the pitching moment. These forces in turn depend on the attitude of the aircraft as well as the three control inputs. On the right hand sides of the equations are the constants, elastic coefficients and the state variables of the aircraft in the body axes. The state variables in the body axes are: pitch angle θ, pitch rate Q, body axis horizontal speed U, and body axis vertical speed W, along with the four generalized elastic variables η_f, $\dot{\eta}_f$, η_a and $\dot{\eta}_a$. Subscripts f and a correspond to the forward and aft of the aircraft respectively. The forces and moments on the left hand side are determined using rigid–body forces in (2.41)–(2.43) and the elastic force relations in (2.64) and (2.65). It is advantageous as well to know the height, h, of the aircraft. Therefore,

the following kinematic relation,

$$\dot{h} = U \sin\theta - W \cos\theta \tag{2.67}$$

is introduced.

The implementation of Equation (2.66) is cumbersome and slow on any computer. Some of the solutions for obtaining the pressure distribution and subsequent forces on the hypersonic vehicle require solving nonlinear equations. A more implementable aircraft model is obtained through the transformation of the above system to the stability axis and then the subsequent curve fitting of the forces and moments to that of an algebraic relation. This increases the ease of implantation of the aircraft model, and greatly reduces computation time. Equation (2.66) can be transformed to the stability axis with the following coordinate transformation equations,

$$\begin{aligned} \alpha &= W/U \\ V^2 &= U^2 + W^2 \\ \dot{V} &= (U\dot{U} + W\dot{W})/V \\ \dot{\alpha} &= (U\dot{W} - W\dot{U})/V \end{aligned} \tag{2.68}$$

where α is the angle of attack and V is the velocity of the HSV. The relationship between the stability axes variables and body axes variables is illustrated in Figure2-8.

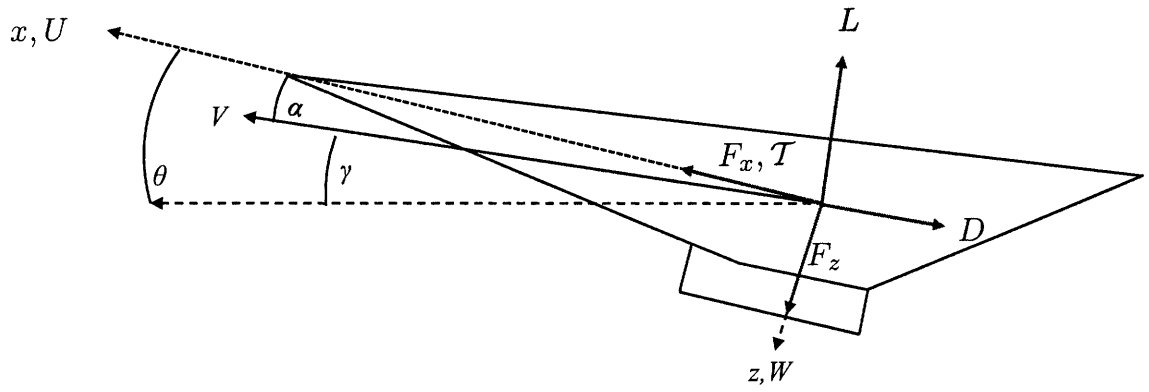

Figure 2-8: Axes of the HSV

The transformation to the stability axes was performed and extra coupling between elastic variables and state derivatives was neglected in order to obtain the following relations, [40]

$$\begin{aligned}
\dot{V} &= (\mathcal{T}\cos\alpha - D)/m - g\sin\gamma \\
\dot{\alpha} &= -(\mathcal{T}\sin\alpha + L)/mV + q + g\cos\gamma/V) \\
\dot{q} &= (M_y + \tilde{\psi}_f\ddot{\eta}_f + \tilde{\psi}_a\ddot{\eta}_a)/I_{yy} \\
\dot{h} &= V\sin\gamma \\
\dot{\theta} &= q \\
k_f\ddot{\eta}_f &= -2\zeta_f\omega_f\dot{\eta}_f - \omega_f^2\eta_f + N_f - \tilde{\psi}_f M/I_{yy} - \tilde{\psi}_f\tilde{\psi}_a\ddot{\eta}_f/I_{yy} \\
k_a\ddot{\eta}_a &= -2\zeta_a\omega_a\dot{\eta}_a - \omega_a^2\eta_a + N_a - \tilde{\psi}_a M_y/I_{yy} - \tilde{\psi}_f\tilde{\psi}_a\ddot{\eta}_a/I_{yy}
\end{aligned} \tag{2.69}$$

where $\gamma = \theta - \alpha$, $k_f = 1 + \tilde{\psi}_f/I_{yy}$ and $k_a = 1 + \tilde{\psi}_a/I_{yy}$. In order to obtain the Thrust $\mathcal{T}$, Lift L, Drag D and Moment M_y the following expressions are used:

$$\begin{aligned}
L &= \frac{1}{2}\rho V^2 S C_L \\
D &= \frac{1}{2}\rho V^2 S C_D \\
T &= C_{\mathcal{T}} \\
M_y &= z_{\mathcal{T}}\mathcal{T} + \frac{1}{2}\rho V^2 S\bar{c}C_M \\
N_f &= C_{N_f} \\
N_a &= C_{N_a}
\end{aligned} \tag{2.70}$$

with the above coefficients $C_{(\cdot)}$ defined as follows:

$$\begin{aligned}
C_L &= C_L^{\alpha}\alpha + C_L^{\delta_e}\delta_e + C_L^{\delta_c}\delta_c + C_L^0 \\
C_M &= C_M^{\alpha^2}\alpha^2 + C_M^{\alpha}\alpha + C_M^{\delta_e}\delta_e + C_M^{\delta_c}\delta_c + C_M^0 \\
C_D &= C_D^{\alpha^2}\alpha^2 + C_D^{\alpha}\alpha + C_D^{\delta_e^2}\delta_e^2 + C_D^{\delta_e}\delta_e + C_D^{\delta_c^2}\delta_c^2 + C_D^{\delta_c}\delta_c + C_D^0 \\
C_{\mathcal{T}} &= (\beta_1\phi + \beta_2)\alpha^3 + (\beta_3\phi + \beta_4)\alpha^2 + (\beta_5\phi + \beta_6)\alpha + (\beta_7\phi + \beta_8) \\
C_{N_f} &= C_{N_f}^{\alpha^2}\alpha^2 + C_{N_f}^{\alpha}\alpha + C_{N_f}^{\delta_c}\delta_c + C_{N_f}^0 \\
C_{N_a} &= C_{N_a}^{\alpha^2}\alpha^2 + C_{N_a}^{\alpha}\alpha + C_{N_a}^{\delta_e}\delta_e + C_{N_a}^0
\end{aligned} \tag{2.71}$$

where S is the projected area of the HSV in the x-y plane, $\bar{c}$ is the average width of the aircraft and ρ is the density of the air. The curve fitting of the aircraft model in Equation (2.69) was performed by the authors in [40] and [20]. The coefficient values used for implantation can be found in Table A.2.

It is clear from Equation (2.69) that there is significant coupling between the pitch rate and the elastic states of the model. The complexity in turn poses a significant challenge for developing a control design.

2.4.2 Design Model

Only the rigid–body states of the aircraft will be accessible for aircraft design and it is not clear what role the unsteady or elastic effects will have on the aircraft. For this reason the controller will be designed with no knowledge of such nonlinearities or complexities, and will simply be robust with respect to the unknown states. Thus the Design Model will have the following governing equations,

$$\begin{aligned}
\dot{V} &= (\mathcal{T}\cos\alpha - D)/m - g\sin\gamma \\
\dot{\alpha} &= (-\mathcal{T}\sin\alpha - L)/mV + q + g\cos\gamma/V) \\
\dot{q} &= M_y/I_{yy} \\
\dot{h} &= V\sin\gamma \\
\dot{\theta} &= q.
\end{aligned} \tag{2.72}$$

The Design Model is obtained by simply removing the elastic effects from the aircraft model in (2.69). It should be noted that Equation (2.72) is the set of governing equations for the decoupled longitudinal dynamics of any rigid aircraft.[45][1] The Thrust $\mathcal{T}$, Lift L, Drag D and Moment M_y have the same relations as the Evaluation Model and are defined by Equations (2.70) and (2.71).

2.4.3 Actuator Dynamics

Actuator dynamics will also be incorporated into the design and evaluation models. These can be described as follows:

$$\begin{aligned} \ddot{\phi} &= -2\zeta_\phi \omega_\phi \dot{\phi} - \omega_\phi^2 \phi + \omega_\phi \phi_{\text{cmd}} \\ \ddot{\delta}_e &= -2\zeta_\delta \omega_\delta \dot{\delta}_e - \omega_\delta^2 \delta_e + \omega_\delta \delta_{e,\text{cmd}} \\ \ddot{\delta}_c &= -2\zeta_\delta \omega_\delta \dot{\delta}_c - \omega_\delta^2 \delta_c + \omega_\delta \delta_{c,\text{cmd}} \end{aligned} \tag{2.73}$$

with $\zeta_\phi = 1$, $\zeta_\delta = 1$, $\omega_\phi = 10$ and $\omega_\delta = 20$.

[1] In Stengel's 2004 *Aircraft Dynamics* the equations of motion are found on page 240

Chapter 3

Controller Design

The control structure proposed has a combination of feedforward input, nominal feedback, and adaptive feedback terms. The HSV model is linearized around a desired trim point. Using the linear model an LQ regulator is then designed. Uncertainties along with actuator saturation are then introduced and an adaptive control structure is then explored that adjusts to the model uncertainties and maintains stability even with the actuator saturation.

3.1 Linear Model

The underlying design model, described by the DM in (2.72) and the actuator dynamics in (2.73) can be expressed compactly as a nonlinear model

$$\dot{X} = f(X, U), \tag{3.1}$$

where X is the state vector and U contains the exogenous inputs ϕ_{cmd} and $\delta_{e,\text{cmd}}$. In order to facilitate the control design, we linearize these equations to obtain the following:

$$\dot{x}_p = A_p x_p + B_p u + \varepsilon(t), \tag{3.2}$$

where ε is the linearization error, which is assumed to be small,

$$A_p = \left.\frac{\partial f(X,U)}{\partial X}\right|_{\substack{X=X_0 \\ U=U_0}}, \quad B_p = \left.\frac{\partial f(X,U)}{\partial U}\right|_{\substack{X=X_0 \\ U=U_0}}, \tag{3.3}$$
$$x_p = X - X_0, \text{ and } u = U - U_0.$$

The linear state x_p contains the perturbation states, $[\Delta V\ \Delta\alpha\ \Delta q\ \Delta h\ \Delta\theta\ \Delta\dot{\phi}\ \Delta\phi\ \Delta\dot{\delta}_e\ \Delta\delta_e]^\mathsf{T}$ and u is the command input perturbation vector, $[\Delta\phi_{\text{cmd}}\ \Delta\delta_{e,\text{cmd}}]^\mathsf{T}$.

Integral error states will be augmented to the linear model of the HSV for command following purposes. The reference command , r, will be given in $h - V$ space and is constructed as

$$r = [\Delta V_{\text{ref}}\ \ \Delta h_{\text{ref}}]^\mathsf{T} \tag{3.4}$$

Denoting an output $y = [\Delta V\ \ \Delta h]^\mathsf{T}$ an integral error state e_I can be expressed as

$$e_I = \int (y - r)d\tau = \int (Hx_p - r)d\tau, \tag{3.5}$$

where H is a selection matrix. In addition to error augmentation, the actuator inputs will be explicitly incorporated into the linear model as states, and a new input v is defined as

$$v = \dot{u}. \tag{3.6}$$

By augmenting both the command following error in (3.5) and actuator inputs in (3.6) to the linear system in (3.2) the overall system to be controlled becomes,

$$\underbrace{\begin{bmatrix} \dot{x}_p \\ \dot{e}_I \\ \dot{u} \end{bmatrix}}_{\dot{x}} = \underbrace{\begin{bmatrix} A_p & 0 & B_p \\ H & 0 & 0 \\ 0 & 0 & 0 \end{bmatrix}}_{A} \underbrace{\begin{bmatrix} x_p \\ e_I \\ u \end{bmatrix}}_{x} + \underbrace{\begin{bmatrix} 0 \\ 0 \\ I \end{bmatrix}}_{B} v + \underbrace{\begin{bmatrix} 0 \\ -I \\ 0 \end{bmatrix}}_{B_{cmd}} r, \tag{3.7}$$

which can be compactly expressed as,

$$\dot{x} = Ax + Bv + B_{cmd}r. \tag{3.8}$$

3.2 Baseline Controller

The baseline controller is designed so that the output y will follow a given reference signal r in the h–V space. At steady state it is clear that the error term e_I will have reached some constant value, so that $\dot{e}_I$ is now zero. With that, the plant state x_p will have reached some ideal x_p^* with some ideal input u^*, so that,

$$\begin{bmatrix} 0 \\ r \end{bmatrix} = \begin{bmatrix} A_p & B_p \\ H & 0 \end{bmatrix} \begin{bmatrix} x_p^* \\ u^* \end{bmatrix}. \tag{3.9}$$

With the following construction,

$$\begin{aligned} G &= \begin{bmatrix} A_p & B_p \\ H & 0 \end{bmatrix}^{-1} \\ &= \begin{bmatrix} G_{11} & G_{12} \\ G_{21} & G_{22} \end{bmatrix} \end{aligned} \tag{3.10}$$

and with some algebra we find that,

$$\begin{aligned} x_p^* &= G_{12} r \\ u^* &= G_{22} r. \end{aligned} \tag{3.11}$$

We now define,

$$\begin{aligned} \tilde{x}_p &= x_p - x_p^* \\ \tilde{u} &= u - u^* \end{aligned} \tag{3.12}$$

and collecting terms compactly,

$$\tilde{x} = \left[\tilde{x}_p^\mathsf{T} \; e^\mathsf{T} \; \tilde{u}^\mathsf{T}\right]^\mathsf{T} \tag{3.13}$$

The linear system of (3.8) can now been cast into that of an LQ regulator of the following form,[1]

$$\dot{\tilde{x}} = A\tilde{x} + Bv. \tag{3.14}$$

A linear quadratic cost function is then chosen as

$$J = \int (\tilde{x}^{\mathsf{T}} Q \tilde{x} + v^{\mathsf{T}} R v) d\tau, \tag{3.15}$$

where Q and R are suitably chosen positive definite matrices.[2] The nominal feedback gain is then selected as,

$$K = \underset{K}{\operatorname{argmin}} \{ J(v, \tilde{x}, Q, R) \mid v = K^{\mathsf{T}} \tilde{x} \}. \tag{3.16}$$

Through the expansion of $\tilde{x}$ the feedforward control gain can be extracted and leads to a baseline control design of the following form:

$$\begin{aligned} v =& K^{\mathsf{T}} \tilde{x} \\ =& [K_1 \; K_2 \; K_3] \left[\tilde{x}_p^{\mathsf{T}} \; e^{\mathsf{T}} \; \tilde{u}^{\mathsf{T}} \right]^{\mathsf{T}} \\ =& (-K_1 G_{12} - K_3 G_{22}) r + K_1 x_p + K_2 e + K_3 u \\ =& K_{ff} r + K^{\mathsf{T}} x \end{aligned} \tag{3.17}$$

Noting that the components of x include: state vector x_p, the integral error e_I, and control input u, it follows that the baseline controller has Proportional, Integral, and Filter components. Leading to a PIF-LQ regulator as first introduced in [43] with more details given in [44] and [45]. The PIF control structure is shown in Figures 3-1 and 3-2.

[1]The construction of $\tilde{x}$ is covered in great detail in Reference [44] page 523 and PIF control structure on pages 528-531.

[2]For more details pertaining to the values chosen for Q and R refer to Appendix C.

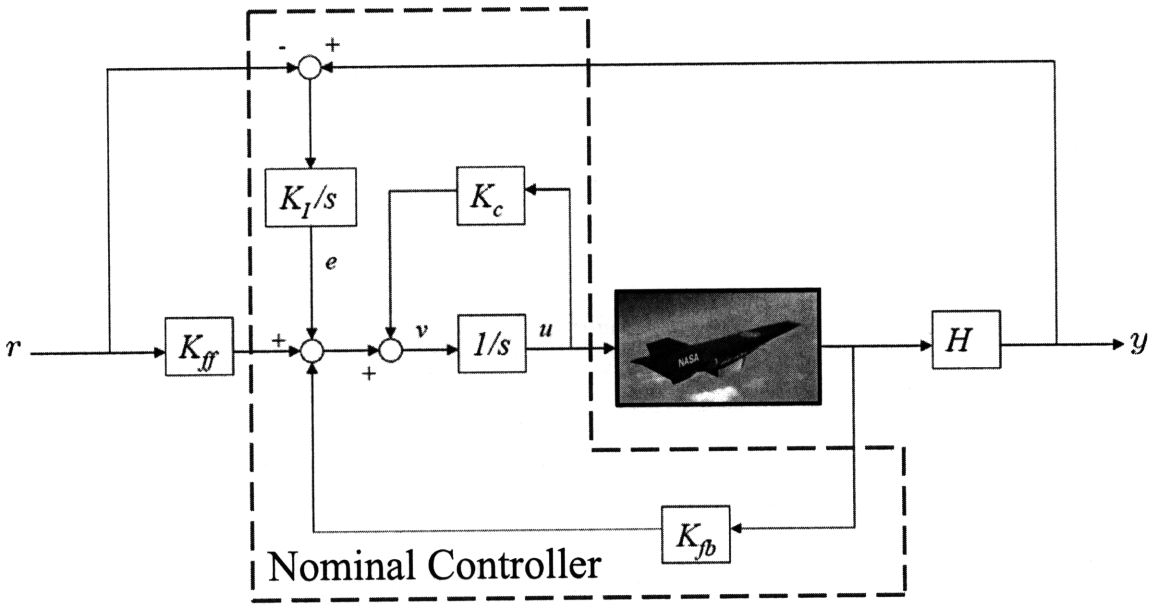

Figure 3-1: PIF control structure
[33, 43, 44, 45]

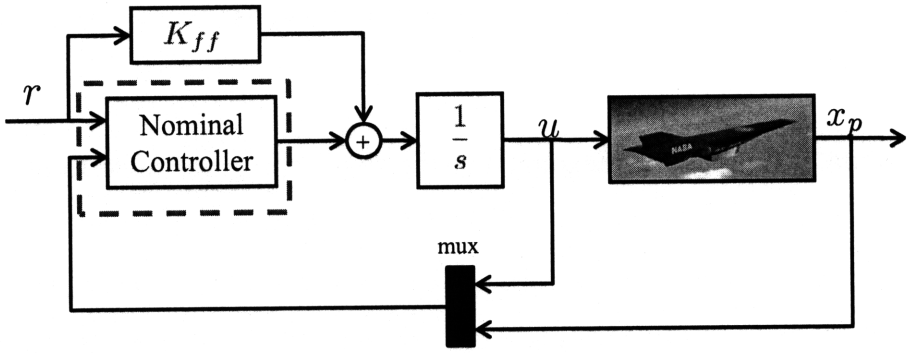

Figure 3-2: Nominal control structure

3.3 Uncertainties and Actuator Saturation

We now introduce two classes of uncertainties, parametric and unmodeled. The former case is represented as

$$A_{p,\text{uncertain}} = A_p(\lambda)$$

$$B_{p,\text{uncertain}} = B_p\Lambda$$

where λ is a vector that accounts for various aerodynamic uncertainties that may occur causing the underlying aerodynamic forces and moments to be perturbed. The

specific construction of λ is shown,

$$\lambda = \begin{bmatrix} \lambda_m & \lambda_L & \lambda_M & \lambda_{CG} \end{bmatrix}^T$$

where:

- λ_m: Multiplicative uncertainty in the inertial properties, $m = \lambda_m m_0$, and $I_{yy} = \lambda_m I_{yy,0}$ where
- λ_L: Multiplicative uncertainty in lift, $C_L^\alpha = \lambda_L C_{L,0}^\alpha$.
- λ_M: Multiplicative uncertainty in pitching moment, $C_M^\alpha = \lambda_M C_{M,0}$.
- λ_{CG}: Longitudinal distance between the neutral point and the center of gravity divided by the length l will be denoted as λ_{CG}. While a negative value of λ_{CG} denotes that the CG has been moved backwards, positive values denote a forward CG movement.

Capital lambda, Λ, is a 2x2 diagonal matrix that represents uncertainties in the actuator that may occur due to damages or failures, leading to loss of effectiveness.

Unmodeled uncertainties include the flexible effects, which are neglected in the design model, as well as time-delays, such as computational lags. If the unmodeled uncertainties and linearization errors are neglected, the underlying plant can be expressed as

$$\dot{x}_p = A_p(\lambda)x_p + B_p\Lambda u. \tag{3.18}$$

In addition to the above uncertainties, our studies also include magnitude saturation in the actuators. This is accounted for with the inclusion of a rectangular saturation function $R_s(u)$ where the i–th component is defined as, [29]

$$R_{s_i} = \begin{cases} u_i & \text{if } u_{\min_i} \leq u_i \leq u_{\max_i}, \\ u_{\max_i} & \text{if } u_i > u_{\max_i}, \\ u_{\min_i} & \text{if } u_i < u_{\min_i} \end{cases} \tag{3.19}$$

for $i = 1, 2$.

A visual representation of the uncertainties and saturation effects is shown in Figure 3-3.

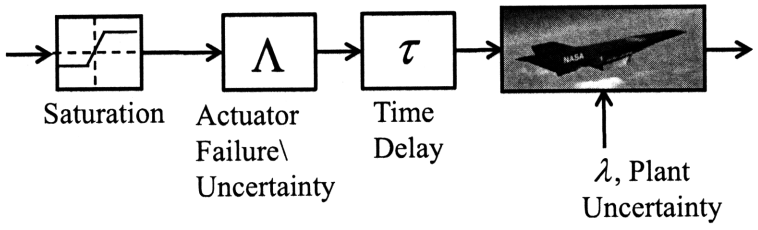

Figure 3-3: Uncertainty modelling

3.4 Adaptive Controller

In order to compensate for the modeling uncertainties, an adaptive controller is now added to the baseline controller described in Section 3.2. We note that the adaptive controller is designed so as to directly accommodate for the parametric uncertainties while remaining robust with respect to the unmodeled uncertainties. The structure of the adaptive controller is chosen as

$$v = \overbrace{K_{ff} r + \underbrace{K^{\mathsf{T}} x}_{\text{nominal}}}^{\text{baseline}} + \underbrace{\theta(t)^{\mathsf{T}} x}_{\text{adaptive}} \tag{3.20}$$

The adaptive component of the controller is denoted, θ, as can be seen in (3.20) and has the same dimension as the nominal feedback gain K. The adaptive component augments naturally with the nominal controller and a visual interpretation of this can be seen in Figure 3-4.

Combining the uncertain plant model in (3.18) with the integral state e_I in (3.5), the input-state in (3.6), the the saturation function in (3.19), and the overall baseline

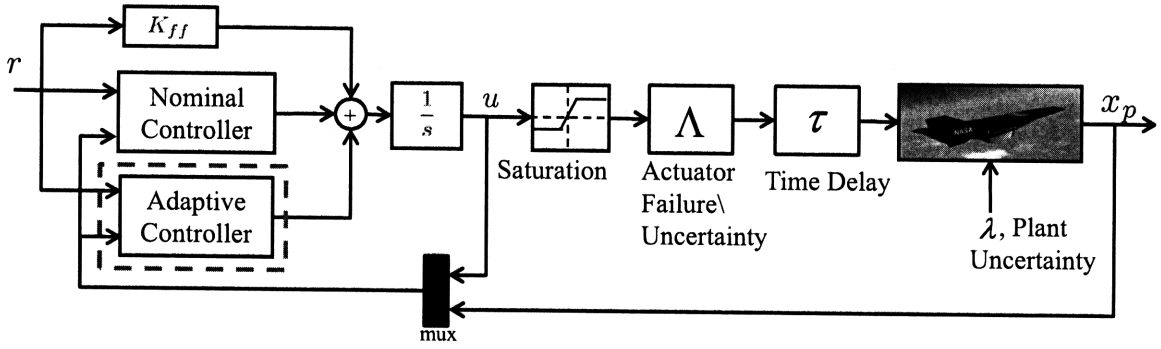

Figure 3-4: Nominal with adaptive augmentation and uncertainty

and adaptive control input from (3.20), the closed loop equations are given by,

$$\underbrace{\begin{bmatrix} \dot{x}_p \\ \dot{e} \\ \dot{u} \end{bmatrix}}_{\dot{x}} = \underbrace{\begin{bmatrix} A_p(\lambda) & 0 & B_p\Lambda \\ H & 0 & 0 \\ K_1+\theta_1(t) & K_2+\theta_2(t) & K_3+\theta_3(t) \end{bmatrix}}_{A(\lambda,\Lambda)+B(K^{\mathsf{T}}+\theta(t)^{\mathsf{T}})} \underbrace{\begin{bmatrix} x_p \\ e \\ u \end{bmatrix}}_{x} + \underbrace{\begin{bmatrix} 0 \\ -I \\ 0 \end{bmatrix}}_{B_{cmd}} K_{ff}r - \underbrace{\begin{bmatrix} B_p \\ 0 \\ 0 \end{bmatrix}}_{B_1} \Lambda u_\Delta, \tag{3.21}$$

where $u_\Delta = u - R_s(u)$, and in compact form reduces to,

$$\dot{x} = (A(\lambda,\Lambda) + B(K^{\mathsf{T}} + \theta(t)^{\mathsf{T}}))x + B_{cmd}K_{ff}r - B_1\Lambda u_\Delta. \tag{3.22}$$

A reference model is chosen as

$$\dot{x}_m = A_m x_m - B_m r. \tag{3.23}$$

where A_m and B_m are such that A_m is a Hurwitz matrix, $B_m = B_{cmd}K_{ff}$ and $\Delta A_m = A(\lambda,\Lambda) + B(K^{\mathsf{T}} + \theta^{*\mathsf{T}}) - A_m$ is arbitrarily small. We note that due to the addition of the integral action, it may not be possible to choose ΔA_m to be zero for general

parametric uncertainties. Defining the state error e as,

$$e = x - x_m, \tag{3.24}$$

we choose adaptive laws for adjusting the adaptive parameter in 3.20 as

$$\begin{aligned} \dot{\theta} &= -\Gamma_\theta x e_u^\mathsf{T} P B \text{sign}(\Lambda) - \sigma_\theta \theta \\ \dot{\hat{\lambda}} &= -\Gamma_\lambda \text{diag}(u_\Delta) B_1^\mathsf{T} P e_u - \sigma_\lambda \hat{\lambda} \end{aligned} \tag{3.25}$$

where $A_m^\mathsf{T} P + P A_m^\mathsf{T} = -Q$ and $Q = Q^\mathsf{T} > 0$. Also $e_u = e - e_\Delta$ where the auxiliary error e_Δ is defined as,

$$\dot{e}_\Delta = A_m e_\Delta - B_1 \text{diag}(\hat{\lambda}) u_\Delta. \tag{3.26}$$

The auxiliary error represents the error that occurs do to saturation, and by subtracting it from e we obtain a new error e_u, which is the uncertainty do to parametric uncertainty and unmodelled dynamics alone. In the above adaptive laws the Γ's are design parameters that control the rate of adaptation, and the other design parameter σ introduces damping into the laws. The choice of Γ was driven by an optimal selection function defined in [17] with more details contained in Appendix C.

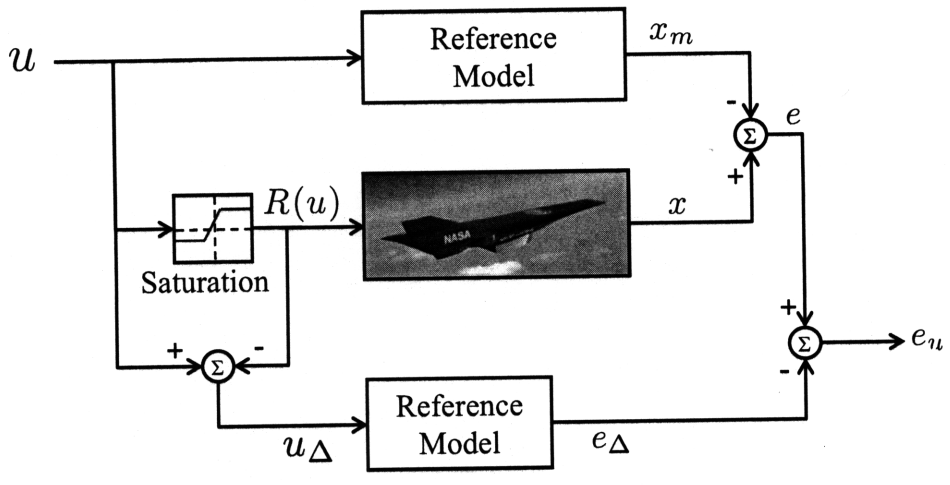

Figure 3-5: Error Modelling

Chapter 4

Simulation Studies

In order to assess the robustness of the adaptive control scheme, several simulation studies were performed. In the simulation studies the adaptive controller is compared to the nominal controller under an uncertain plant flight condition. All of the simulation begin with the HSV Evaluation Model in level flight at an altitude of 85,000 ft and travelling at Mach 8. The trim values for the HSV at this flight condition are given in Table 4.1.

Table 4.1: Trim values for two input HSV model.

State Variable	Trim Value	Units
V	7850	ft/s
α	0.0268	rad
q	0	rad/s
h	85000	ft
θ	0.0268	rad
η_f	0.939	–
$\dot{\eta}_f$	0	–
η_a	0.775	–
$\dot{\eta}_a$	0	–

A similar approach to that shown in Equation (3.3) was performed on the Evaluation Model. Using the state Jacobian and the input Jacobian matrices a pole–zero plot of the transfer matrix from the control inputs ϕ and δ_e to V and γ was generated and is shown in Figure 4-1, with a zoom of the origin shown in Figure 4-2.

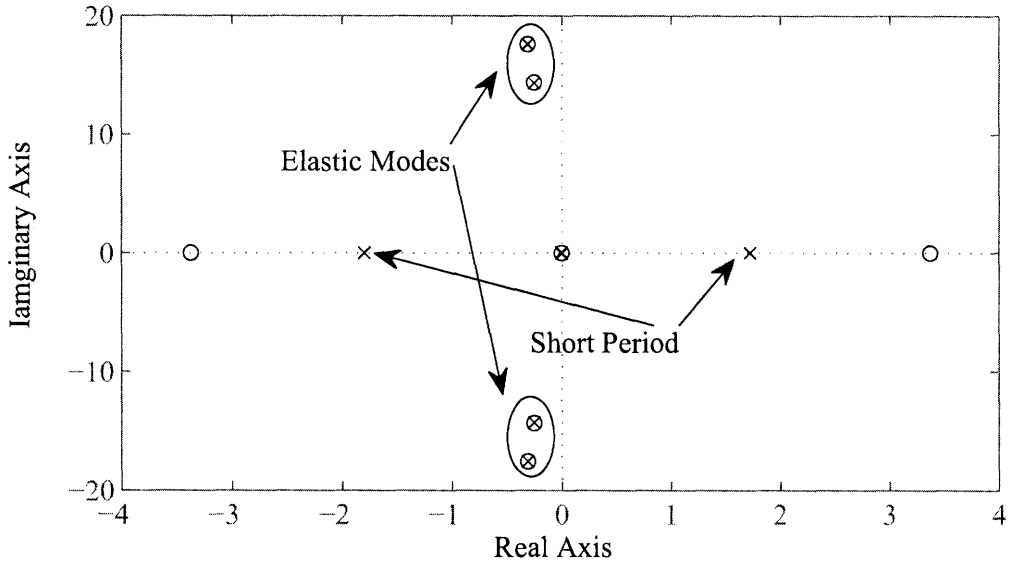

Figure 4-1: Pole Zero Map for $\phi\,\delta_e$ to $V\,\gamma$.

From the figures it is readily noticed that the HSV has an uncharacteristic short period mode, and is therefore open loop unstable. In most aircraft the short period mode is stable. The HSV lacks this stability because of the slender body and rear controls. The *Right Half Plane* (RHP) zero arises from the interaction between the elevator deflection, δ_e, and the heading γ. In order for the aircraft to increase the euler angle the aircraft must first nose down, so as to gain speed, and then nose up. If this counter intuitive procedure is not carried out and the aircraft is simply brought nose up, then the speed of the aircraft will decrease and the aircraft will begin to loose altitude. Zooming in on the origin of the P–Z map the slow Phugoid mode is found along with a slightly unstable altitude mode.

Eight different sets of simulations are carried out in the this chapter. Four different sets of uncertain plant dynamics will be controlled with both a nominal, non–adaptive, controller and then once with an adaptive controller. The uncertain sets are numbered 1–4 with the non adaptive simulations prefixed with "N" and the adaptive simulation results prefixed with "A". So for example, the first uncertain parameter set simulation with a non–adaptive controller is denoted "N1".

The following four uncertain parameter sets are used, (uncertain parameters given

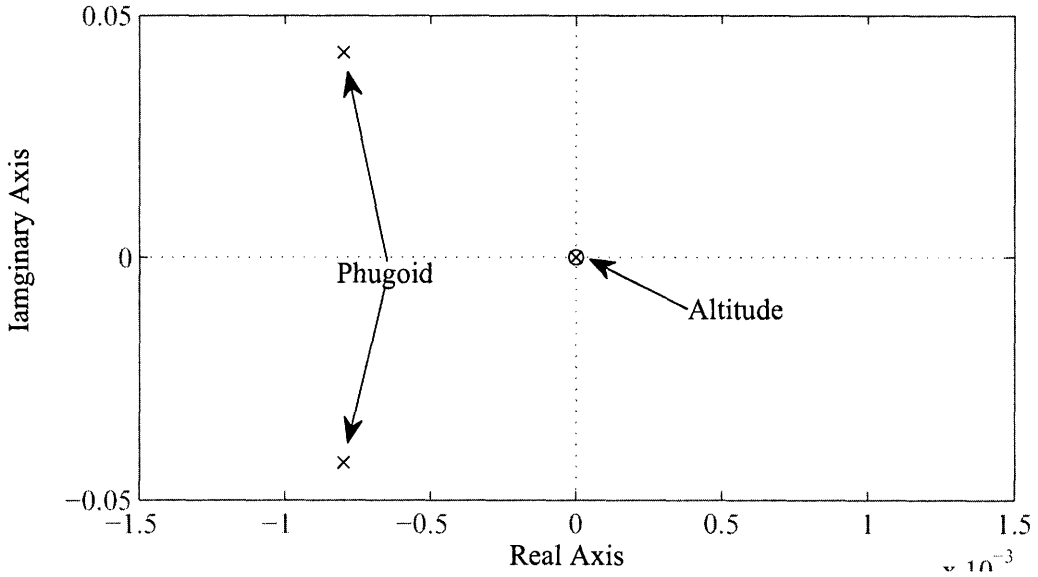

Figure 4-2: Pole Zero Map zoom in at the origin.

in Table 4.2):

1. No uncertainty, nominal plant.

2. Decreased lift and moment coefficients along with the center of gravity moved forward in the HSV. This scenario introduces a more stable aircraft, however decreases the maneuverability of the HSV and will display the control algorithms robustness with respect to saturation.

3. Same as (2) with a significant time delay.

4. Center of gravity moved backwards, leads to more unstable open–loop dynamics as well as increase in the uncertain pitching moment coefficient.

For the simulation studies a filtered step command in altitude of 10,000 ft and a filtered step command of 1,000 ft/s were given. The filter used to generate the smooth commands is that of order two with a damping ratio of 1 and a natural frequency of 0.06 rad. The filtered commands are displayed in Figure 4-3.

The first set of simulations are introduced in order to compare how the adaptive controller compares to the nominal controller when there is no uncertainty. The

Table 4.2: Simulation Study Uncertainty Selection.

Label	τ	λ_L	λ_M	λ_{CG}
N1	0.00	1.0	1.0	0.00
A1	0.00	1.0	1.0	0.00
N2	0.00	0.8	0.8	0.03
A2	0.00	0.8	0.8	0.03
N3	0.06	0.8	0.8	0.03
A3	0.06	0.8	0.8	0.03
N4	0.00	0.4	1.8	-0.16
A4	0.00	0.4	1.8	-0.16

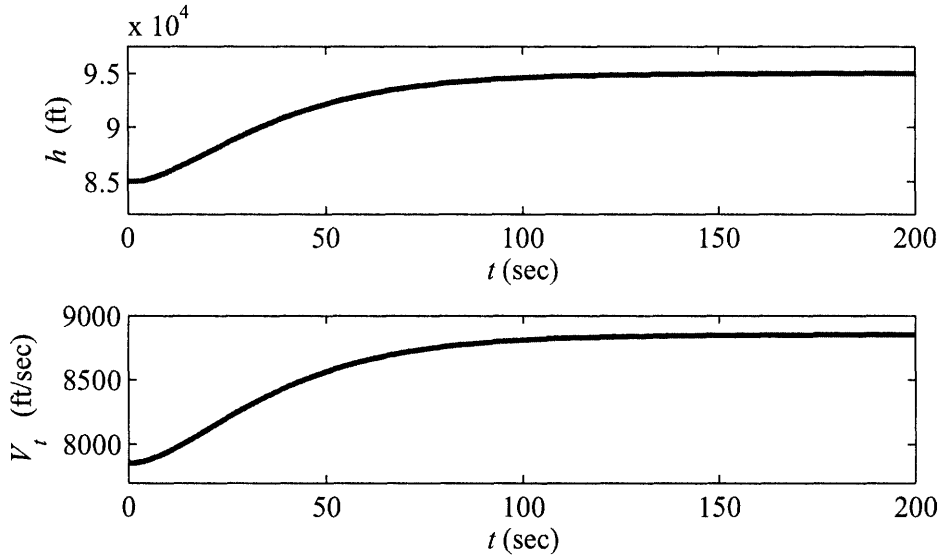

Figure 4-3: Reference command in h–V space.

command following errors for the N1 and A1 simulations are shown in Figure 4-4 and the control input signals are displayed in Figure 4-5. The first thing to notice from the simulation results for no uncertainty is that the adaptive and nominal results are indistinguishable with the naked eye. This is desirable as at nominal conditions the adaptive controller should not contribute to the control scheme. It can also be verified that the adaptive controller is not contributing to the overall control scheme by inspecting the adaptive parameter time history shown in Figure B-10. Another characteristic of the simulation study that is readily noticeable is the highly oscillatory response. The low frequency lightly damped oscillations are a consequence of the elastic poles as seen in the P–Z map, Figure 4-1. Recall that the control scheme

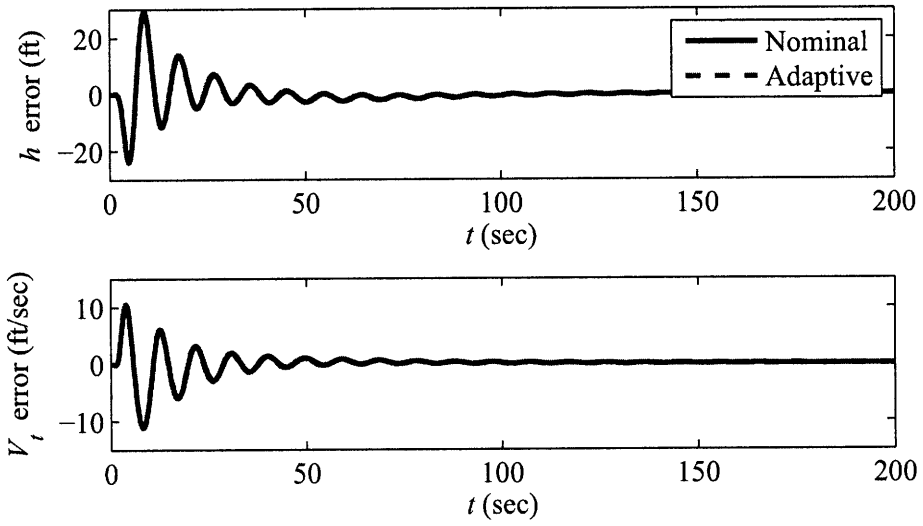

Figure 4-4: Command following errors for N1 and A1 simulation studies.

employed, whether nominal or adaptive, neglects the elastic states and this work relies on the fact that the control structure employed is simply robust with respect to elastic effects. Simulation results for the HSV model with rigid–body dynamics, only, does not display such severe oscillatory behavior.

The second uncertainty scenario introduces uncertainty in the aero coefficients as well as uncertainty in the center of gravity location. As previously mentioned,

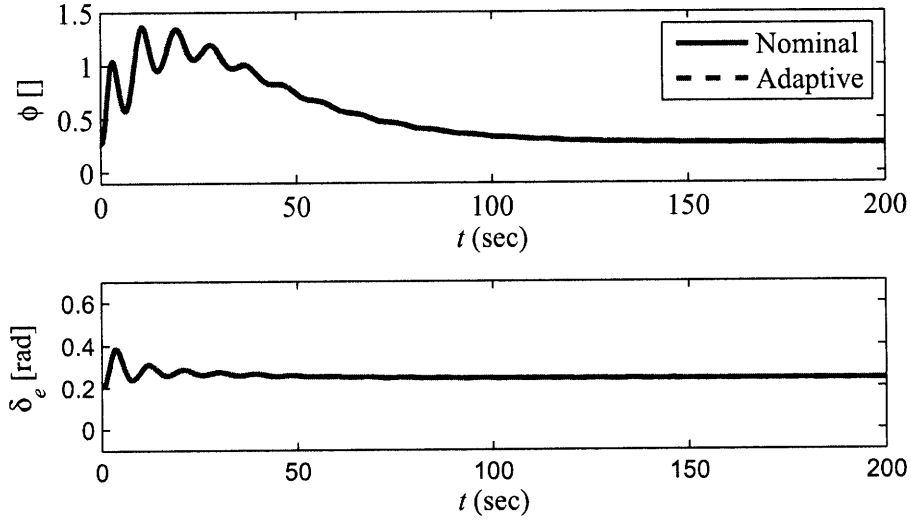

Figure 4-5: Control input for N1 and A1 simulation studies.

this scenario was introduced with the purpose of initiating saturation in the control inputs. The command following error time plots and control inputs for the N2 and A2 studies are shown in Figures 4-5 and 4-6 respectively.

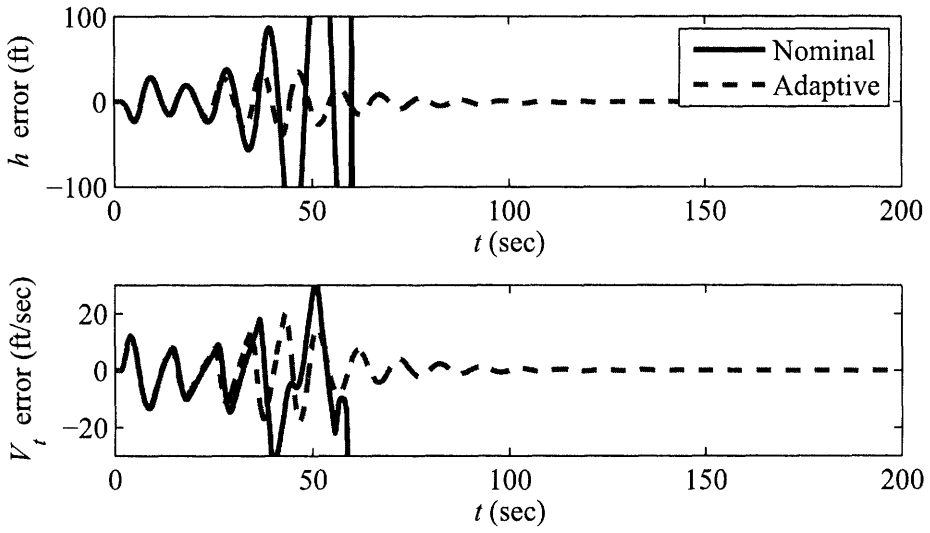

Figure 4-6: Command following errors for N2 and A2 simulation studies.

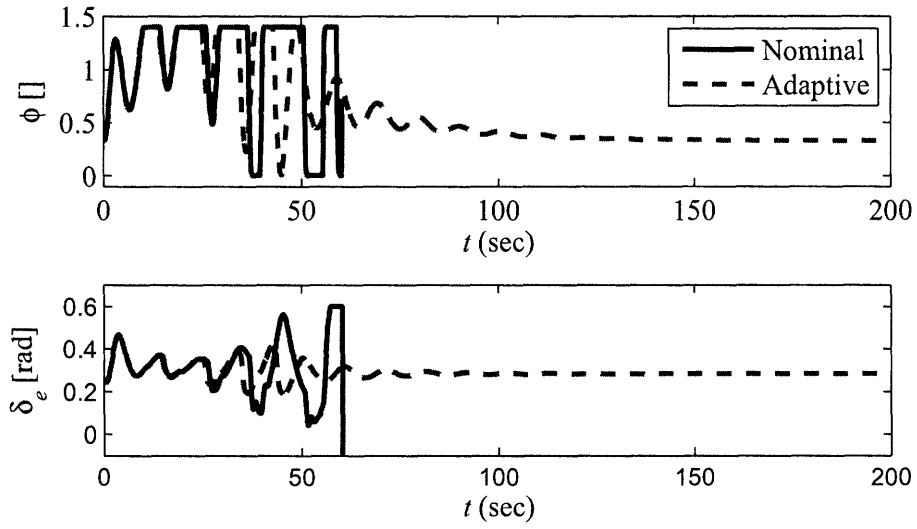

Figure 4-7: Control input for N2 and A2 simulation studies.

The adaptive controller and nominal controller generate similar initial transients. However, as time progresses the adaptive control results limit cycle for shorter and shorter periods of time, while the nominal controller limit cycles until the angle of

attack departs severely and the simulation is stopped. The adaptive parameters, as seen in Figure B-20, adjust in a stable fashion even during saturation because of the use of the augmented error dynamics e_u as shown in Figure (3-5). If the generic reference model error e were used instead of e_u the adaptive controller would not perform as well during saturation.

The uncertain scenarios of A2 was then modified for uncertain scenario 3. The time delay τ was increased from 0 in increments of 0.01s until the adaptive control structure failed. The adaptive algorithm was stable from 0.00s to 0.05s of time delay, until ultimately the adaptive controller failed with a time delay of 0.06s. The command following error and control inputs for N3 and A3 are shown in Figures 4-8 and 4-9. The adaptive controller illustrates better tracking and less saturation than the nominal controller during the first 40 seconds of the simulation. However, the time delay is too large and leads to an unbounded response from the nonlinear controller. 60 milliseconds of uncertain time delay is rather significant however. Time delays within the control hardware of large transport vehicles can be on the order of 40-80 milliseconds. For hypersonic vehicle this value is expected to be much lower.

The last uncertainty scheme introduces and obscure scenario. The uncertain parameters are rather large, in fact, larger than they are in scenario 2. Yet the adaptive

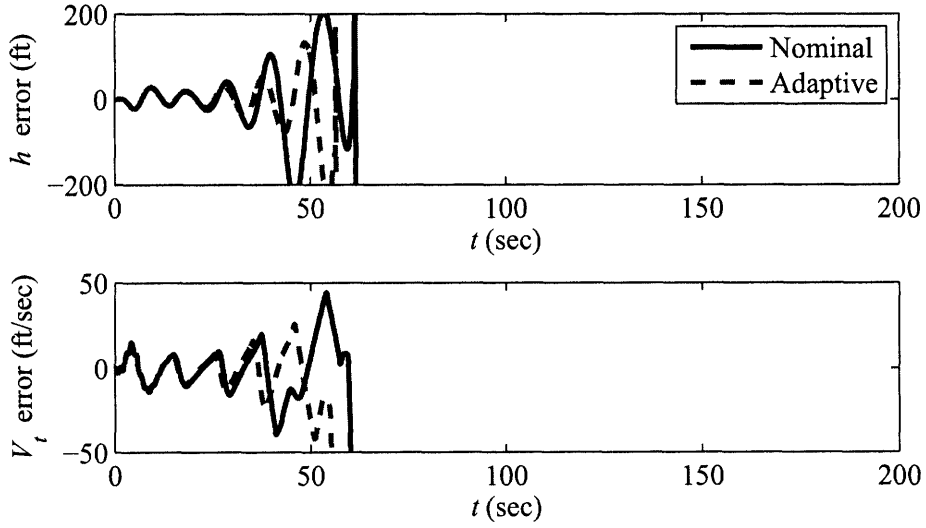

Figure 4-8: Command following errors for N3 and A3 simulation studies.

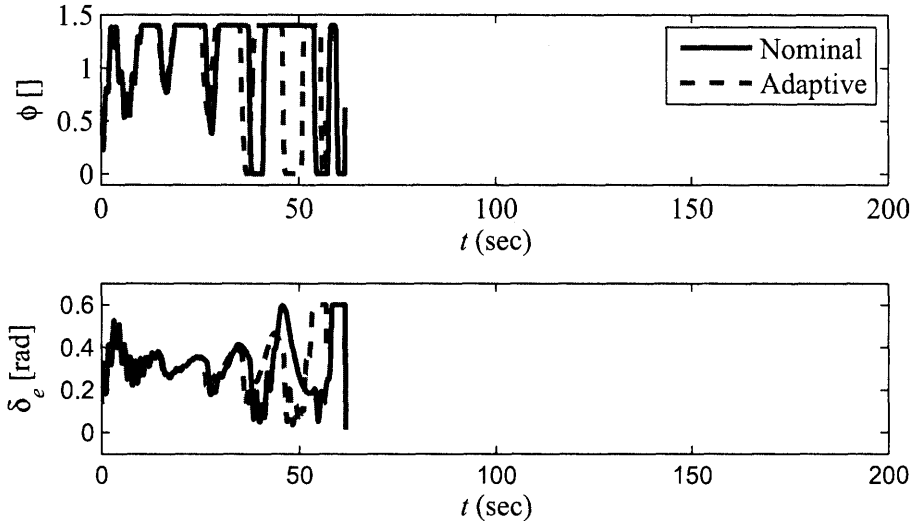

Figure 4-9: Control input for N3 and A3 simulation studies.

controller and nominal controller results are indistinguishable. The command following error and control inputs for N3 and A3 are shown in Figures 4-10 and 4-11.

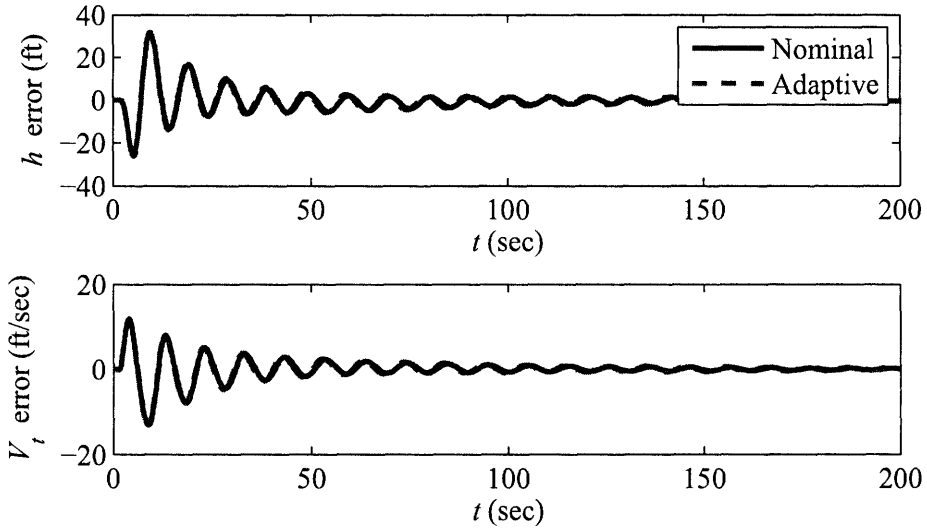

Figure 4-10: Command following errors for N4 and A4 simulation studies.

The reference model error was not large enough to instigate changes in the adaptive parameter, see Figure B-40. This illustrates the fact that the uncertain parameter space does not map intuitively to the failure domains for the adaptive or non adaptive algorithms. Therefore, it is difficult to assess the overall performance of the adaptive

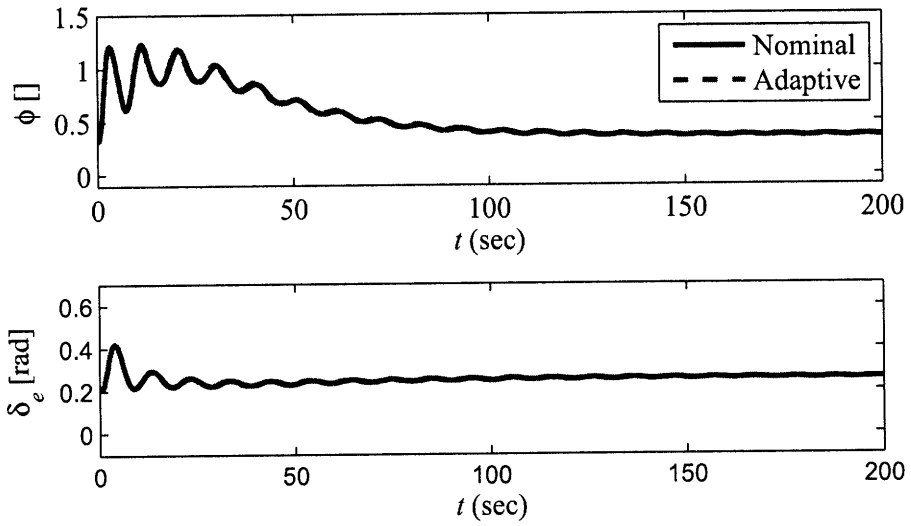

Figure 4-11: Control input for N4 and A4 simulation studies.

algorithm. This leads to Chapter 5, where a more rigorous approach for controller validation is performed.

Chapter 5

Control Verification, A different Approach

In order to have a better assessment of the improvement in performance with the adaptive controller, we use tools that have been developed in [16] and [15] . In order to make the exposition self contained, the tools developed in [16] and [15] are briefly explained below.

5.1 Mathematical Framework

The parameters which specify the closed-loop system are grouped into two categories: uncertain parameters which are denoted by the vector p, and the control design parameters which are denoted by the vector d. While the plant model depends on p, the controller depends on d. The *Nominal Parameter* value, denoted as $\bar{p}$, is a deterministic estimate of the true value of p. Stability and performance requirements for the closed-loop system will be prescribed by the set of inequality constraints $g(p, d) < 0$. For a fixed d, the larger the region in p-space where $g < 0$ the more robust the controller. The *Failure Domain* corresponding to the controller with parameter d

is given by[1]

$$\mathcal{F}^j(d) = \{p : g_j(p, d) \geq 0\}, \tag{5.1}$$

$$\mathcal{F}(d) = \bigcup_{j=1}^{\dim(\boldsymbol{g})} \mathcal{F}^j(d). \tag{5.2}$$

While Equation (5.1) describes the failure domain corresponding to the jth requirement, Equation (5.2) describes the failure domain for all requirements. The *Non-Failure Domain* is the complement set of the failure domain and will be denoted[2] as $\mathcal{F}^c$. The names "failure domain" and "non-failure domain" are used because in the failure domain at least one constraint is violated while, in the non-failure domain, all constraints are satisfied.

Let a reference set where the parameter $\bar{p}$ lies be given by the hyper-rectangle,

$$\mathcal{R}(\bar{p}, n) = \{p : \bar{p} - n \leq \ p \leq \bar{p} + n\}. \tag{5.3}$$

where $n > 0$ is the vector of half-lengths. One of the tasks of interest is to assign a measure of robustness to a controller based on measuring how much the reference set can be deformed before intersecting the failure domain.

In what follows we assume that $g(\bar{p}, d) < 0$. We define a Critical Parameter Value, CPV, as the point where the deforming set touches the failure domain. The CPV corresponding to the deformation of $\mathcal{R}(\bar{p}, n)$ for the jth requirement is given by

$$\tilde{p}^j = \underset{\boldsymbol{p}}{\operatorname{argmin}} \left\{ \|p - \bar{p}\|_{\boldsymbol{n}}^{\infty} : g_j(p, d) \geq 0, \ Ap \geq b \right\}, \tag{5.4}$$

where $\|x\|_{\boldsymbol{n}}^{\infty} = \sup_i\{|x_i|/n_i\}$ is the n-scaled infinity norm. The last constraint is used to exclude regions of the parameter space where plants are infeasible and/or uncertainty levels are unrealistic. The overall CPV is

$$\tilde{p} = \tilde{p}^k, \tag{5.5}$$

[1]Throughout this paper, super-indices are used to denote a particular vector or set while numerical sub-indices refer to vector components, e.g., p_i^j is the ith component of the vector p^j.

[2]The complement set operator will be denoted as the super-index c.

where

$$k = \underset{1 \leq j \leq \dim(\boldsymbol{g})}{\operatorname{argmin}} \left\{ \|\tilde{p}^j - \bar{p}\|_{\boldsymbol{n}}^{\infty} \right\}. \tag{5.6}$$

Hence, once the CPV for each individual constraint function is solved for, the overall CPV is the closest of these CPVs to the nominal parameter point according to the n-scaled infinity norm.

The size of the deformed set is proportional to *Rectangular PSM*, which is defined as

$$\rho = \tilde{\alpha}\|n\|, \tag{5.7}$$

where $\tilde{\alpha} = \|\tilde{p} - \bar{p}\|_{\boldsymbol{n}}^{\infty}$, referred to as the critical similitude ratio, is non-dimensional, but depends on both the shape and the size of the reference set.[14] The PSM has the same units as the uncertain parameters, and depends on the shape, but not the size, of the reference set. If the PSM is zero, the controller's robustness is practically nil since there are infinitely small perturbations of $\bar{p}$ leading to the violation of at least one of the requirements. If the PSM is positive, the requirements are satisfied for parameter points in the vicinity of the the nominal parameter point. The larger the PSM, the larger the hyper-rectangular vicinity.

5.2 Hypersonic Vehicle Uncertainty

The following uncertain parameters will be considered in subsequent analysis

1. Multiplicative uncertainty in the inertial properties: $\lambda_m \in (0, 2]$.
2. Multiplicative uncertainty in lift: $\lambda_L \in (0, 2]$.
3. Multiplicative uncertainty in pitching moment: $\lambda_M \in (0, 2]$.
4. Time delay τ in both plant inputs, where $\tau \in (0, 0.04]$.
5. Longitudinal distance between the neutral point and the center of gravity $\lambda_{CG} \in [-0.1, 0.1]$.

The reference set Ω for $p = [\lambda_m, \lambda_L, \lambda_M, \tau, \lambda_{CG}]$ to be used is a hyper-rectangle with aspect vector $n = [1, 1, 1, 0.04, 0.1]$ and nominal parameter point $\bar{p} = [1, 1, 1, 0, 0]$. Note that n determines the relative levels of uncertainty among parameters, e.g., there is 0.04/0.1 more uncertainty in the CG location than in the time delay.

A set of closed-loop requirements is introduced subsequently. Lets define the vector of signals

$$h(p, d, t) = [\dot{V}(p, d, t) - 10g, |\alpha(p, d, t)| - 0.2, \tag{5.8}$$

$$\|e_{I,1}(p, d, t)\|_2 - q\|e_{I,1}(\bar{p}, d_{base}, t_f)\|_2, \tag{5.9}$$

$$\|e_{I,2}(p, d, t)\|_2 - q\|e_{I,2}(\bar{p}, d_{base}, t_f)\|_2], \tag{5.10}$$

where $e_{I,1}$ is the velocity error, $e_{I,2}$ is the altitude error, q is a real number larger than one, d_{base} refers to the baseline controller, and t_f is a sufficiently large integration time. This vector enables the formulation of the following set of requirements:

1. Structural: the load factor must not exceed 10, i.e., $g_1 = \max_t\{h_1\}$.

2. Stability and engine stall: the angle of attack must stay in the ± 0.2 *rad* range, i.e., $g_2 = max_t\{h_2\}$.

3. Tracking performance in velocity: the tracking error must not exceed a prescribed upper bound, i.e., $g_3 = h_3(t = t_f)$.

4. Tracking performance in altitude: the tracking error must not exceed a prescribed upper bound, i.e., $g_4 = h_4(t = t_f)$.

In the studies that follow we will evaluate the robustness characteristics of both controllers for several subsets of $[\lambda_m, \lambda_L, \lambda_M, \tau, \lambda_{CG}]$. Parametric studies indicate that the trim-ability condition $\max\{u_{max} - U_0, U_0 - u_{min}\}$, where $f(X_0, U_0, p) = 0$ for the saturation limits u_{max} and u_{min}, is satisfied for all the values of p in the range of interest.

5.3 Baseline Controller Analysis

Table 5.1 provides the CPVs corresponding to each individual uncertain parameter for the baseline controller. The critical requirement corresponding to λ_m, λ_L, λ_M, τ, and λ_{CG}, are g_4, g_2, g_1, g_1, and g_4 respectively. Note that λ_{CG} is the critical parameter and g_4 its most critical requirement. The PSM and the CPV corresponding to $p = [\tau, \lambda_{CG}]$ are equal to $\rho = 0.02564$ and $\tilde{p} = [0.0095, -0.02381]$. As with the 1-dimensional case, the critical requirement is g_1. In the case where $p = [\lambda_m, \lambda_L, \lambda_M, \tau, \lambda_{CG}]$, the PSM, the CPV and the critical requirement are $\rho = 0.150$, $\tilde{p} = [1.086, 0.913, 0.962, 8.4 \times 10^{-11}, -0.0086]$ and g_4.

Table 5.1: 1-dimensional CPVs for d_{base}.

	$\tilde{p}^1$	$\tilde{p}^2$	$\tilde{p}^3$	$\tilde{p}^4$
$p = [\lambda_m]$	1.1847	1.1847	1.1845	1.1843
$p = [\lambda_L]$	0.5187	0.5184	0.6540	0.7036
$p = [\lambda_M]$	0.3670	0.3670	0.3897	0.4015
$p = [\tau]$	0.0310	$\emptyset$	0.0362	0.0362
$p = [\lambda_{CG}]$	−0.0246	−0.0246	−0.0242	−0.0240

5.4 Adaptive Controller Analysis

Table 5.2 shows the 1-dimensional CPVs associated with the adaptive controller. The critical requirements corresponding to λ_m, λ_L, λ_M, τ, and λ_{CG}, are now g_1, g_4, g_4, g_1, and g_4. This set of critical requirements differs from that of the baseline. As before, the critical parameter is λ_{CG} and its most critical requirement g_4. The PSM and the CPV corresponding to $p = [\tau, \lambda_{CG}]$ are equal to $\rho = 0.02845$ and $\tilde{p} = [0.0090, -0.0264]$. As with the 1-dimensional case, the critical requirement is g_4. In the case where $p = [\lambda_m, \lambda_L, \lambda_M, \tau, \lambda_{CG}]$, the PSM, the CPV and the critical requirement are $\rho = 0.145$, $\tilde{p} = [1.083, 0.916, 0.963, 8.1 \times 10^{-11}, -0.009]$ and g_4.

Table 5.2: 1-dimensional CPVs for $d_{adaptive}$.

	$\tilde{p}^1$	$\tilde{p}^2$	$\tilde{p}^3$	$\tilde{p}^4$
$p = [\lambda_m]$	0.7674	1.2347	0.7643	0.7610
$p = [\lambda_L]$	0.4606	0.4606	0.6005	0.6866
$p = [\lambda_M]$	0.2271	0.2271	0.2865	0.3629
$p = [\tau]$	0.0300	0.0316	0.0312	0.0312
$p = [\lambda_{CG}]$	−0.0293	−0.0293	−0.0286	−0.0267

5.5 Comparative Analysis

The improvements in robustness resulting from augmenting the baseline controller are shown in Table 5.3. The data in Tables 5.1 and 5.2 fully determine Table 5.3. The adaptive controller attains better margins in the λ_m, λ_L, λ_M, and λ_{CG} directions. While the λ_m direction leads to the largest improvement, τ produces the only drop. This situation illustrates the tight dependence that exists between any robust control assessment method and the uncertainty model assumed. Note that the critical parameters and the critical requirements corresponding to d_{base} coincide with those of $d_{adaptive}$. Overall the augmented control architecture attains sizable improvements in all but one of the cases. Since multi-dimensional cases are more realistic, the adoption of the adaptive controller is well justified.

Table 5.3: Relative PSM improvement.

	$\left(\frac{\rho_{adaptive}}{\rho_{baseline}} - 1\right) 100\%$
$p = [\lambda_m]$	26.2%
$p = [\lambda_L]$	5.7%
$p = [\lambda_M]$	6.5%
$p = [\tau]$	−3.2%
$p = [\lambda_{CG}]$	11.2%
$p = [\tau, \lambda_{CG}]$	7.7%
$p = [\lambda_m, \lambda_L, \lambda_M, \tau, \lambda_{CG}]$	8.2%

The parameter space $p = [\tau, l]$ for the adaptive controller is shown in Figure 5-1. The non-failure domain, which contains the nominal parameter point, is colored in

green while the failure domain is in red. The boundaries of individual failure domains, are also shown. A dotted white line denotes $g_1 = 0$, a solid black line $g_2 = 0$, a short-dashed yellow line $g_3 = 0$, and a long-dashed blue line $g_4 = 0$. Note that $\mathcal{F}^c(d_{base})$ is delimited by the boundaries of $\mathcal{F}^1$ and $\mathcal{F}^4$ only. A comparison between $\mathcal{F}^c(d_{base})$ (not shown) and $\mathcal{F}^c(d_{adaptive})$ indicates improved robustness to CG uncertainty, and smaller robustness to time delay. Note the high sensitivity of the time delay margin to the CG location. In both controllers, such a margin increases as the CG moves forward from the its nominal position. Large movements however, reverse this trend. Both controllers exhibit a sudden drop in time-delay margin close to $\lambda_{CG} = -0.025$. Such a drop is caused by the violation of the tracking performance requirement.

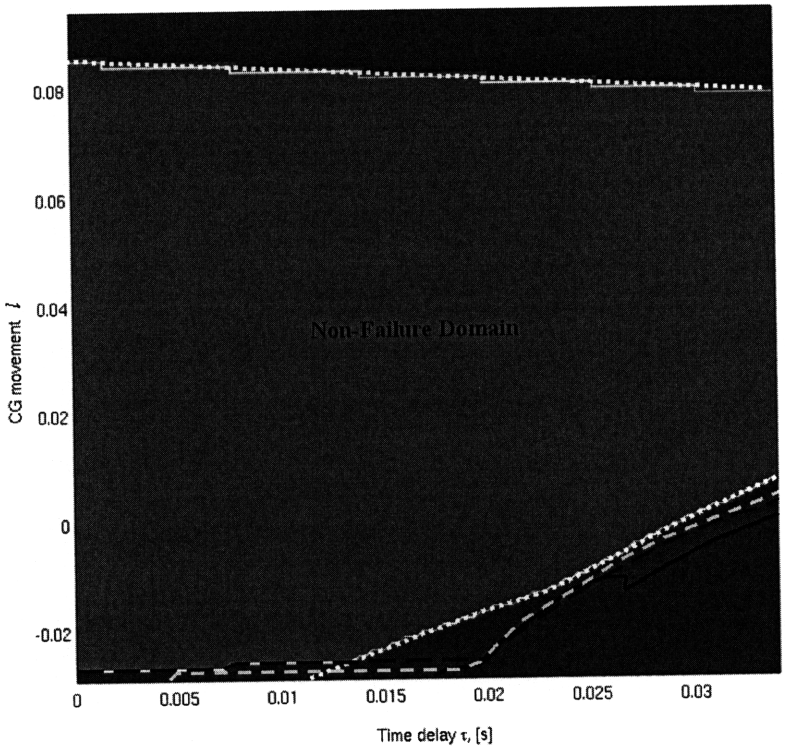

Figure 5-1: Failure and non-failure domains for the adaptive controller.

Chapter 6

Conclusions

An adaptive controller was proposed for a hypersonic vehicle at cruise conditions. The HSV was subject to aerodynamic uncertainties, center–of–gravity movements, actuator saturation and failures, and time-delays. The adaptive algorithm was designed so as to account for modelled uncertainties and remain robust with respect to time delays and elastic effects. The control design was then evaluated using a highfidelity HSV model that considers structural flexibility and thrust-pitch coupling. Time simulations showed the relative improvements in stability gained with the addition of the adaptive algorithm. The level of improvement over the entire uncertainty set was not clear, however. This lead to an elaborate analysis scheme using a stand-alone control verification methodology. The analysis indicated sizable improvements in robust performance resulting from adding an adaptive component to the baseline controller. With the exception of the time-delay margin, where a slight drop in robustness takes place, the region of safe performance was enlarged in all other one–dimensional and multi–dimensional directions of the uncertain space considered. This is particularly remarkable since the parameters and architecture of the adaptive controller were not tailored according to the closed-loop requirements.

Appendix A

Tables

Table A.1: Geometry of Aircraft.

Variable	Value	Units	Variable	Value	Units
l	100	ft	x_c	15	ft
l_f	47	ft	z_c	0	ft
l_u	20	ft	x_e	85	ft
l_a	33	ft	z_e	3.5	ft
h_i	3.5	ft	S_e	17	$\text{ft}^2 \cdot \text{ft}^{-1}$
A_e	5	$\text{ft}^2 \cdot \text{ft}^{-1}$	$\bar{x}$	55	ft
A_d	2	-	$\bar{z}$	0	ft
A_n	6.35	-	m	100	$\text{slugs} \times \text{ft}^{-1}$
$\tau_{1,u}$	3	deg	$\hat{m}_f$	47	$\text{slugs/ft} \times \text{ft}^{-1}$
$\tau_{1,l}$	6.2	deg	$\hat{m}_a$	20	$\text{slugs/ft} \times \text{ft}^{-1}$
τ_2	14.41	deg			

Table A.2: Physical Constants and Aerodynamic Coefficients. [40, 20]

Variable	Value	Units
EI	4.6635×10^{8}	$\text{lb}_\text{f}\cdot\text{ft}^2 \times \text{ft}^{-1}$
I_{yy}	8.6722×10^{4}	slugs $\cdot\text{ft}^2/\text{rad}$
$z_{\mathcal{T}}$	8.3600×10^{0}	ft
S_c	1.7000×10^{1}	$\text{ft}^2 \times \text{ft}^{-1}$
S_e	1.7000×10^{1}	$\text{ft}^2 \times \text{ft}^{-1}$
$\bar{c}$	3.5000×10^{1}	ft
C_L^{α}	4.6773×10^{0}	rad^{-1}
$C_L^{\delta_e}$	7.6224×10^{-1}	rad^{-1}
$C_L^{\delta_c}$	9.2176×10^{-1}	rad^{-1}
C_L^{0}	-1.8714×10^{-2}	-
C_D^{α}	-4.5315×10^{-2}	rad^{-1}
$C_D^{\alpha^2}$	5.8224×10^{0}	rad^{-2}
$C_D^{\delta_e}$	2.7699×10^{-4}	rad^{-1}
$C_D^{\delta_e^2}$	8.1993×10^{-1}	rad^{-2}
$C_D^{\delta_c}$	-2.2416×10^{-16}	rad^{-1}
$C_D^{\delta_c^2}$	1.1859×10^{0}	rad^{-2}
C_D^{0}	1.0131×10^{-2}	-
C_M^{α}	2.1335×10^{0}	rad^{-1}
$C_M^{\alpha^2}$	6.2926×10^{0}	rad^{-2}
$C_M^{\delta_e}$	-1.2987×10^{0}	rad^{-1}
$C_M^{\delta_c}$	2.7326×10^{0}	rad^{-1}
C_M^{0}	1.8979×10^{-1}	-
$C_{N_f}^{\alpha^2}$	1.4013×10^{3}	$\text{lb}\cdot\text{slug}^{-0.5}\cdot\text{rad}^{-2} \times \text{ft}^{-1}$
$C_{N_f}^{\alpha}$	4.5737×10^{3}	$\text{lb}\cdot\text{slug}^{-0.5}\cdot\text{rad}^{-1} \times \text{ft}^{-1}$
$C_{N_f}^{\delta_c}$	5.0000×10^{2}	$\text{lb}\cdot\text{slug}^{-0.5}\cdot\text{rad}^{-1} \times \text{ft}^{-1}$
$C_{N_f}^{0}$	1.1752×10^{2}	$\text{lb}\cdot\text{slug}^{-0.5} \times \text{ft}^{-1}$
$C_{N_a}^{\alpha^2}$	-5.0227×10^{3}	$\text{lb}\cdot\text{slug}^{-0.5}\cdot\text{rad}^{-2} \times \text{ft}^{-1}$
$C_{N_a}^{\alpha}$	2.8633×10^{3}	$\text{lb}\cdot\text{slug}^{-0.5}\cdot\text{rad}^{-1} \times \text{ft}^{-1}$
$C_{N_a}^{\delta_e}$	1.2465×10^{3}	$\text{lb}\cdot\text{slug}^{-0.5}\cdot\text{rad}^{-1} \times \text{ft}^{-1}$
$C_{N_a}^{0}$	-4.4201×10^{1}	$\text{lb}\cdot\text{slug}^{-0.5} \times \text{ft}^{-1}$
β_1	-3.7693×10^{5}	$\text{lb}\cdot\text{rad}^{-3} \times \text{ft}^{-1}$
β_2	-3.7225×10^{4}	$\text{lb}\cdot\text{rad}^{-3} \times \text{ft}^{-1}$
β_3	2.6814×10^{4}	$\text{lb}\cdot\text{rad}^{-2} \times \text{ft}^{-1}$
β_4	-1.7277×10^{4}	$\text{lb}\cdot\text{rad}^{-2} \times \text{ft}^{-1}$
β_5	3.5542×10^{4}	$\text{lb}\cdot\text{rad}^{-1} \times \text{ft}^{-1}$
β_6	-2.4216×10^{3}	$\text{lb}\cdot\text{rad}^{-1} \times \text{ft}^{-1}$
β_7	6.3785×10^{3}	$\text{lb}\times\text{ft}^{-1}$
β_8	-1.0090×10^{2}	$\text{lb}\times\text{ft}^{-1}$

Table A.3: Trim values for two input HSV model.

State Variable	Trim Value	Units
V	7850	ft/s
α	0.0268	rad
q	0	rad/s
h	85000	ft
θ	0.0268	rad
η_f	0.939	–
$\dot{\eta}_f$	0	–
η_a	0.775	–
$\dot{\eta}_a$	0	–

Table A.4: Eigenvalues and Modes of HSV.

Eigenvalue	Mode
$-0.310 \pm 17.6i$	Forward Aero–elastic
$-0.253 \pm 14.3i$	Aft Aero–elastic
$+1.73, -1.80$	Short Period
$-8 \times 10^{-4} \pm 0.0423i$	Phugoid
8.2×10^{14}	Altitude

Appendix B

Figures

Table B.1: Simulation Study Uncertainty Selection.

Label	τ	λ_L	λ_M	λ_{CG}
N1 – Appendix B.1	0.00	1.0	1.0	0.00
A1 – Appendix B.2	0.00	1.0	1.0	0.00
N2 – Appendix B.3	0.00	0.8	0.8	0.03
A2 – Appendix B.4	0.00	0.8	0.8	0.03
N3 – Appendix B.5	0.06	0.8	0.8	0.03
A3 – Appendix B.6	0.06	0.8	0.8	0.03
N4 – Appendix B.7	0.00	0.4	1.8	-0.16
A4 – Appendix B.8	0.00	0.4	1.8	-0.16

B.1 Simulation Study–N1

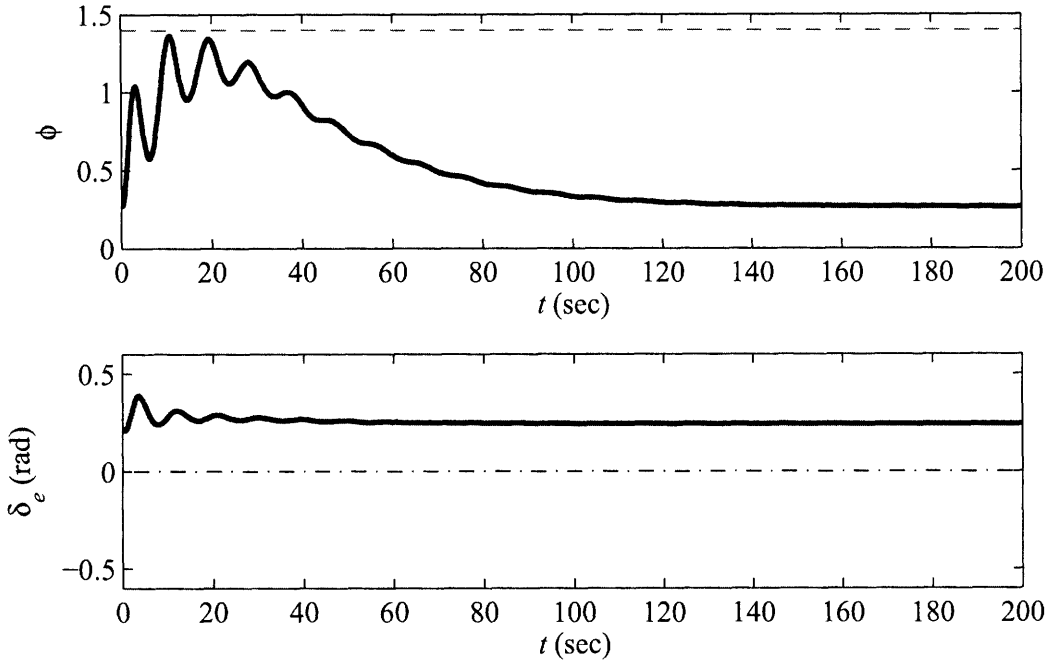

Figure B-1: N1 Control inputs.

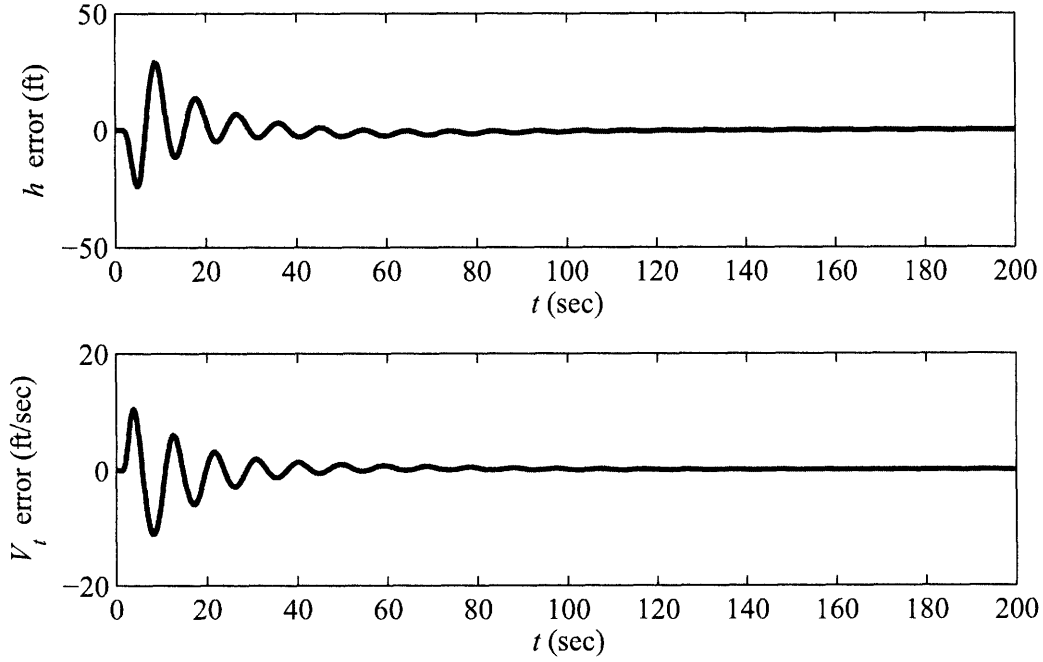

Figure B-2: N1 Command following error.

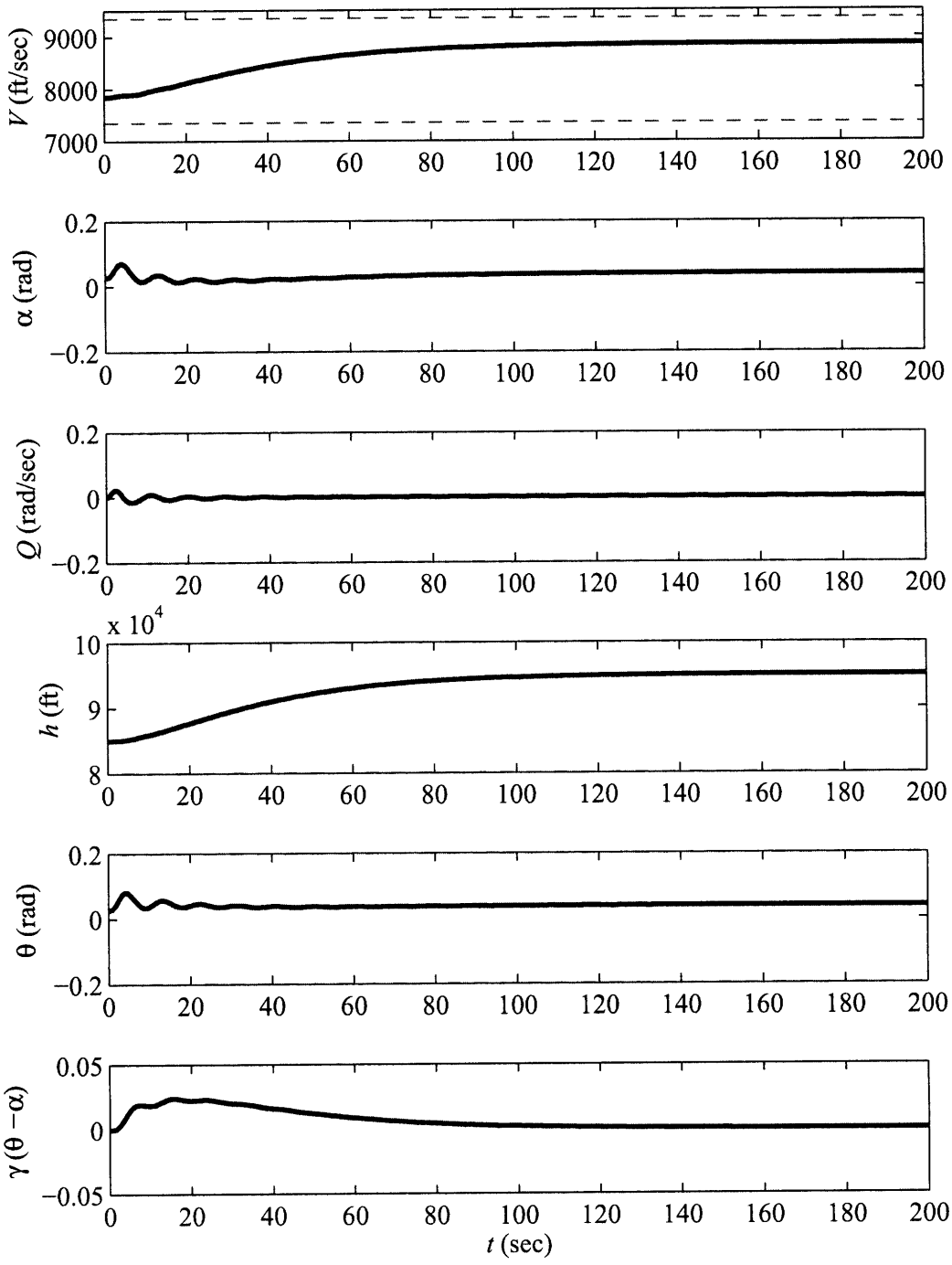

Figure B-3: N1 Rigid states.

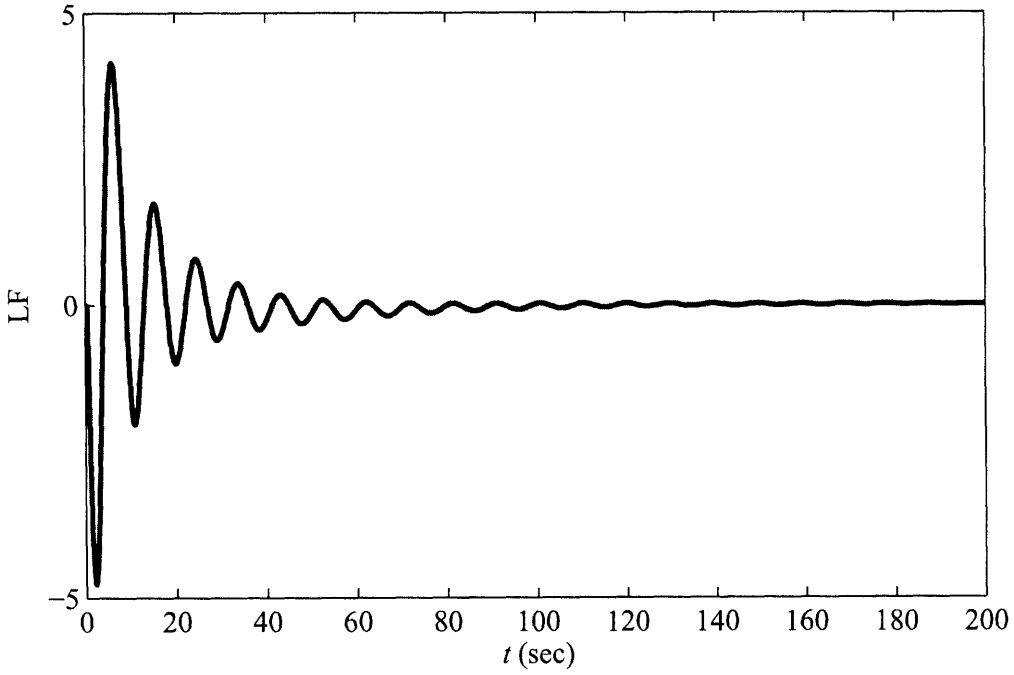

Figure B-4: N1 Loading Factor.

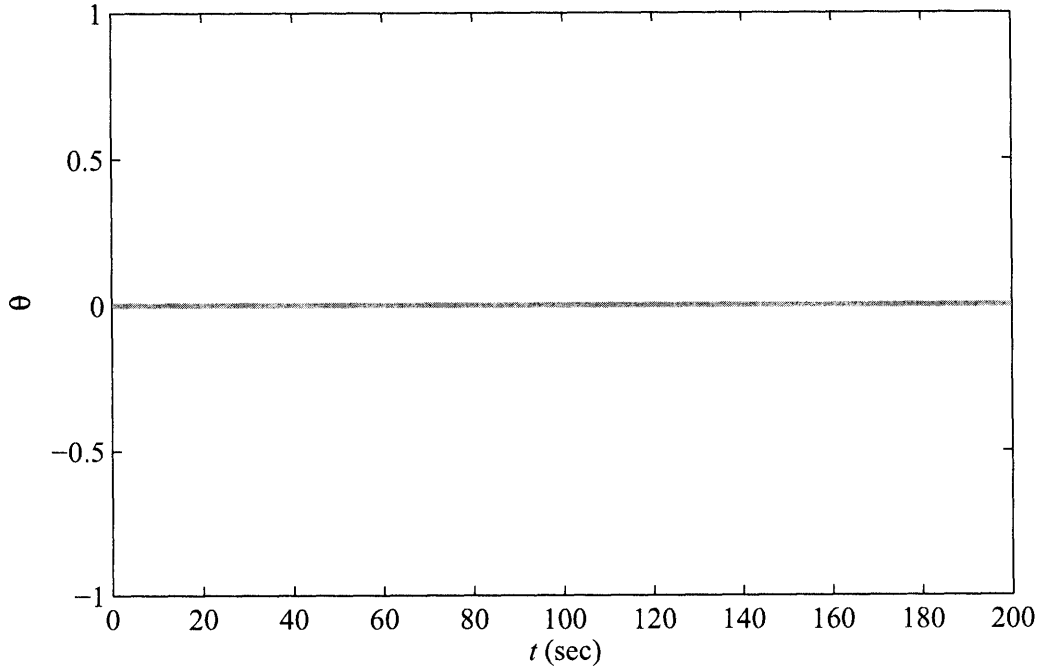

Figure B-5: N1 Adaptive parameters.

B.2 Simulation Study–A1

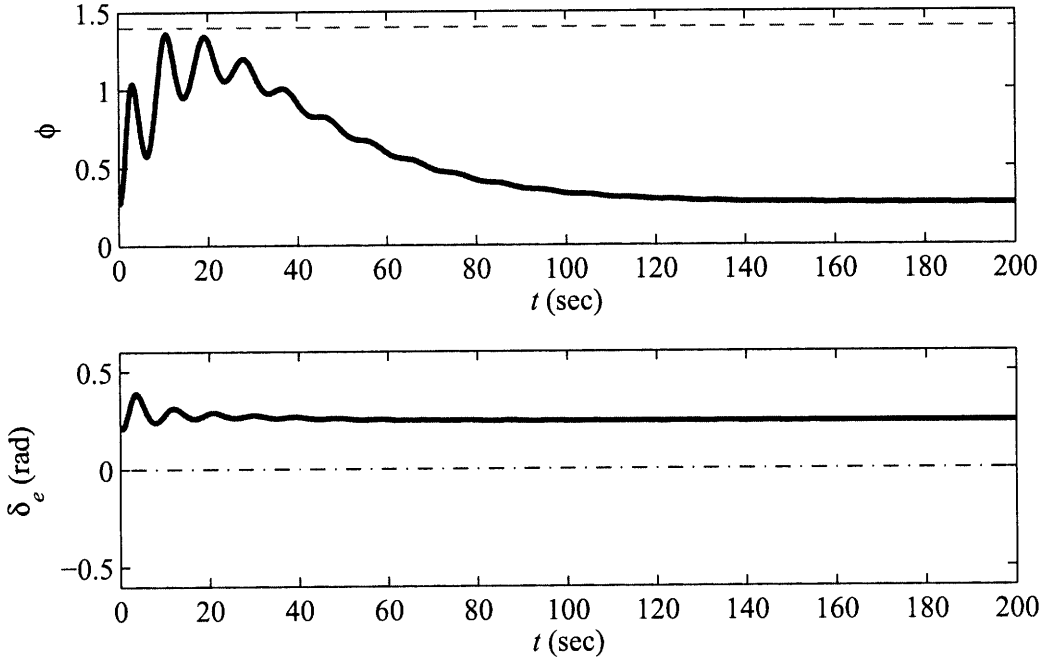

Figure B-6: A1 Control inputs.

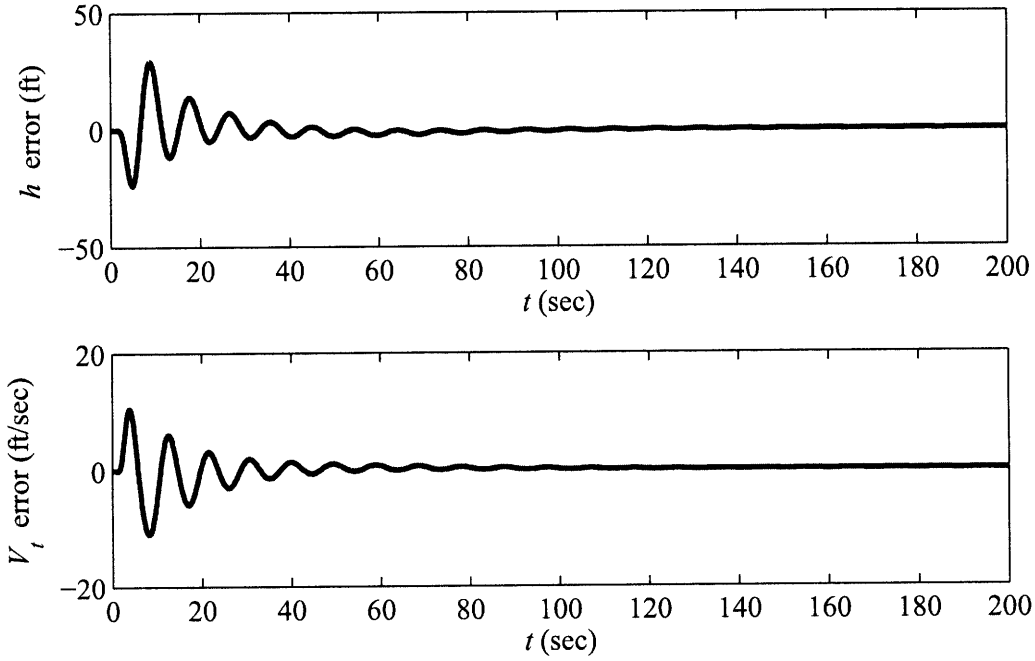

Figure B-7: A1 Command following error.

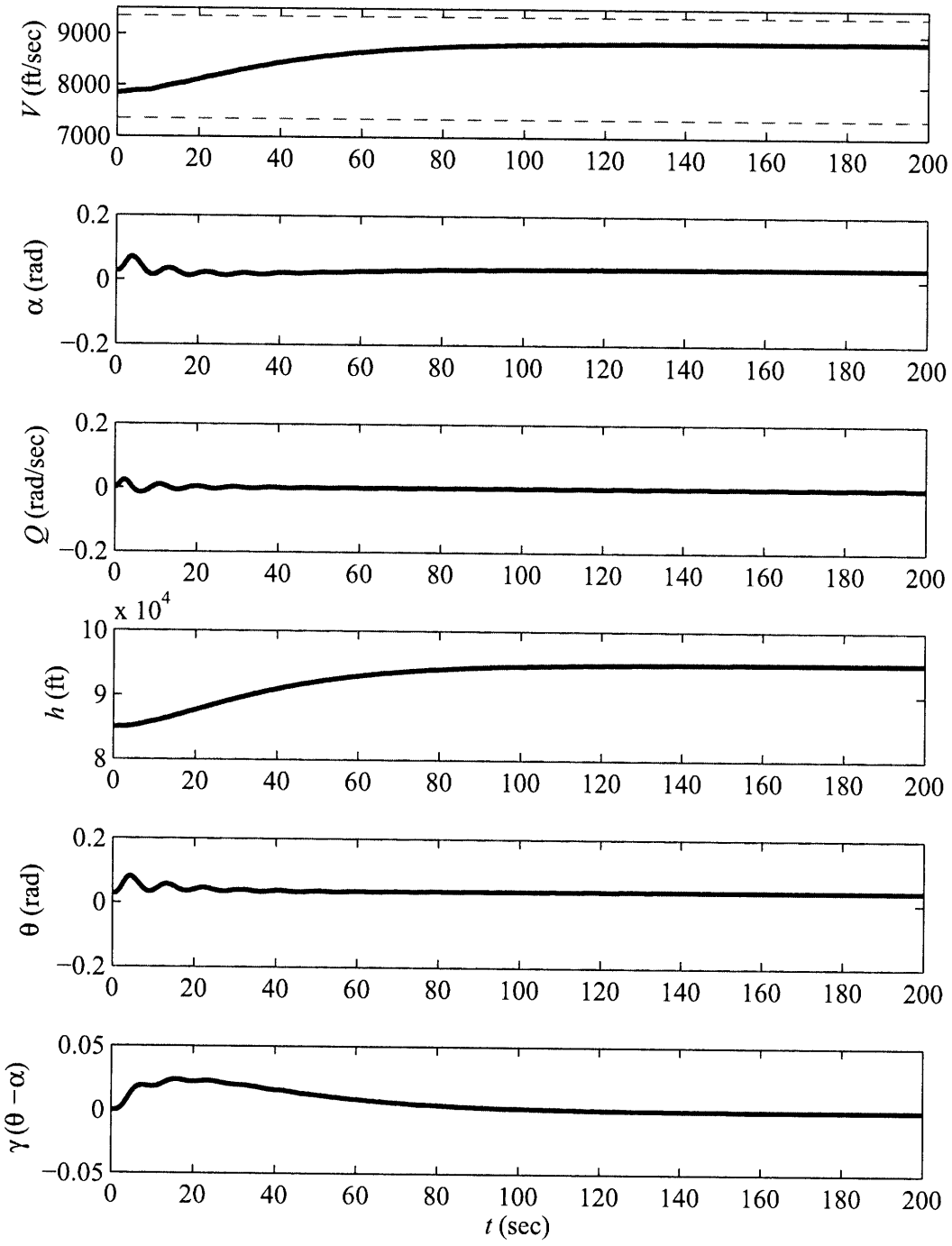

Figure B-8: A1 Rigid states.

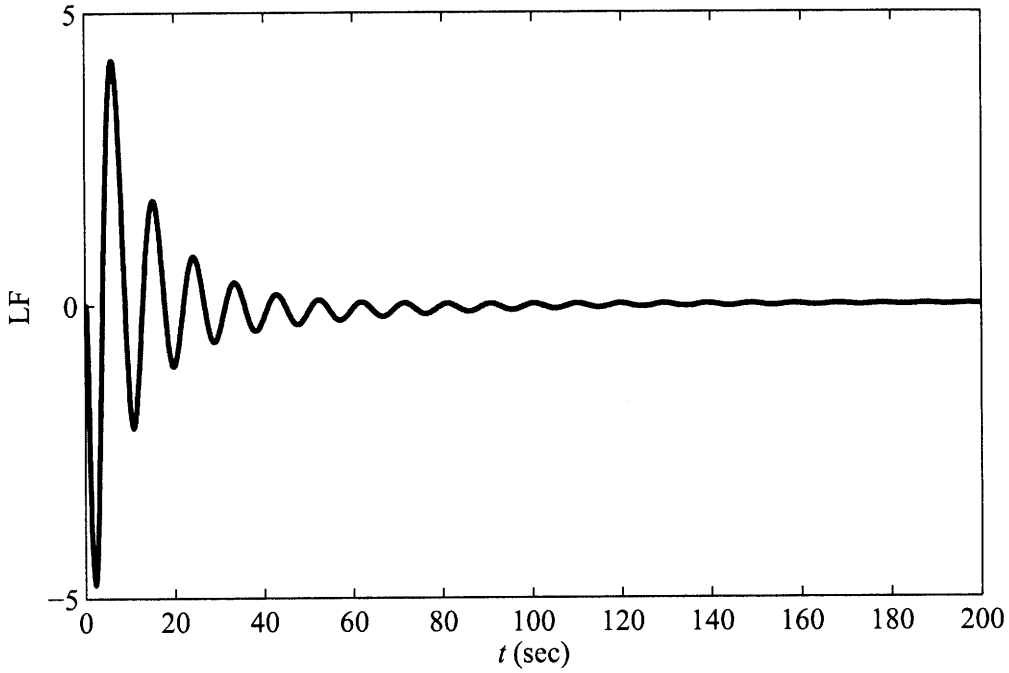

Figure B-9: A1 Loading Factor.

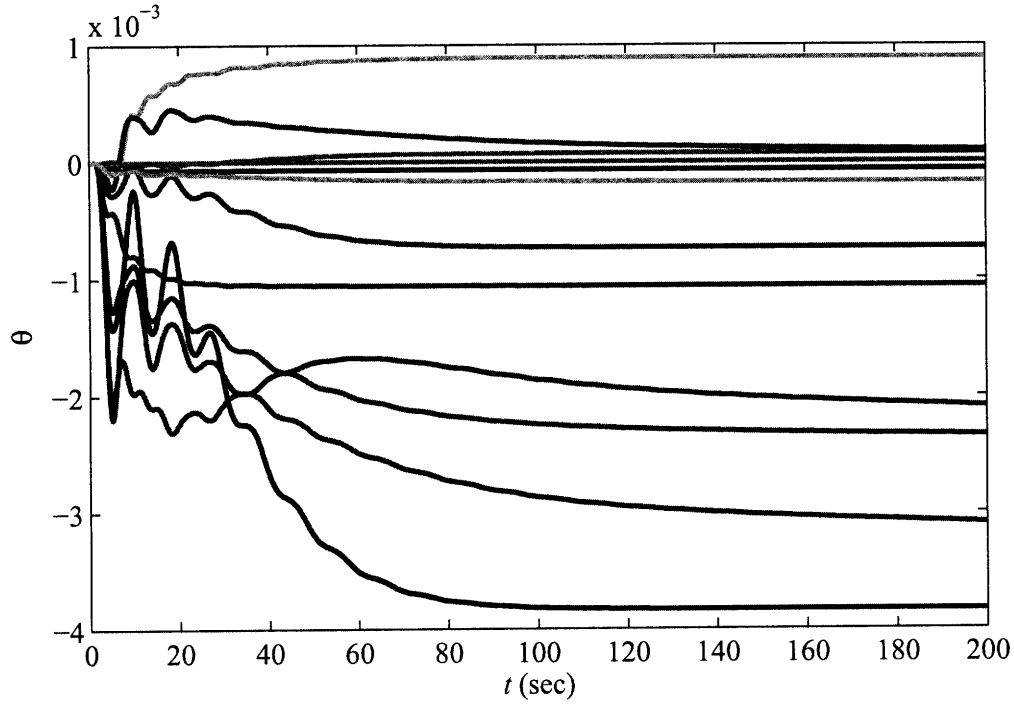

Figure B-10: A1 Adaptive parameters.

B.3 Simulation Study–N2

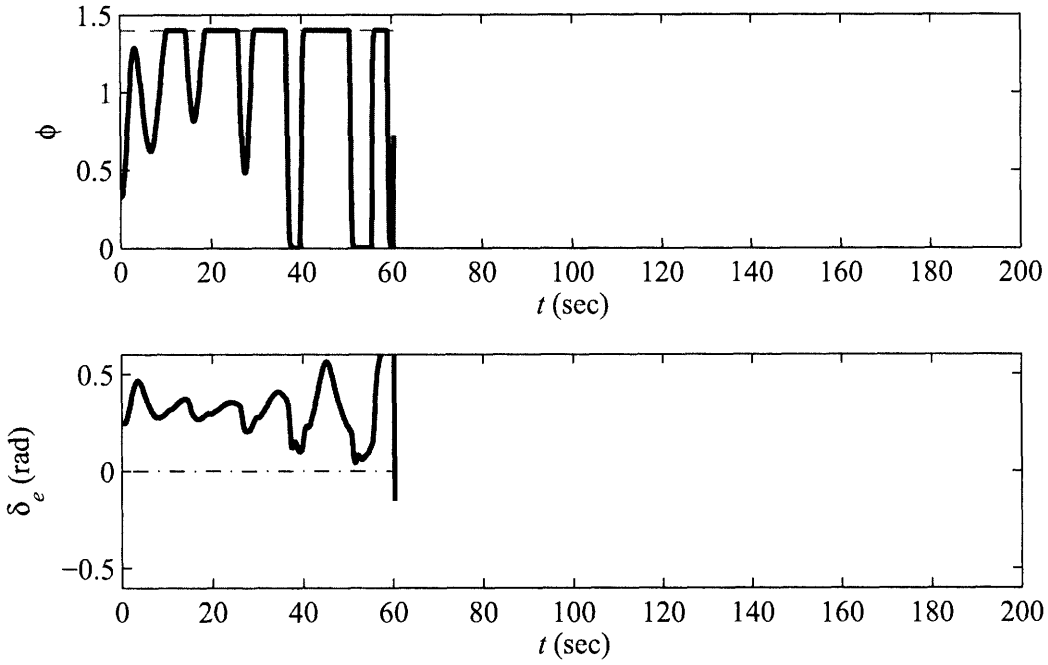

Figure B-11: N2 Control inputs.

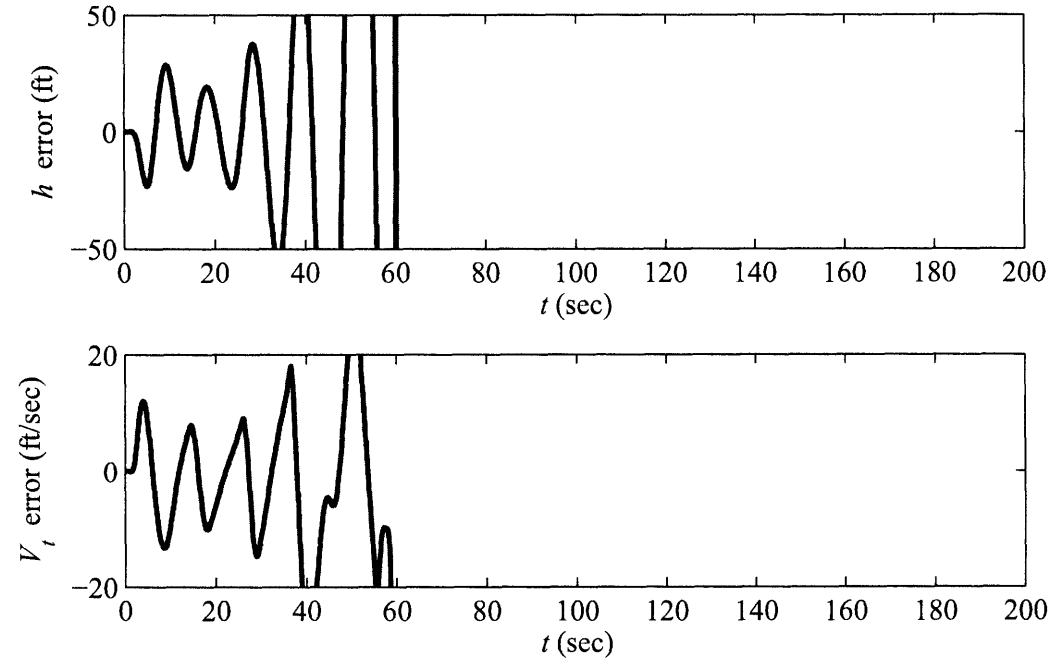

Figure B-12: N2 Command following error.

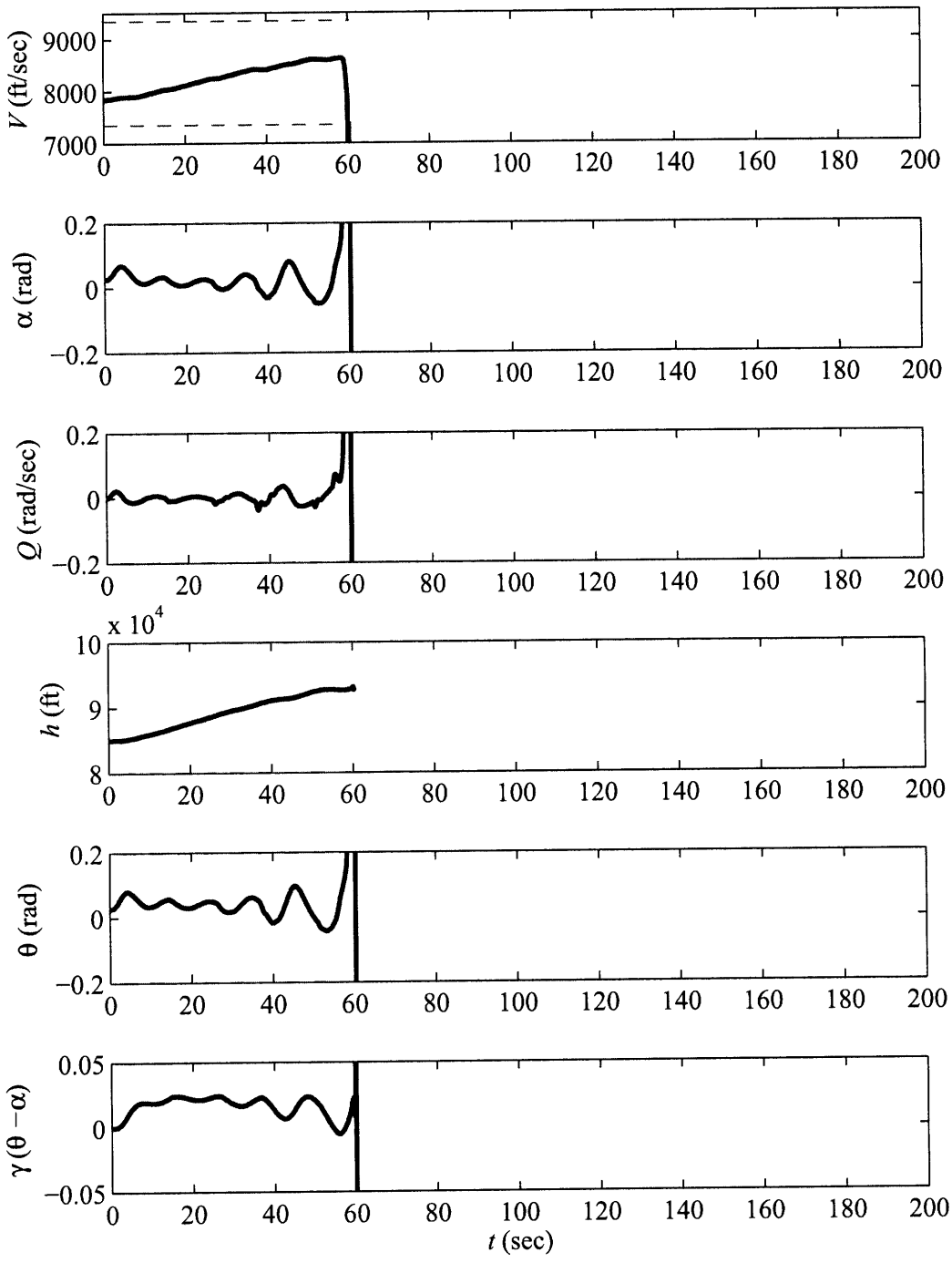

Figure B-13: N2 Rigid states.

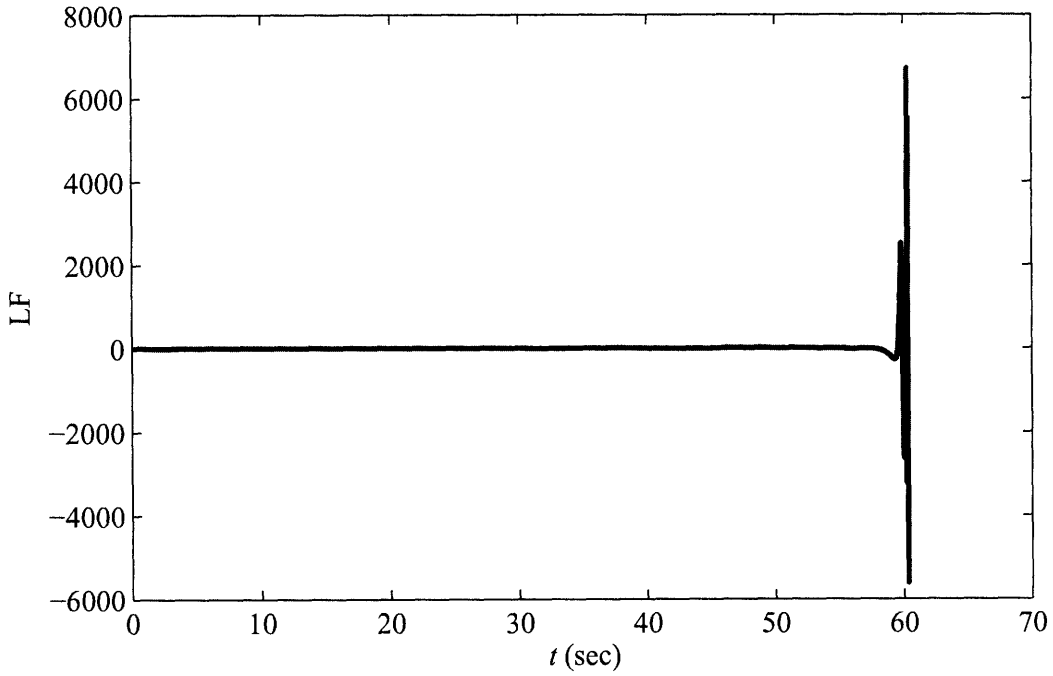

Figure B-14: N2 Loading Factor.

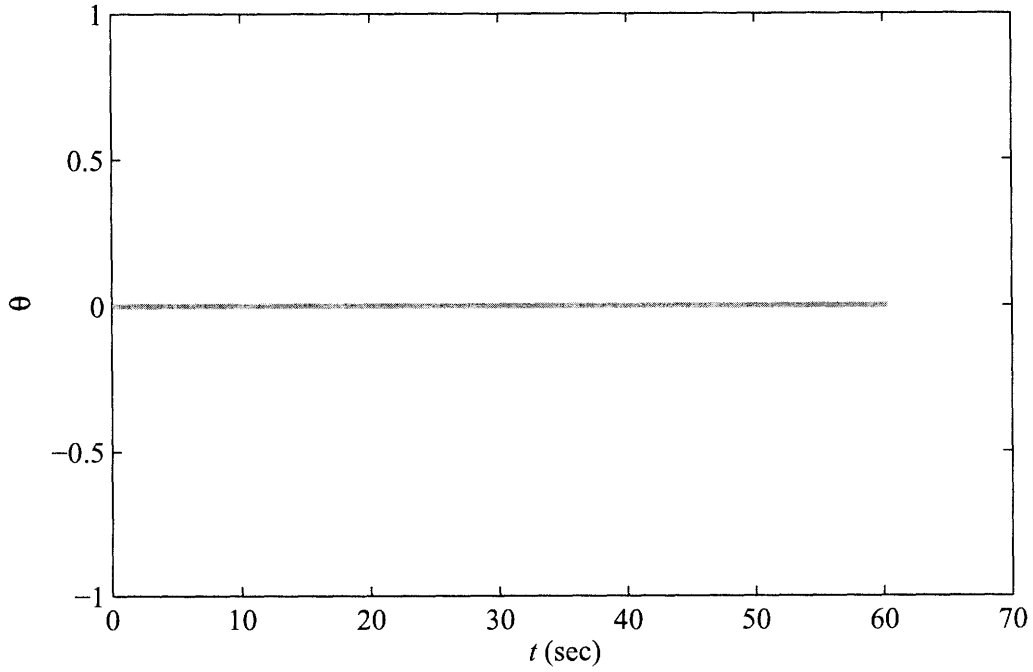

Figure B-15: N2 Adaptive parameters.

B.4 Simulation Study–A2

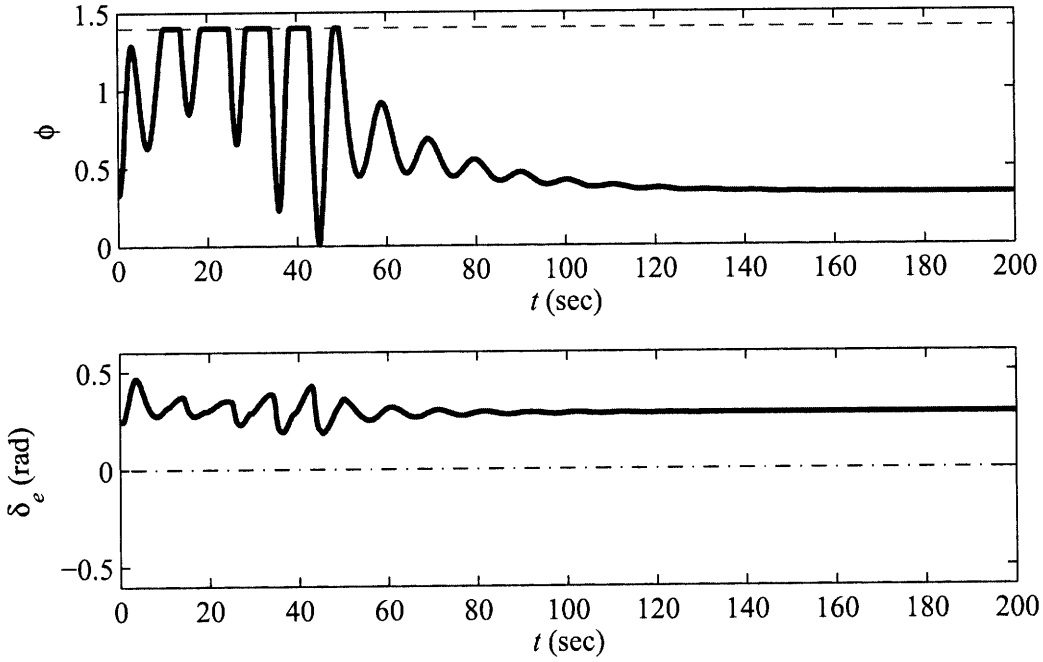

Figure B-16: A2 Control inputs.

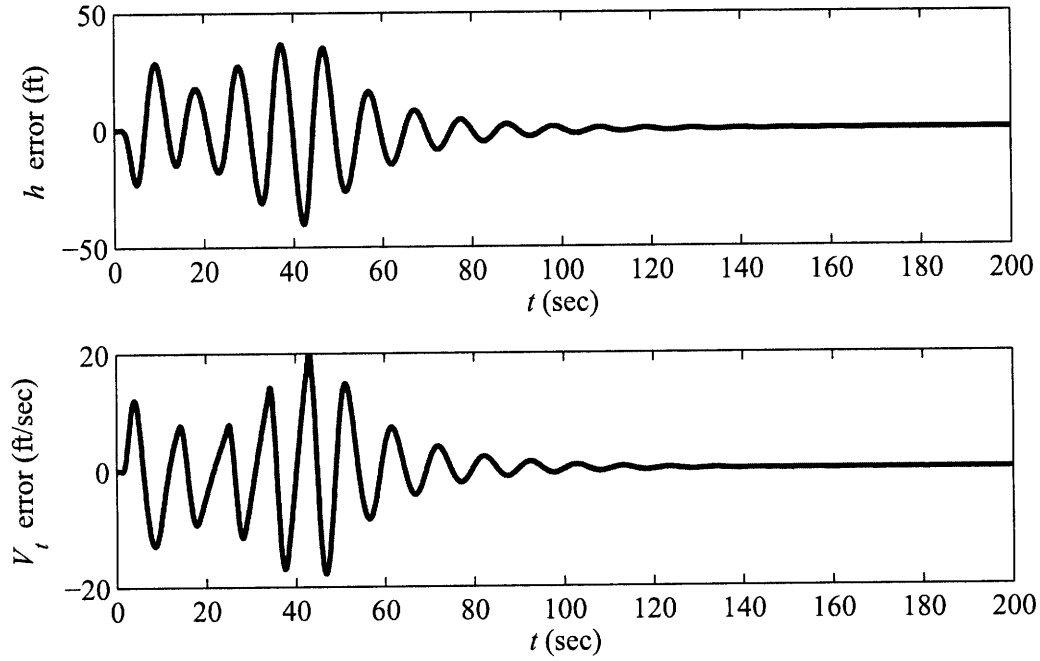

Figure B-17: A2 Command following error.

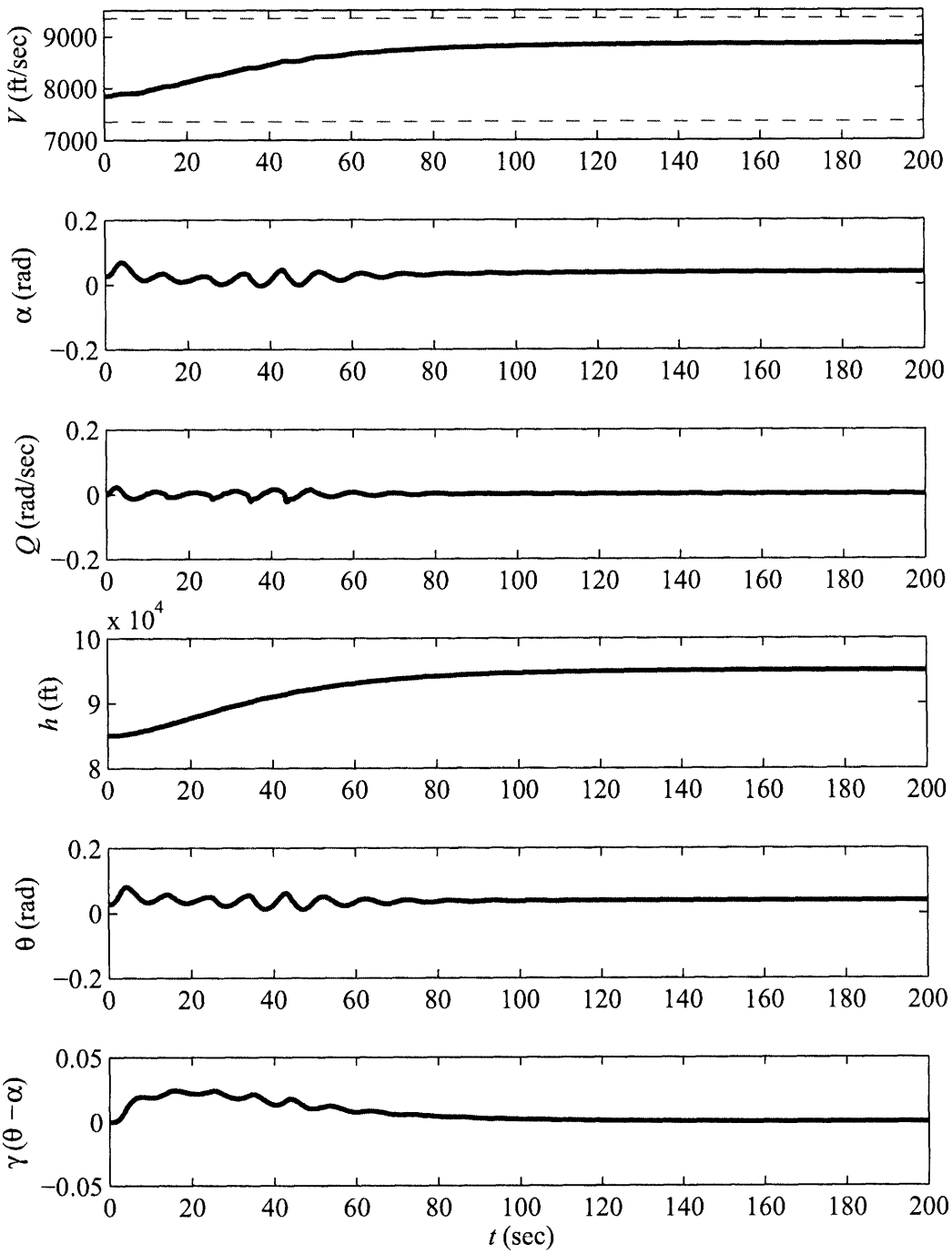

Figure B-18: A2 Rigid states.

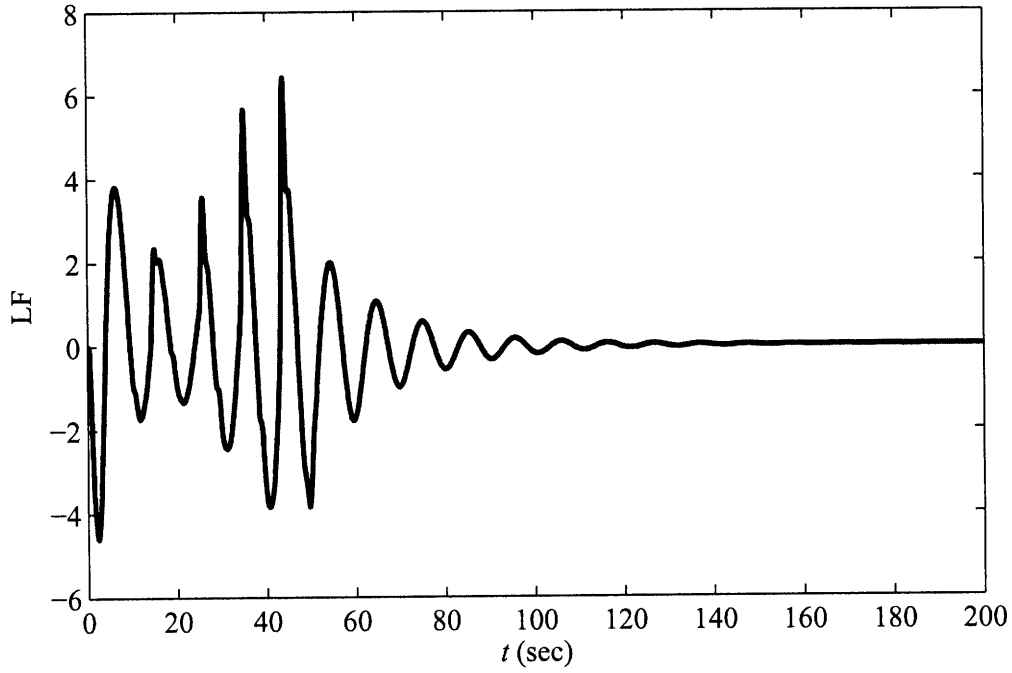

Figure B-19: A2 Loading Factor.

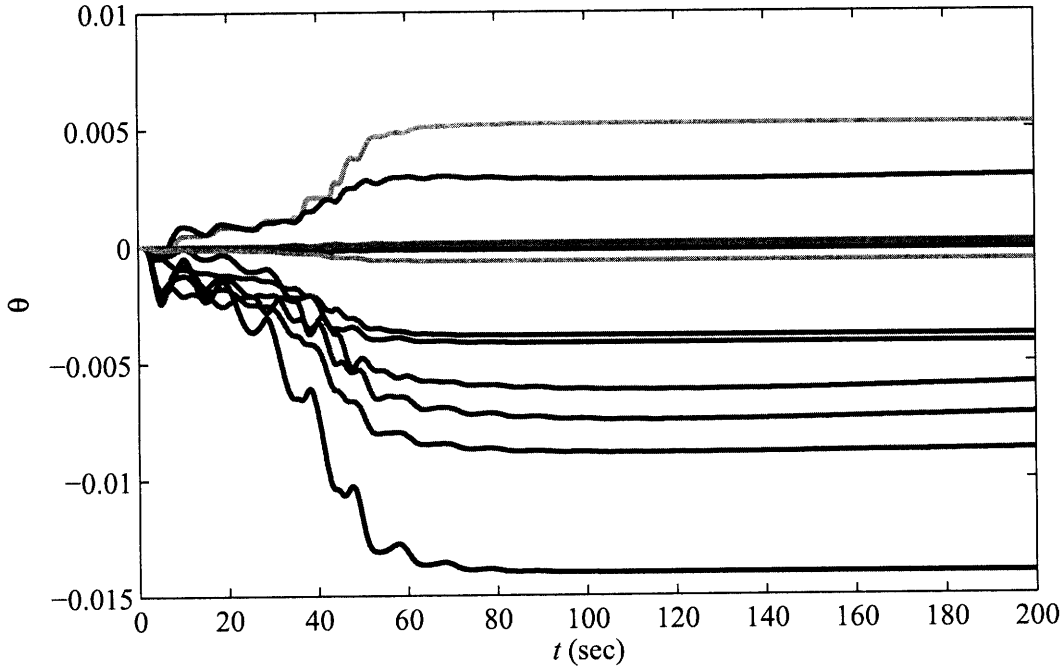

Figure B-20: A2 Adaptive parameters.

B.5 Simulation Study–N3

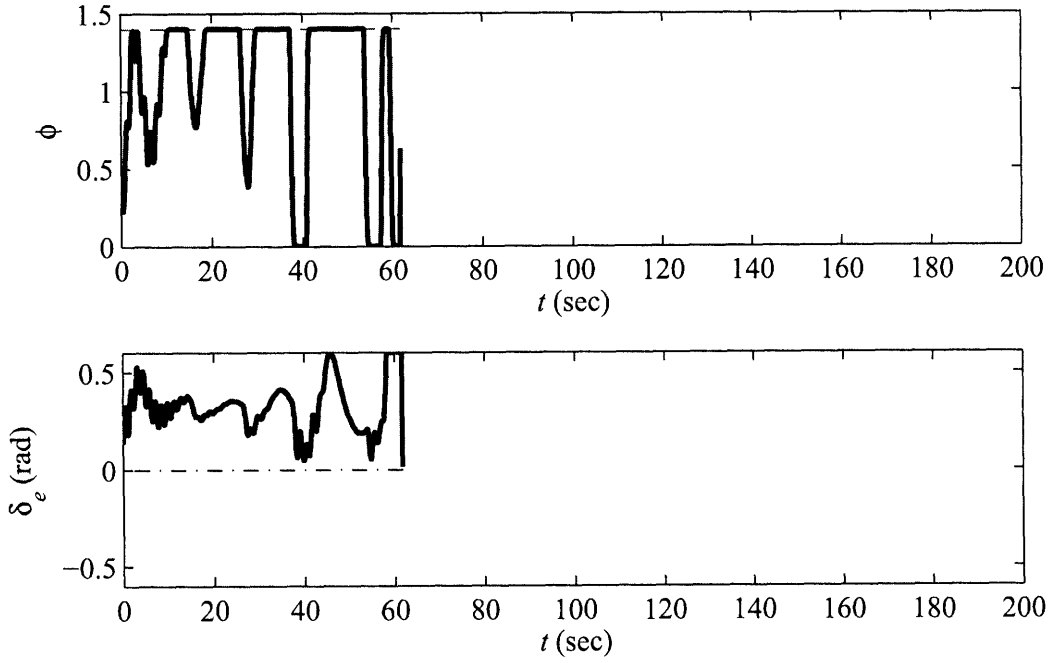

Figure B-21: N3 Control inputs.

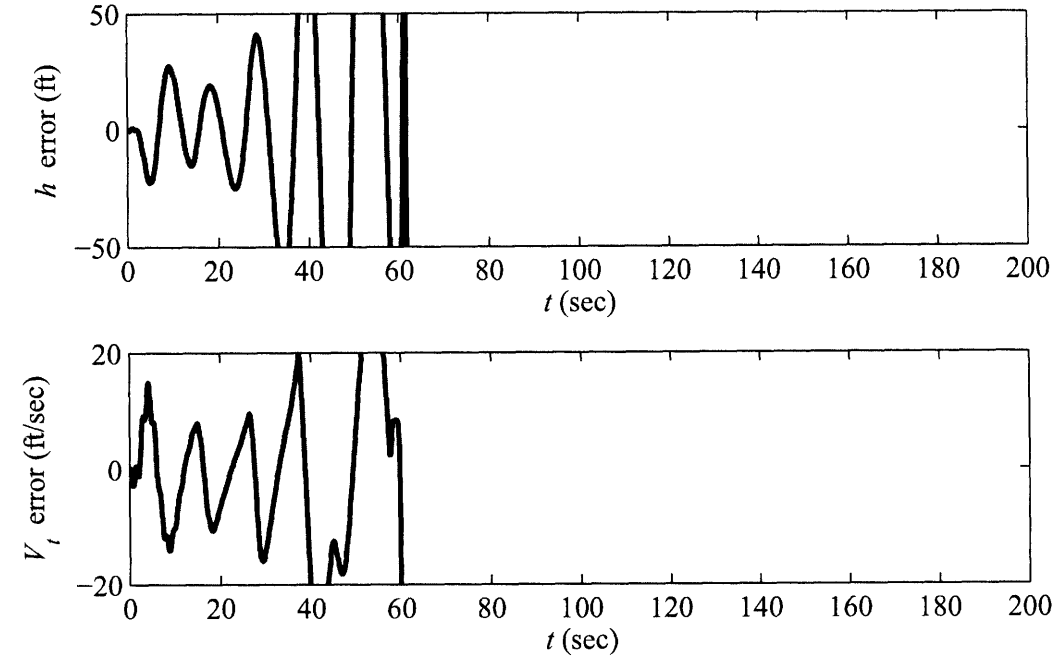

Figure B-22: N3 Command following error.

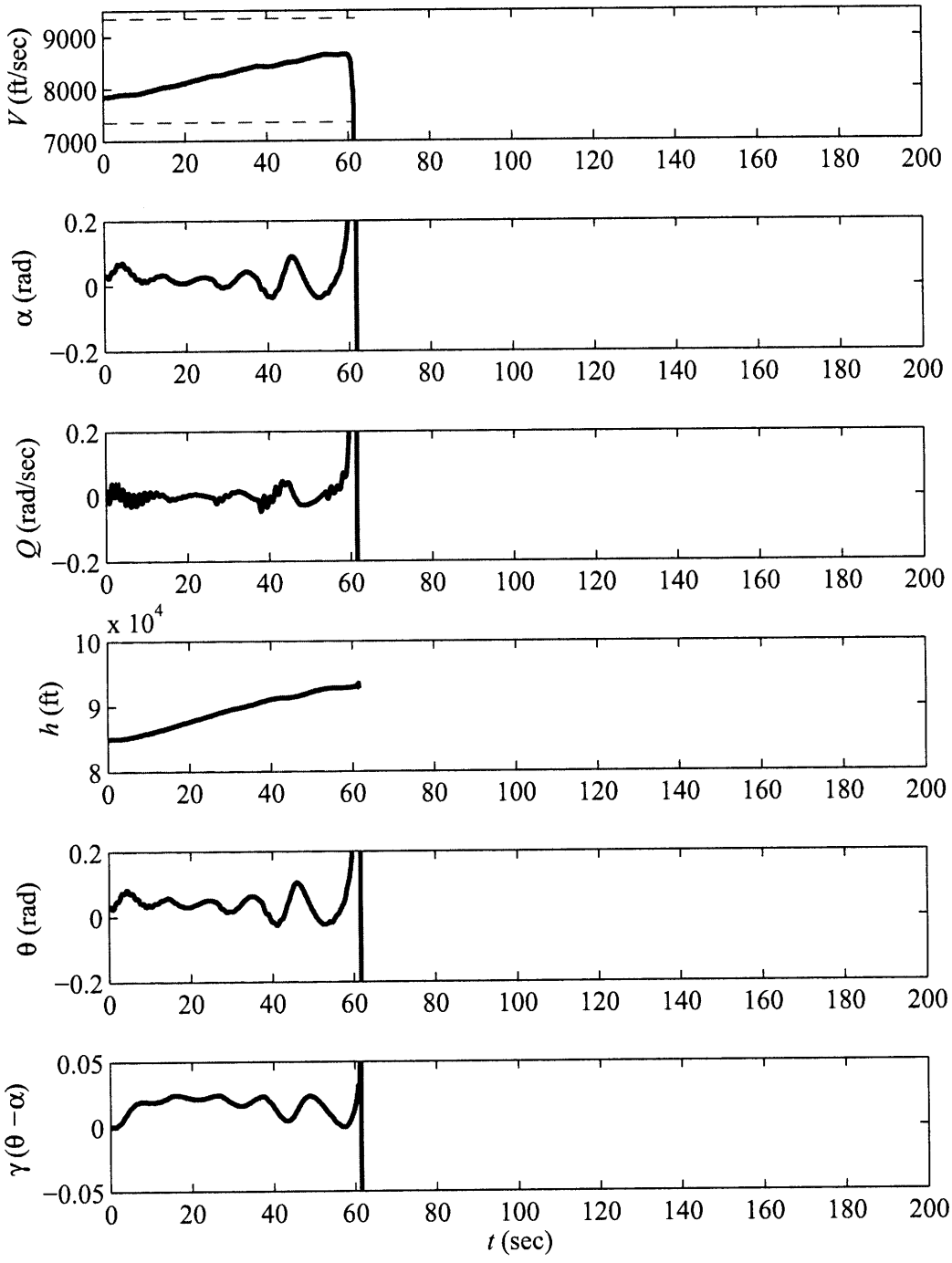

Figure B-23: N3 Rigid states.

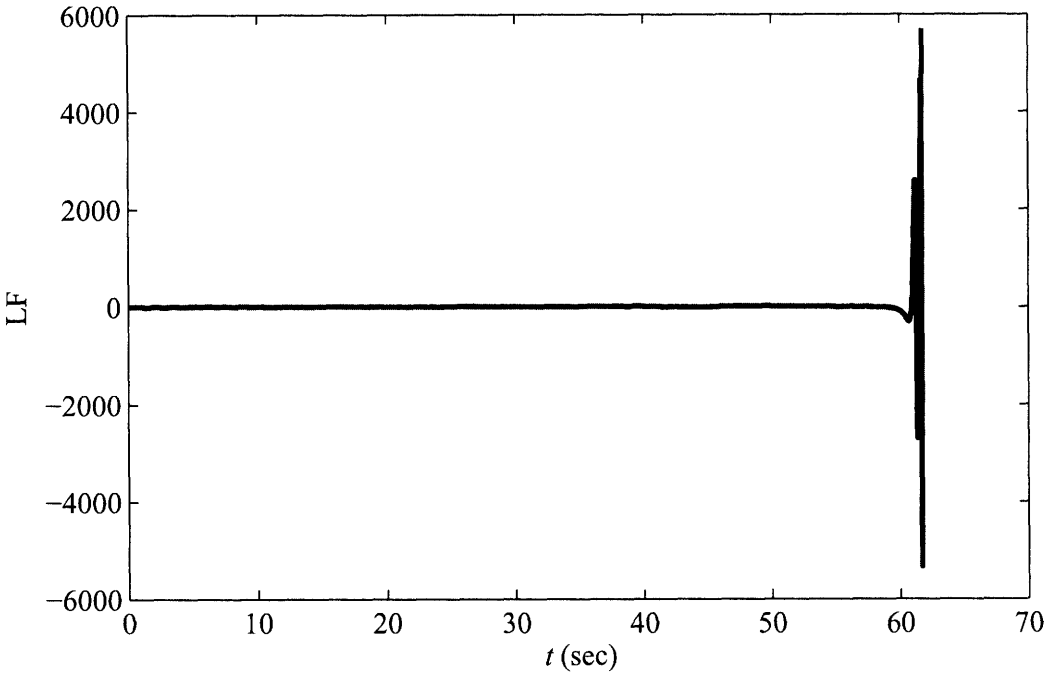

Figure B-24: N3 Loading Factor.

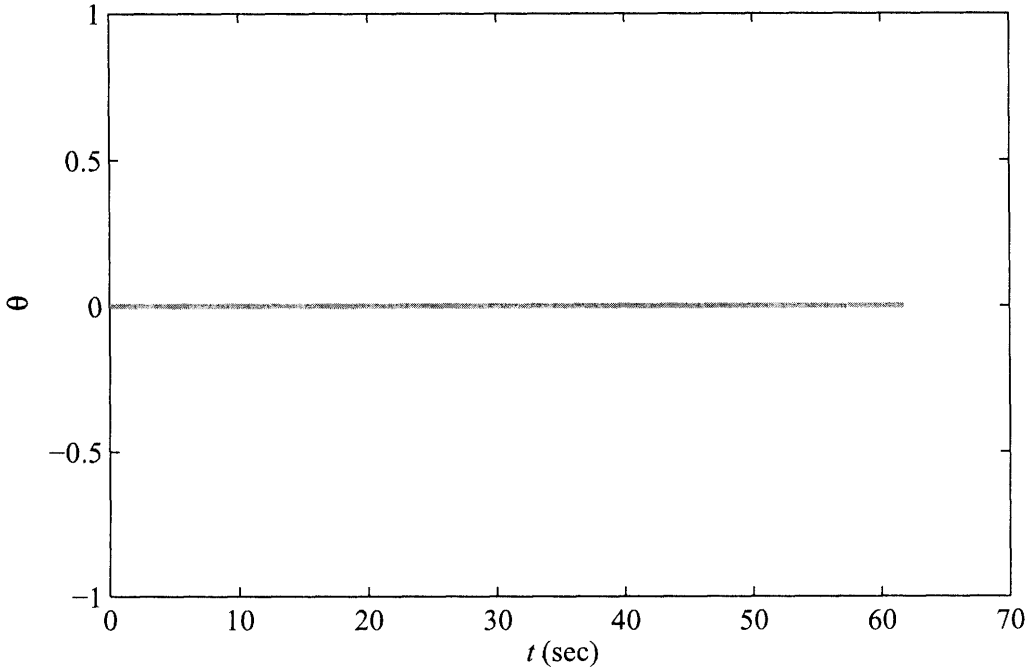

Figure B-25: N3 Adaptive parameters.

B.6 Simulation Study–A3

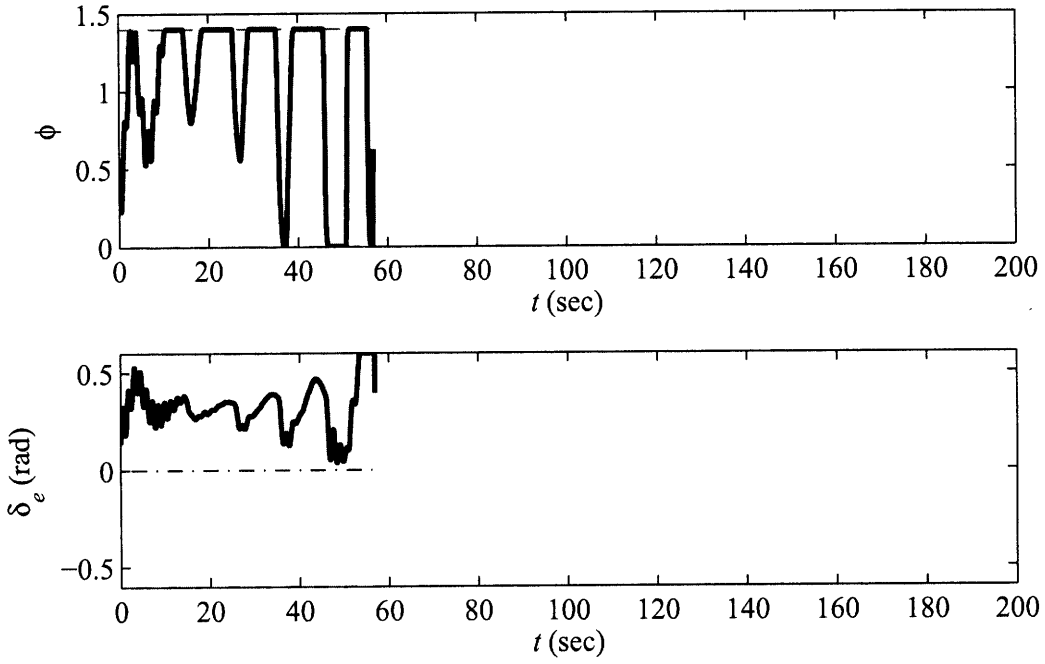

Figure B-26: A3 Control inputs.

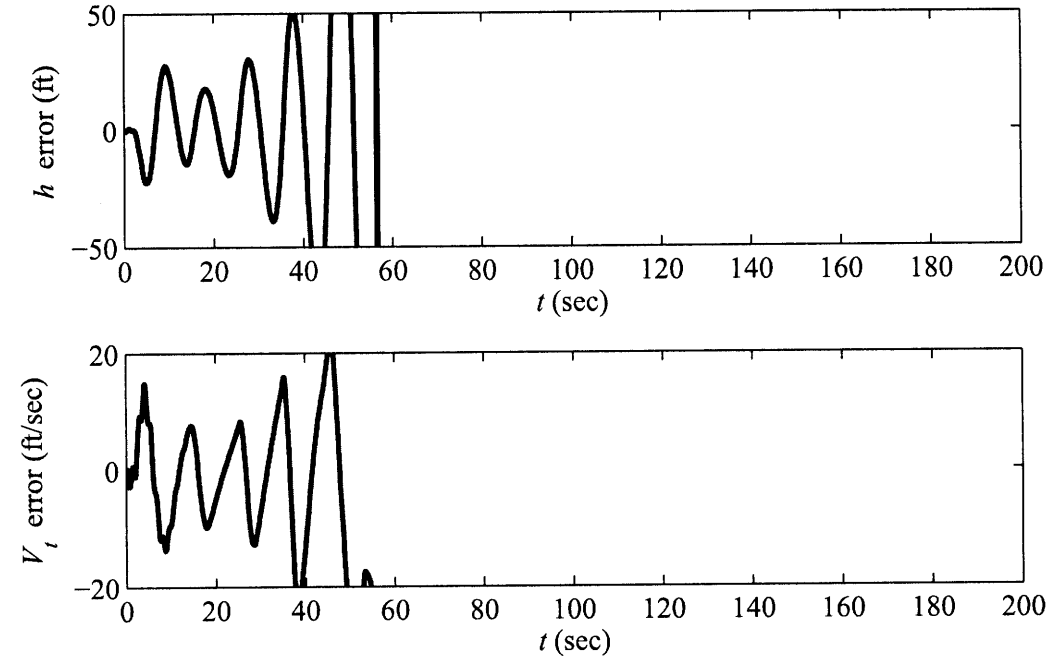

Figure B-27: A3 Command following error.

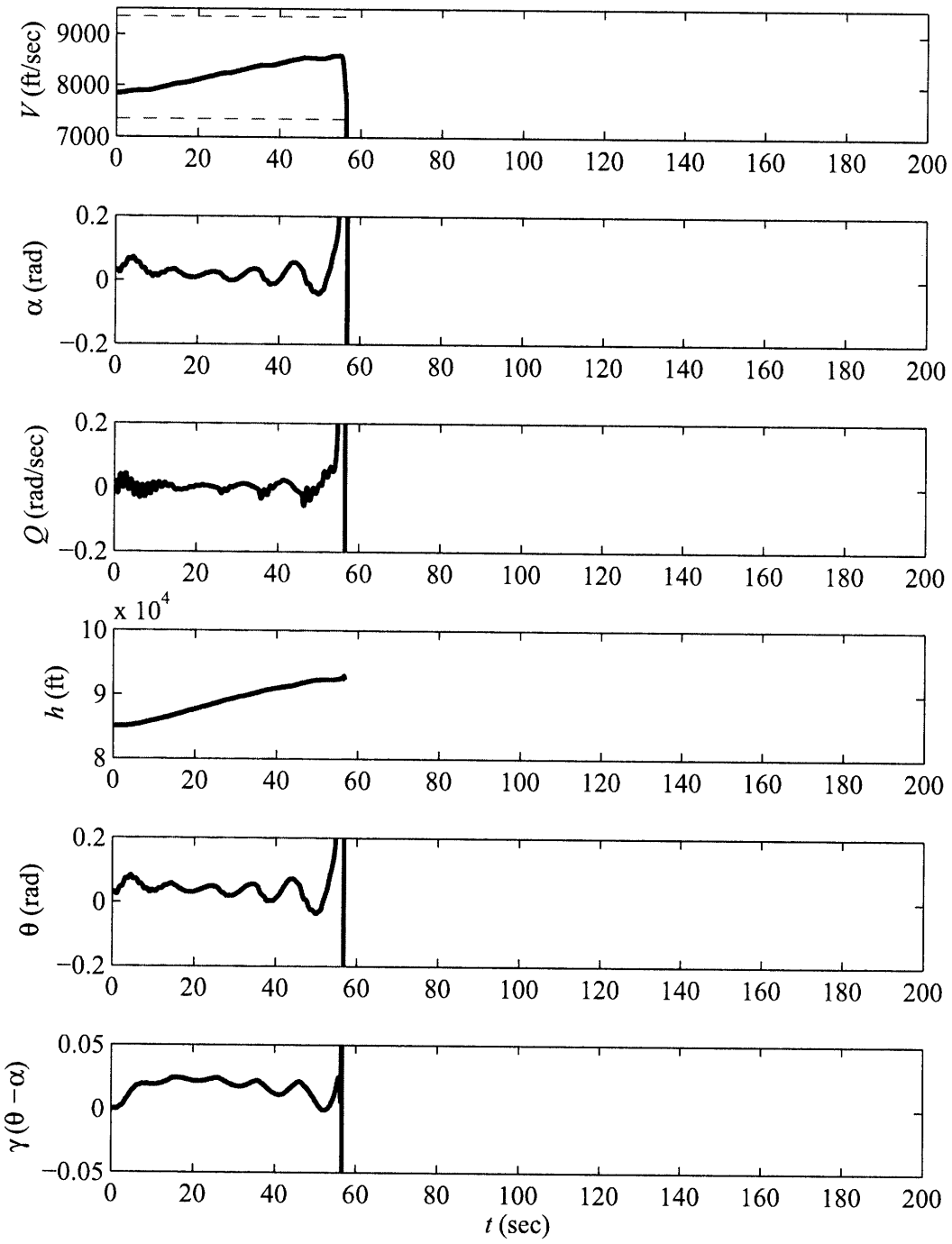

Figure B-28: A3 Rigid states.

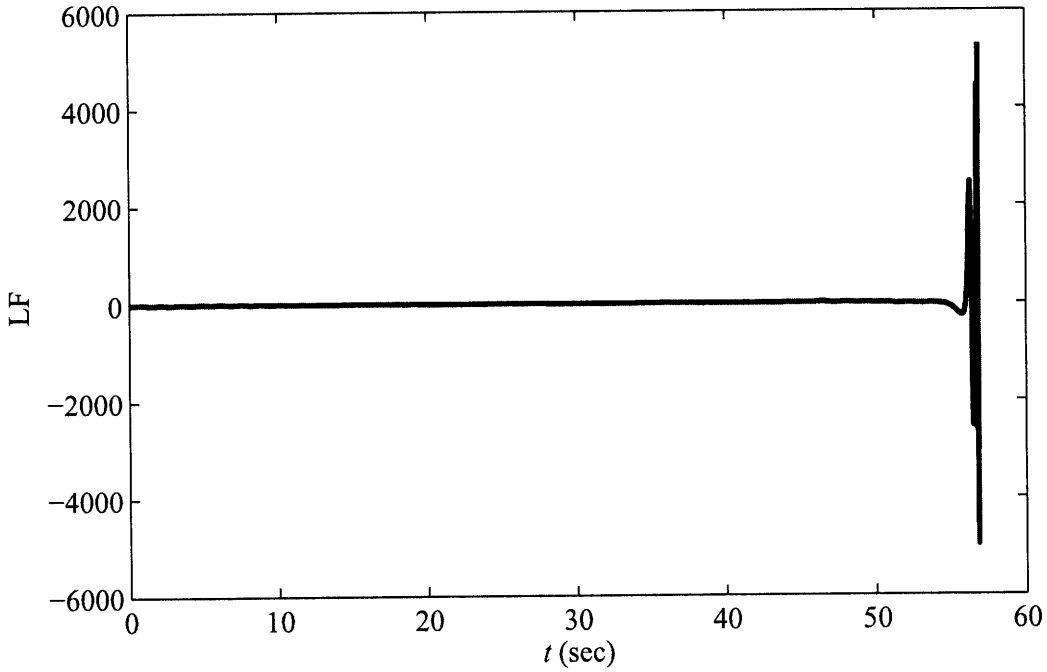

Figure B-29: A3 Loading Factor.

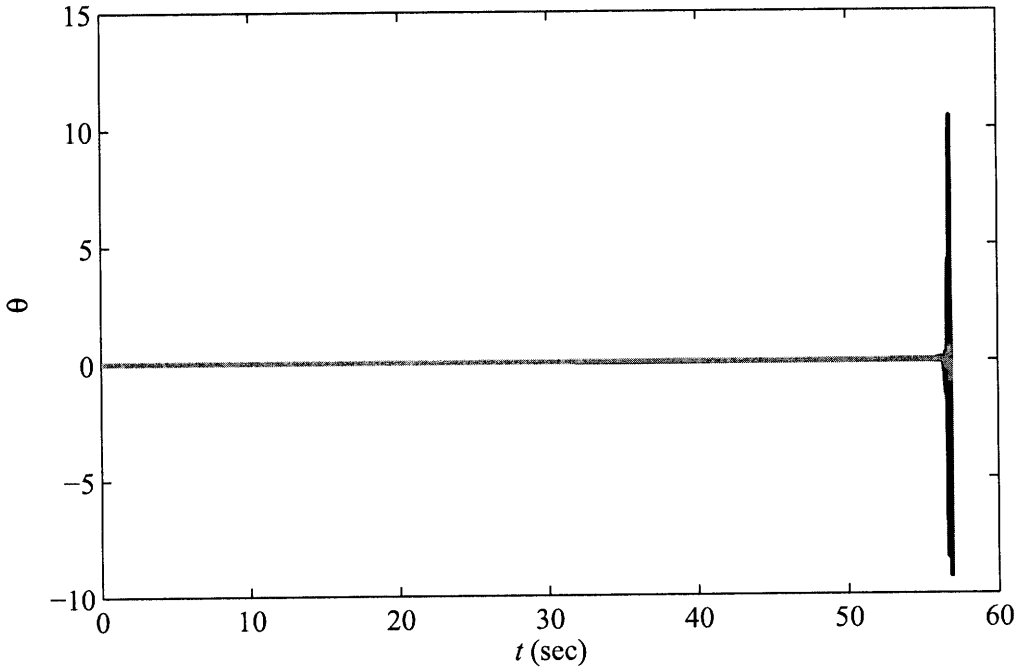

Figure B-30: A3 Adaptive parameters.

B.7 Simulation Study–N4

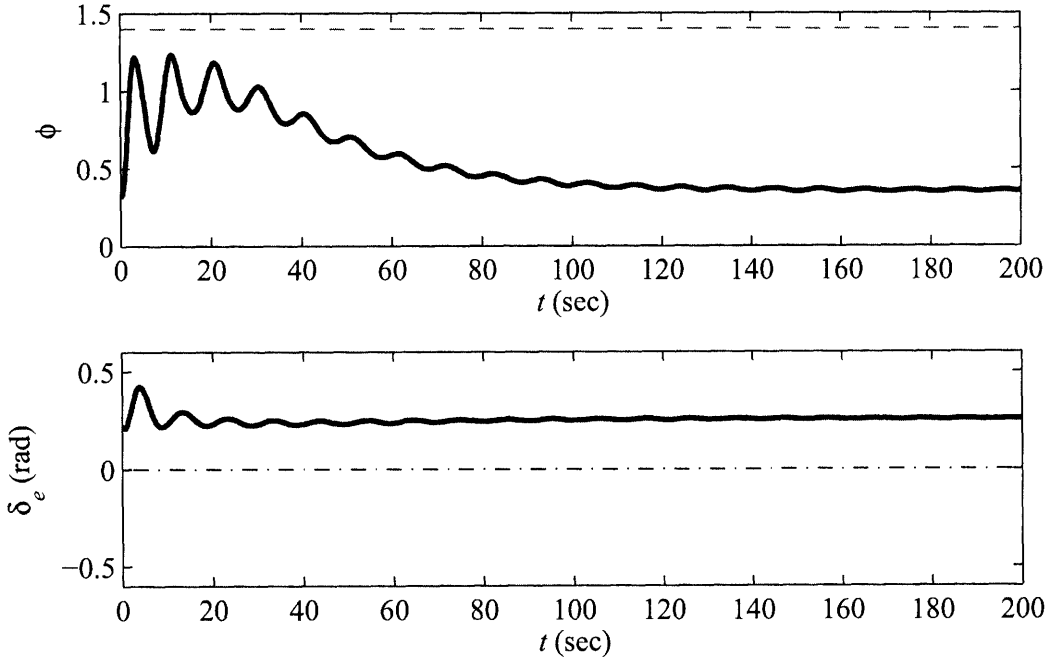

Figure B-31: N4 Control inputs.

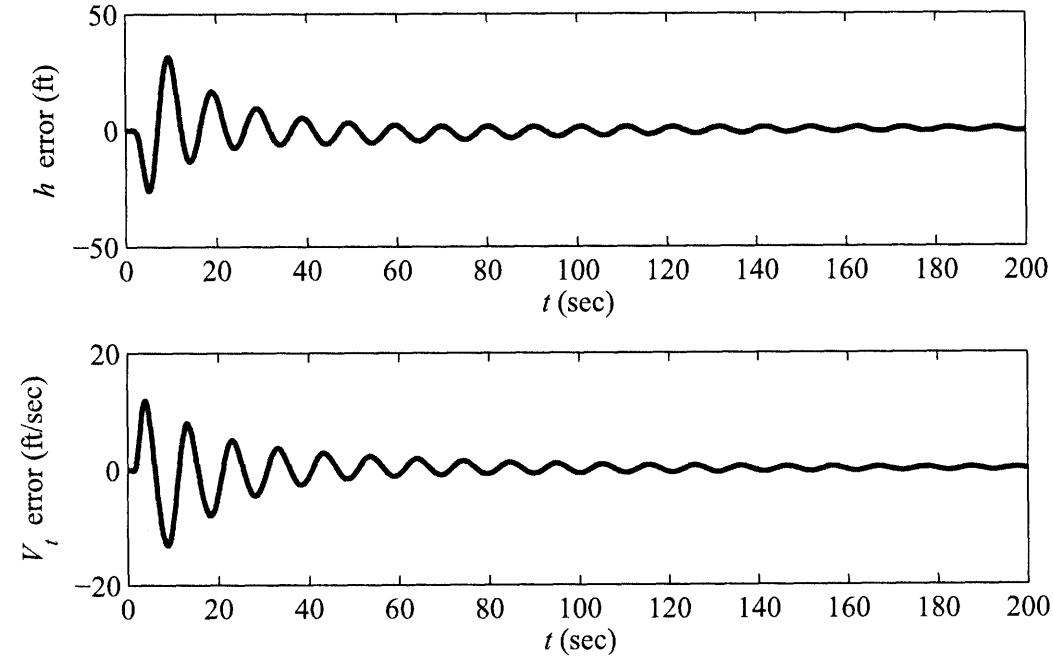

Figure B-32: N4 Command following error.

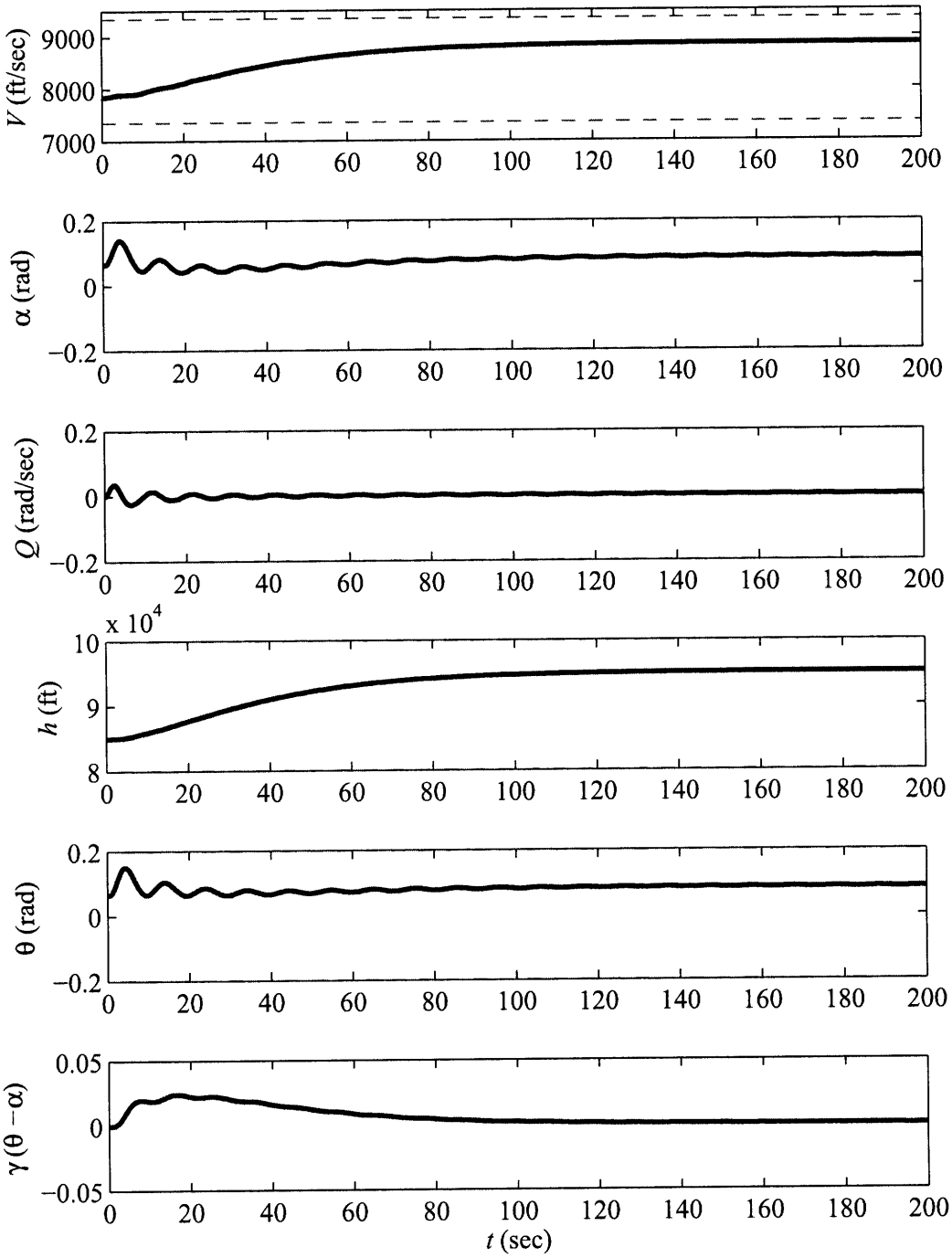

Figure B-33: N4 Rigid states.

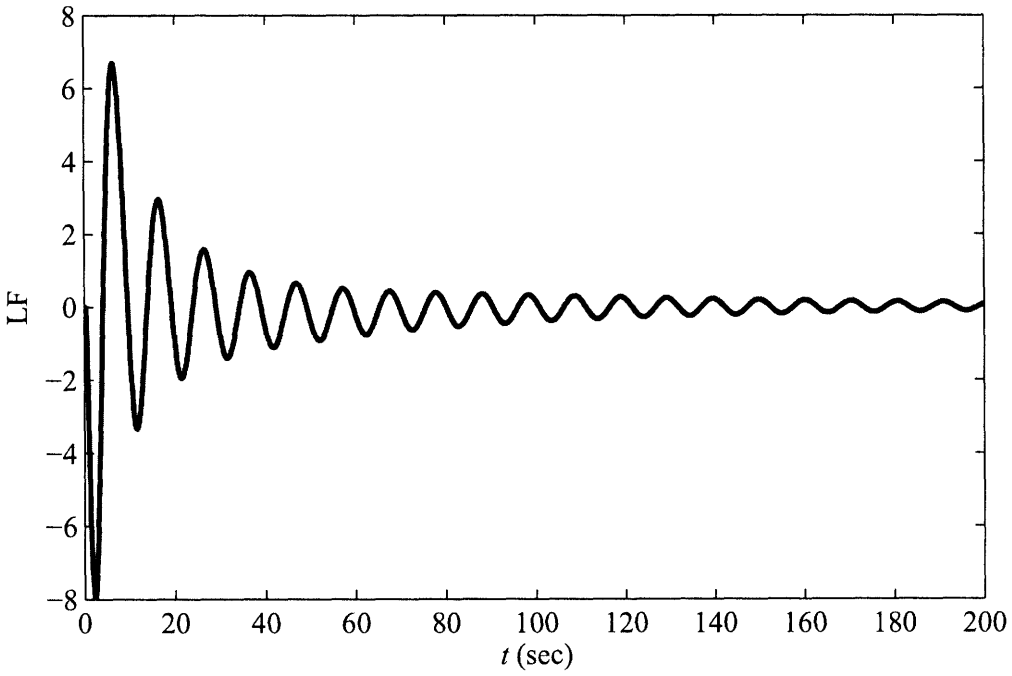

Figure B-34: N4 Loading Factor.

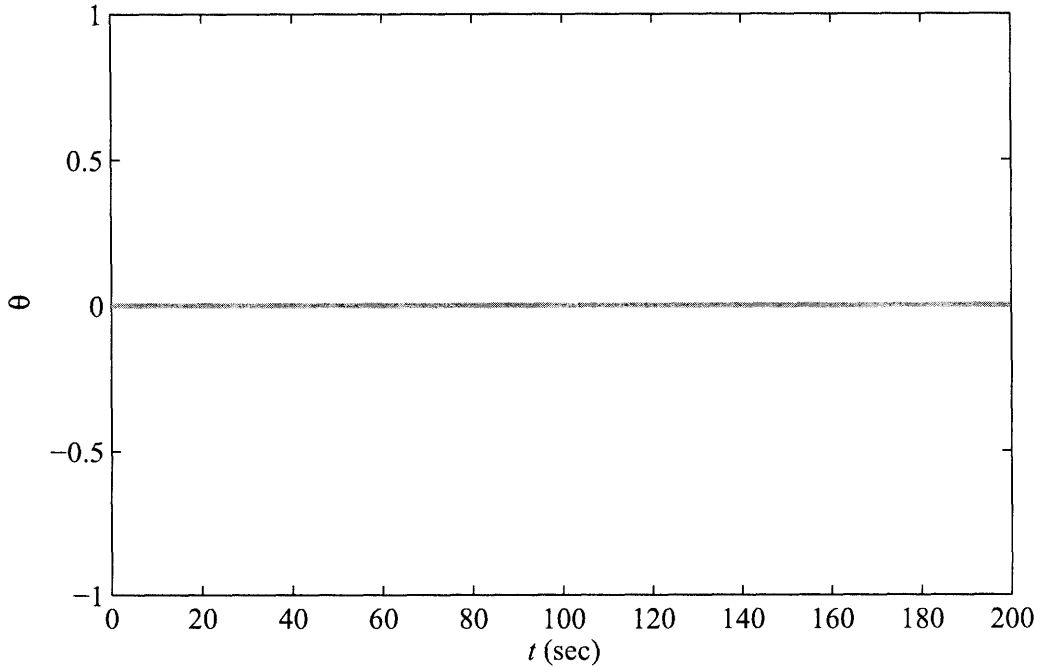

Figure B-35: N4 Adaptive parameters.

B.8 Simulation Study–A4

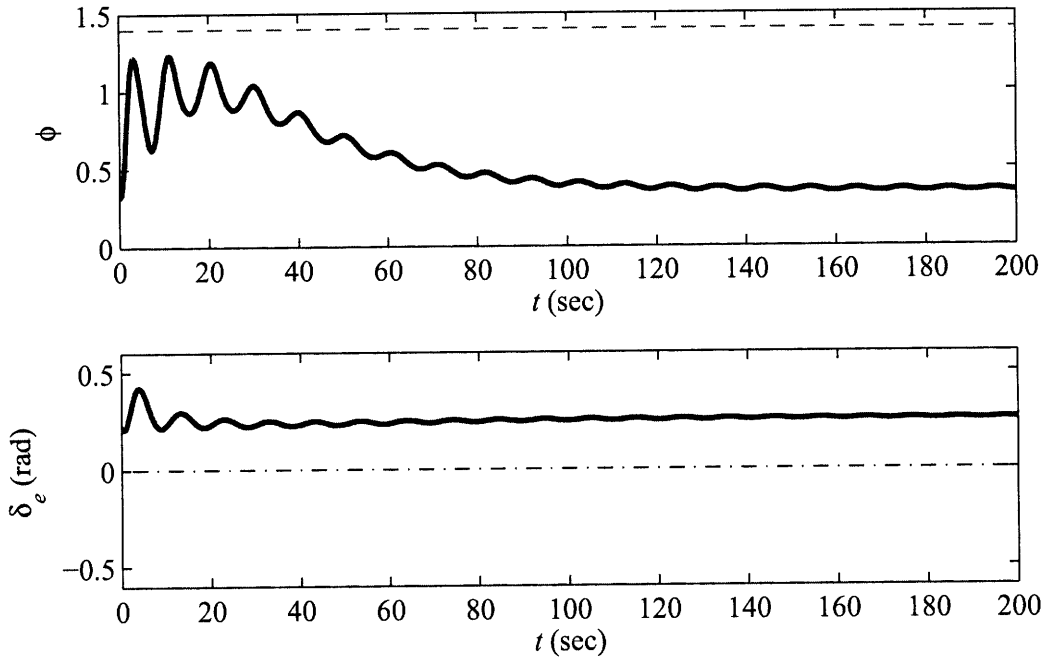

Figure B-36: A4 Control inputs.

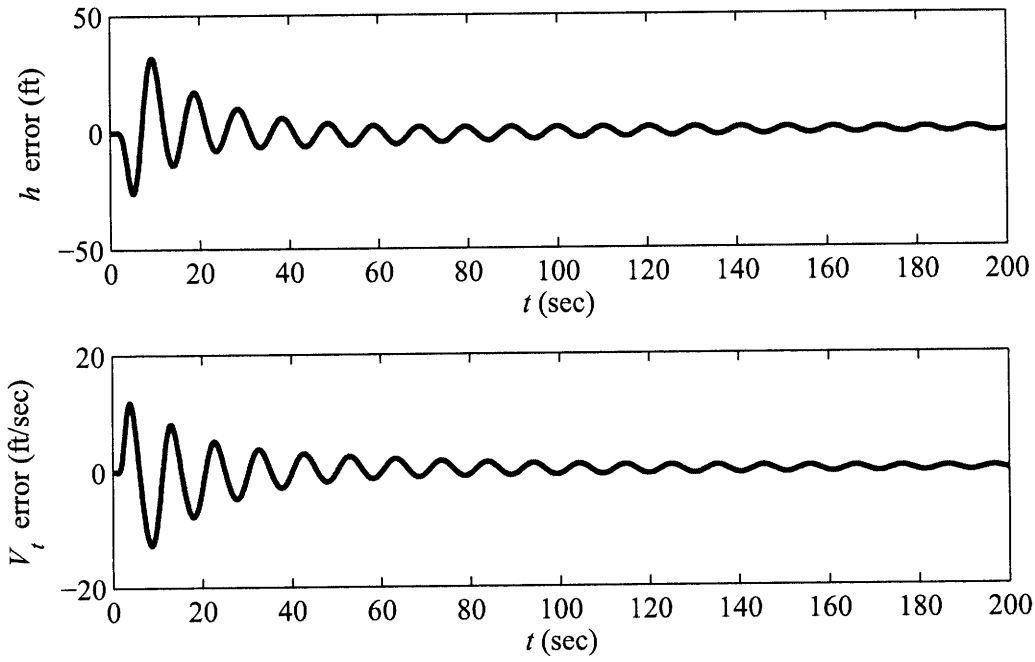

Figure B-37: A4 Command following error.

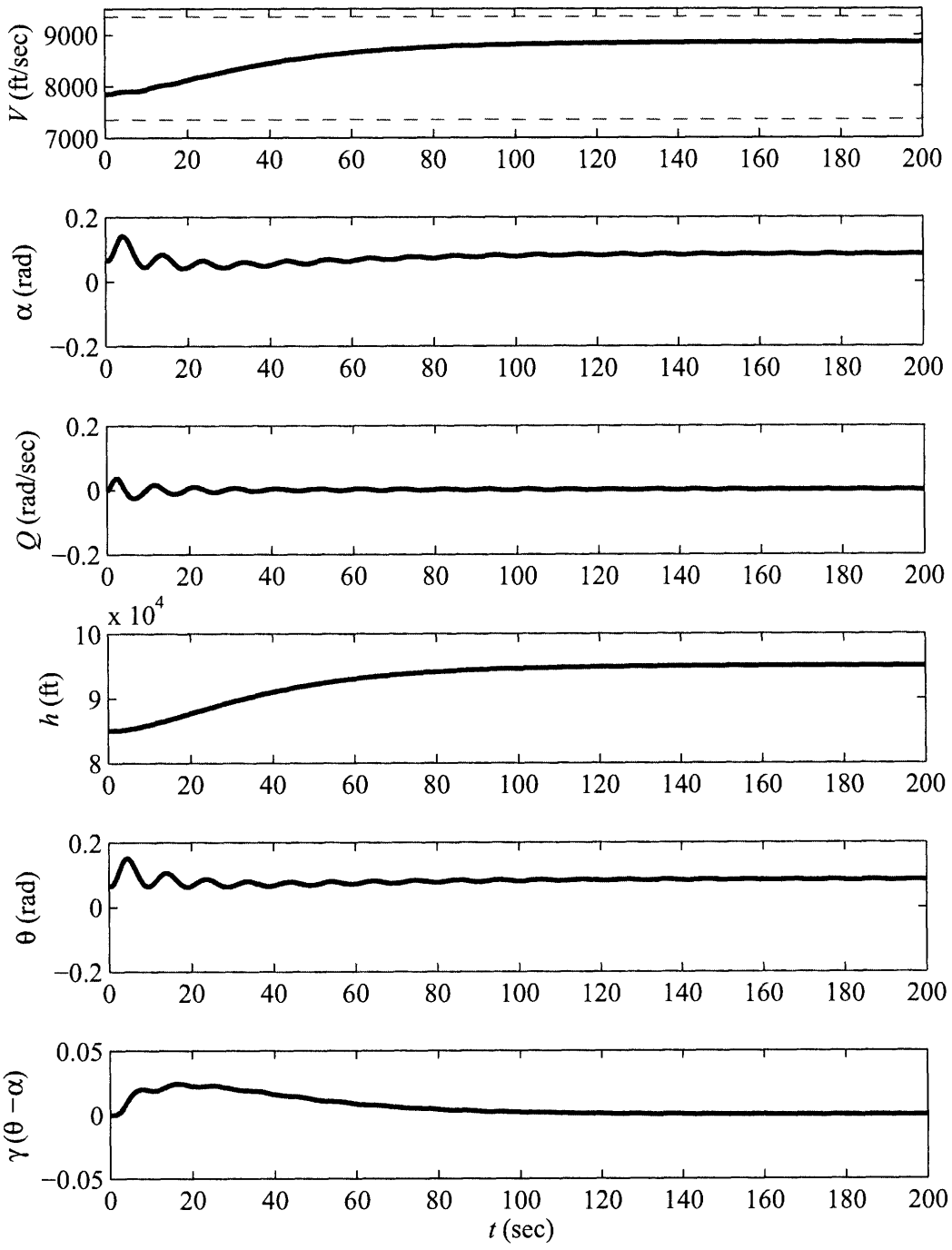

Figure B-38: A4 Rigid states.

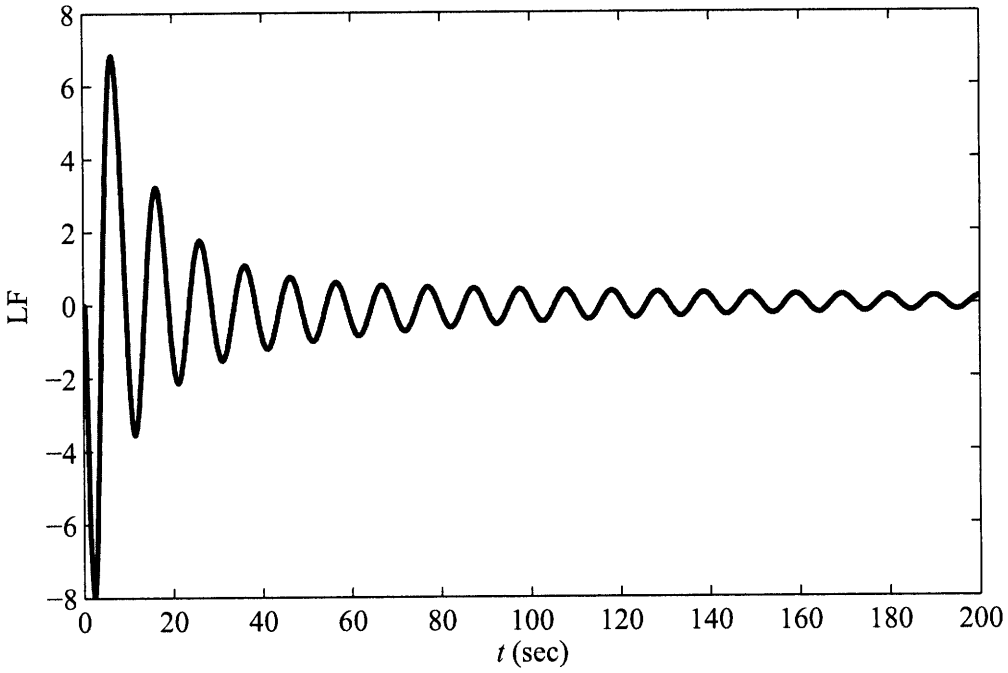

Figure B-39: A4 Loading Factor.

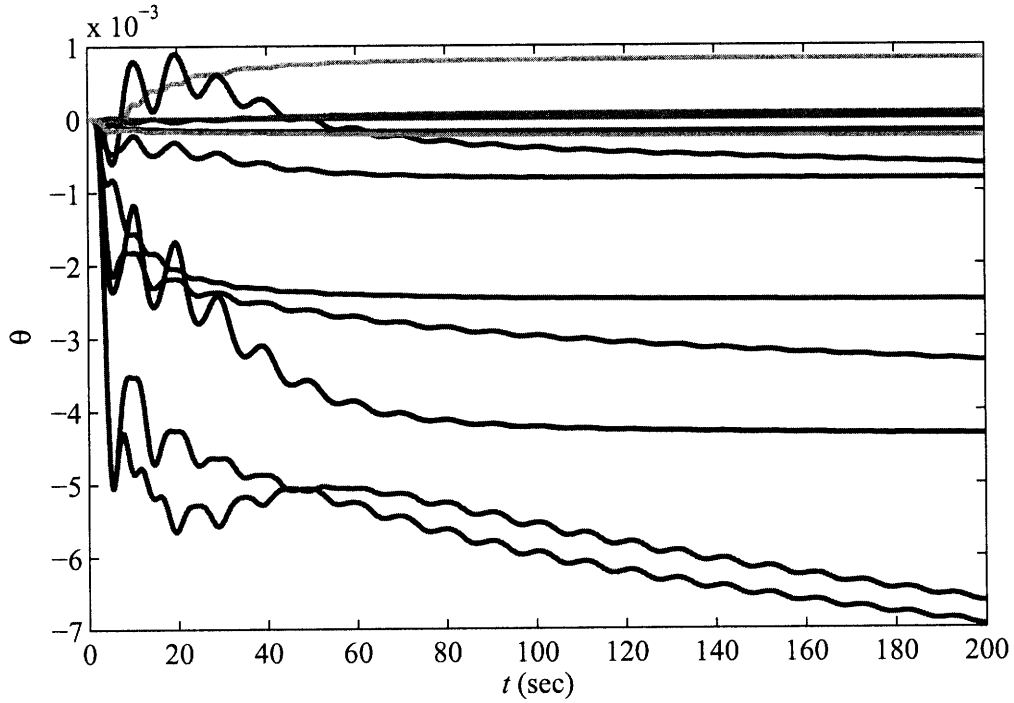

Figure B-40: A4 Adaptive parameters.

Appendix C

Control Design Parameters

The values used for control design are outlined in this section. For ease of notation several MATLAB functions were used, such as: `diag`, `eye`, and `zeros`.

The nominal control design involves the selection of the LQR cost function weighting parameters from Equation (3.15). The values used for the weighting parameters are as follows,

$$R = \texttt{diag}([10\ 300]^{\mathsf{T}}) \tag{C.1}$$

$$Q = C_z^{\mathsf{T}} \cdot Q_z \cdot C_z, \tag{C.2}$$

where

$$C_z = [\texttt{eye}(13,13); [0\ \ -1\ \ 0\ \ 0\ \ 1\ \ 0\ \ 0\ \ 0\ \ 0\ \ 0\ \ 0\ \ 0\ \ 0]] \tag{C.3}$$

$$Q_z = \texttt{diag}([0\ \ 1\ \ 10\ \ 0\ \ 1\ \ 0\ \ 0\ \ 0\ \ 0\ \ 1e-1\ \ 1e-1\ \ 1\ \ 10\ \ 1]^{\mathsf{T}}). \tag{C.4}$$

The reference model was selected as the nominal uncertain plant from Equation (3.7) along with the nominal feedback control gain as determined from (3.16). The reference model state jacobian is thus selected as

$$A_m = A_{\text{nominal}} + B_{\text{nominal}} K^{\mathsf{T}}, \tag{C.5}$$

with the reference model input jacobian chosen as

$$B_m = B_{\text{cmd}} K_{ff}. \tag{C.6}$$

The adaptive parameter, Q was selected as,

$$\begin{aligned} Q = \texttt{diag}([&10 \;\; 1 \;\; 0.01 \;\; 1 \;\; 10 \;\; 1 \;\; 1 \;\; 10 ... \\ &0.01 \;\; 1 \cdot 10^{0.1} \;\; 1 \cdot 10^{0.1} \;\; 0.01 \;\; 1]^{\mathsf{T}}). \end{aligned} \tag{C.7}$$

The adaptive rate parameter for θ was chosen using the following law,[[17]]

$$\Gamma_\theta = \texttt{diag}\left(\frac{\sup_{j=1,2} |\theta^*_{i,j}|}{\tau_m \|x^*_i\| \|B_m^{\mathsf{T}} P\| \|e_i\|}, \; i = 1, 2, ..., n \right) \tag{C.8}$$

where θ^* is the ideal gain as found in the text following (3.23), x^* is the steady state value of of the state vector x after a given reference command, and τ_m is the is the smallest time constant of the reference model. Using the above law and then scaling back the adaptive rate term down by 5 factors of 10 the following value was used.

$$\begin{aligned} \Gamma_\theta = \texttt{diag}(10^{-5} \cdot [&0.000000009623494 \;\; 1.056823857761001 \;\; 0.575672230351999 \\ &0.000000000127155 \;\; 0.961929999054892 \;\; 0.044689434889676 \\ &0.026054856539231 \;\; 0.038185101027099 \;\; 0.160275373463354 \\ &0.000399037265467 \;\; 0.000001849335504 \;\; 0.007608541778292 \\ &0.011914958597330]^{\mathsf{T}}) \end{aligned}$$

The other adaptive control design parameters are as follows:

$$\sigma_\theta = \texttt{zeros}(13, 13) \tag{C.9}$$

$$\Gamma_\lambda = \texttt{diag}(1 * 10^{-6} * \texttt{ones}(2, 1)) \tag{C.10}$$

$$\sigma_\lambda = \texttt{zeros}(13, 13) \tag{C.11}$$

Bibliography

[1] R. J. Admas and et al. *Robust Multivariable Flight Control.* Springer-Verlag, 1994.

[2] John D. Anderson. *Modern Compressible Flow: with Hystorical Perspective.* McGraw-Hill Science, 2002.

[3] Anon. Equations, tables, and charts for compressible flow. Technical Report NACA–1135, Ames Aeronautical Laboratory, National Advisory Committee for Aeronautics, Moffett Field, CA, 1953.

[4] Anon. *Handbook of Aviation Fuel Properties.* Coordinating Research Council, Atlanta, GA, 1983.

[5] Anon. Dryden flight research center nasa graphics x–43a/hyper–x, 2004. `http://www.dfrc.nasa.gov/Gallery/Graphics/X-43A/index.html`.

[6] Anon. Dryden flight research center nasa images x–43a/hyper–x, 2004. `http://www.dfrc.nasa.gov/Gallery/Photo/X-43A/Large/index.html`.

[7] Michael A. Bolender and David B. Doman. Nonlinear longitudinal dynamical model of an air-breathing hypersonic vehicle. *Journal Spacecraft and Rockets*, 44(2), March-April 2007.

[8] Michael A. Bolender and Davod B. Doman. Flight path angle dynamics of air-breathing hypersonic vehicles. In *AIAA Guidance, Navigation, and Control Conference and Exhibit*, 21-24 August 2006. Keystone,Colorado.

[9] Michael A. Bolender, Michael W. Oppenheimer, and David B. Doman. Effects of unsteady and viscous aerodynamics on the dynamics of a flexible air-breathing hypersonic vehicle. In *AIAA GAFMC*, August 2007. Hilton Head, South Carolina.

[10] Frank R. Chavez and David K. Schmidt. Analytical aeropropulsive/aeroelastic hypresonic-vehicle model with dynamic analysis. *Journal of Guidance, Control, and Dynamics*, 17(6), Nov-Dec 1994.

[11] Andrew Clark, Chivey Wu, Maj Mirmirani, Sangbum Choi, and Mathew Kuipers. Development of an airframe-propulsion integrated generic hypersonic

vehicle model. In *AIAA Aerospace Sciences Meetings and Exhibit*, January 2006. Reno, Nevada.

[12] R. D. Colgren. Nonlinear h-inf control of a missle's roll axis. *ACC*, 1994. Baltimore, MD.

[13] R. D. Colgren, D. Enns, and et al. Structured singular value synthesis applied to the f–117a. In *IFAC World Congress*, 1996. San Francisco, CA.

[14] L. G. Crespo, D. P. Giesy, and S. P. Kenny. Robust analysis and robust design of uncertain systems. *AIAA Journal*, 46(2), 2008.

[15] L.G. Crespo. Sampling-based techniques for the estimation of probabilistic sensitivities. In *AIAA NDA*, 2008.

[16] L.G. Crespo. A verification-driven approach to control tuning. In *AIAA Guidance, Navigation, and Control Conference and Exhibit*, 2008.

[17] Z. Dydek, H. Jain, J. Jang, A. Annaswamy, and E. Lavretsky. Theoretically verifiable stability margins for an adaptive controller. In *AIAA Guidance, Navigation, and Control Conference and Exhibit*, 21-24 August 2006. Keystone,Colorado.

[18] Zachary T. Dydek. Guaranteed margins and performance for an adaptive flight control system and application on the x-15 research airplane. Master's thesis, Massachusetts Institute of Technology.

[19] L. Fiorentini, A. Serrani, Michael A. Bolender, and David B. Doman. Nonlinear robust/adaptive controller design for an air-breathing hypersonic vehicle model. In *AIAA Atmospheric Flight Mechanics Conference and Exhibit*, Aug. 20-23 2007. Hilton Head, South Carolina.

[20] L. Fiorentini, A. Serrani, Michael A. Bolender, and David B. Doman. Nonlinear control of a hypersonic vehicle with structural flexibility. In *IEEE Conference on Decision and Control*, 2008. Submitted.

[21] Travis E. Gibson and Anuradha M. Annaswamy. Adaptive control of hypersonic vehicles in the presence of thrust and actuator uncertainties. In *AIAA Guidance, Navigation, and Control Conference and Exhibit*, 18-21 August 2008. Honolulu,Hawaii.

[22] Travis E. Gibson, Luis G. Crespo, and A. M. Annaswamy. Adaptive control of hypersonic vehicles in the presence of modeling uncertainties. In *Proceedings of the American Control Conference*, 2009. Submitted.

[23] K.P. Groves, A. Serrani, S. Yurkovich, M. Bolender, and D. Doman. Anti-windup control for an air-breathing hypersonic vehicle model. In *AIAA Guidance Navigation and Controls Conference and Exhibit*, Aug. 21-24 2006. Keystone, Colorado.

[24] K.P. Groves, D.O. Sigthorsson, A. Serrani, S. Yurkovich, M. Bolender, and D. Doman. Reference command tracking for a linearized model of an air-breathing hypersonic vehicle. In *AIAA Guidance, Navigation, and Control Conference and Exhibit*, 15-18 August 2005. San Francisco,California.

[25] W. Heiser and D. Pratt. AIAA, Washington, D.C., 1994, pp. 109–143.

[26] R. A. Hyde. *H–inf Aerospace Control Design: A VSTOL Flight Application.* Springer-Verlag, 1995.

[27] H. Ikawa. Rapid methodology for design and performance prediction of integrated supersonic combustion ramjet engine. 17(3):437, 1991.

[28] J. Jang, A. M. Annaswamy, and E. Lavretsky. Adaptive flight control in the presence of multiple actuator anomalies. In *Proceedings of the 2007 American Control Conference*, pages 3300–3305, New York, NY,20-23 August 2007.

[29] J. Jang, A. M. Annaswamy, and E. Lavretsky. Adaptive flight control in the presence of multi-input magnitude saturation. In *(to appear) IEEE Conference on Decision and Control*, Cancun, Mexico, Dec. 2008.

[30] Dennis R. Jenkins. Hypersonic before the shuttle: A concise history of ther x-15 research plane. Monographs In Aerospace History 18, National Aeronautics and Space Administration, Washington, D.C., 2000.

[31] J.Levin, P. Ioannou, and M. Mirmirani. Adaptive mode suppression scheme for an aeroelastic airbreathing hypersonic cruise vehicle. In *AIAA Guidance, Navigation, and Control Conference and Exhibit*, 18-21 August 2008. Honolulu,Hawaii.

[32] M. Kuipers, P. Ioannou, B.Fidan, and M. Mirmirani. Robust adaptive multiple model controller design for an airbreathing hypersonic vehicle model. In *AIAA Guidance, Navigation, and Control Conference and Exhibit*, 18-21 August 2008. Honolulu,Hawaii.

[33] M. Kuipers, M. Mirmirani, P. Ioannou, and Y. Huo. Adaptive control of an aeroelastic airbreathing hypersonic cruise vehicle. In *AIAA Guidance, Navigation, and Control Conference and Exhibit*, 20-23 August 2007. Hilton Head,South Carolina.

[34] J. F. Magni, S. Bennani, and J. T. (eds.). *Robust flight control: a design challenge.* Springer, 1997.

[35] C. I. Marrison and R. F. Stengel. Design of robust control systems for a hypersonic aircraft. *AIAA GCD*, 21:58–63, 1998.

[36] Laurie A. Marshall, Griffin P. Corpering, and Robert Sherrill. A chief engineer's view of the nasa x–43a scrmajet flight test. In *AIAA-2005-3332*, 2005.

[37] NACA. *Air Force - NACA Conference on XS–1 Flight Research*, Muroc, CA, 1948. NASA Historical Reference Collection.

[38] Richard D. Neumann. Defining the aerothermodynamic methodology. In *Hypersonics:v. 1 : Defining the Hypersonic Environment*, page 127. 1989.

[39] J.T. Parker, A. Serrani, S. Yurkovich, M. Bolender, and D. Doman. Approximate feedback linearization of an air-breathing hypersonic vehicle. In *AIAA Guidance Navigation and Controls Conference and Exhibit*, Aug. 21-24 2006. Keystone, Colorado.

[40] J.T. Parker, A. Serrani, S. Yurkovich, M. Bolender, and D. Doman. Control-oriented modeling of an air-breathing hypersonic vehicle. *Journal of Guidance, Control, and Dynamics*, 30(3), May-June 2007.

[41] D. Sigthorson, A. Serrani, S. Yurkovich, M. Bolender, and D. Doman. Tracking control for an overactuated hypersonic air-breathing vehicle with steady state constraints. In *AIAA Guidance Navigation and Controls Conference and Exhibit*, Aug. 21-24 2006. Keystone, Colorado.

[42] D. 0. Sigthorson, P. Jankovsky, A. Serrani, S. Yurkovich, M. Bolender, and D. Doman. Robust linear output feedback control of an airbreathing hypersonic vehicle. *Journal of Guidance, Control, and Dynamics*, 31(4), July-August 2008.

[43] R. F. Stengel, J. R. Broussard, and P. W. Berry. Digital controllers for vtol aircraft. *IEEE Aerospace and Electronic Systems*, AES 14(1):54–63, 1978.

[44] Robert F. Stengel. *Optimal Control and Estimation.* Dover, New York, 1994.

[45] Robert F. Stengel. *Flight Dynamics.* Princeton University Press, Princeton and Oxford, 2004.

[46] Wendell H. Stillwell. X–15 research results. Sp 60, National Aeronautics and Space Administration, Washington, D.C., 1965.

[47] M. O. Thompson. At the edge of space: The x-15 flight program. Smithsonian Institution Press, Washington DC, 1992.

[48] USAF. *Air Force Supersonic Research Airplane XS–1 Report No. 1.* NASA Historical Reference Collection, 1947.

[49] Qian Wang and Robert F. Stengel. Robust nonlinear control of a hypersonic aircraft. *Journal of Guidance, Control, and Dynamics*, 23(4), Jul-Aug 2000.

[50] Qian Wang and Robert F. Stengel. Robust control of nonlinear systems with parametric uncertainty. *Automatica*, 38:1591–1599, 2002.

[51] R. J. Weber and J. S. Mackay. An analysis of ramjet engines using supersonic combustion. Technical Report NACA TN–4386, Sept 1958.

[52] Haojian Xu, Maj D. Mirmirani, and Petros Ioannou. Adaptive sliding mode control design for a hypersonic flight vehicle. *Journal of Guidance, Control, and Dynamics*, 27(5), Sept-Oct 2004.